MODELING THE HYDRODYNAMICS OF A FLUIDIZED BED

by

Mirka Miluska Deza Grados

Dissertation submitted to the faculty of Virginia Polytechnic Institute and State University in partial fulfillment of the requirements for the degree of

Doctor of Philosophy

In

Mechanical Engineering

Francine Battaglia, Chair
Srinath Ekkad
Theodore J. Heindel
Danesh K. Tafti
Uri Vandsburger

April 3, 2012

Blacksburg, Virginia

Keywords: Computational Fluid Dynamics, Two-Phase Flow, Fluidized Bed, Biomass, Numerical Simulations, Pressure Fluctuation Analysis

MODELING THE HYDRODYNAMICS OF A FLUIDIZED BED

Mirka Miluska Deza Grados

Abstract

Biomass is considered a biorenewable alternative energy resource that can potentially reduce the use of natural gas and provide low cost power production or process heating needs. Biomass hydrodynamics in a fluidized bed are extremely important to industries that are using biomass material in gasification processes to yield high quality producer gas. However, biomass particles are typically difficult to fluidize due to their peculiar shape and a second inert material, such as sand, is typically added to the bed. The large differences in size and density between the biomass and inert particles lead to nonuniform distribution of the biomass within the fluidized bed, and particle interactions and mixing become major issues. The main goal of this research was to use CFD as a tool for modeling and analyzing the hydrodynamic behavior of biomass as a single material or as part of a mixture in a fluidized bed.

The first part of this research focused on the characterization of biomass particles in a fluidized bed and validation of a numerical model with experimental results obtained from pressure measurements and CT and X-ray radiograph images. For a 2D fluidized bed of glass beads, the pressure drop, void fraction and mean bed height expansion were in quantitative agreement between the experiments and simulations using Syamlal-O'Brien and Gidaspow drag models. It was encouraging that the Gidaspow model predictions were in close agreement because the model does not require knowing the minimum fluidization as an input. Ground walnut shells were used to represent biomass because the material fluidizes uniformly and is classified as a Geldart type B particle. Two-dimensional simulations of ground walnut shells were analyzed to determine parameters that can not easily be measured experimentally. The parametric study for ground walnut shell indicated that the material can be characterized with a medium sphericity (≈ 0.6) and a relatively large coefficient of restitution (≈ 0.85).

In the second part of this work numerical simulations of a ground walnut shell fluidizing bed with side air injection were compared to CT data for the gas-solid distribution to demonstrate the quantitative agreement for bed fluidization. The findings showed that 2D simulations

overpredicted the fluidized bed expansion and the results did not demonstrate a uniformly fluidizing bed. The 3D simulations compared well for all cases. This study demonstrates the importance of using a 3D model for a truly 3D flow in order to capture the hydrodynamics of the fluidized bed for a complicated flow and geometry.

Finally, CFD modeling of pressure fluctuations was performed on sand and cotton-sand fluidized beds operating at inlet velocities ranging from 1.0–9.0U_{mf} with the objective of predicting characteristic features of bubbling, slugging, and turbulent fluidization regimes. It was determined that the fluidized bed can be modeled using MUSCL discretization and the Ahmadi turbulence model. Three-dimensional sand fluidized beds were simulated for different fluidization regimes. Fluidized beds for all the regimes behaved as second-order dynamic systems. Bubbling fluidized beds showed one broad peak with a maximum at 2.6 Hz while slugging and turbulent showed two distinct peaks. It was observed that the peak at low frequency increased in magnitude as the flow transitioned from a slugging to a turbulent fluidization regime. CFD simulations of fluidized beds with the purpose of studying pressure fluctuations have demonstrated to be a useful tool to obtain hydrodynamic information that will help determine the fluidization regime. Prediction of slugging and turbulent fluidization regimes using CFD have not been reported to date. The work presented here is the first of its kind and can be an important advantage when designing a reactor and evaluating different operation conditions without the need to test them in a pilot plant or a prototype.

Acknowledgements

I would like to take this opportunity to thank the people who have made my research and dissertation possible. First and foremost, I would like to thank Dr. Francine Battaglia for giving the opportunity to work with her in this amazing research project, for believing in me from the beginning, and for mentoring during all these years. Her advice, invaluable insight, and recommendations have made this work possible and are greatly appreciated. She has guided me, encouraged me, and taught me to conduct research work, to prepare and make professional presentations, to write papers, and to effectively teach a class among many other things. She made sure I had the financial and personal support I needed to succeed as a doctoral student and her advising and teaching style have inspired me to pursue an academic career.

I would also like to thank my committee members, Dr. Srinath Ekkad, Dr. Ted Heindel, Dr. Danesh Tafti, and Dr. Uri Vandsburger for their contributions and recommendations to this work. I would like to thank Dr. Ted Heindel for his insight, collaboration, and experimental data while writing conference and journal papers.

Thank you to the agencies who provided me with financial support: the Department of Energy (grant DE-FG36-08GO18214), URS Corporation (grant 11: 3.671.884.001 PR# 531), the ISU Institute of Physical Research and Technology, and Grow Iowa Values Fund. Computational resources were provided by the Computational Research for Energy Systems and Transport Laboratory (CREST Lab), the Advanced Research Computing (ARC) at Virginia Tech, and the High Performance Computing Center at Iowa State University; their technical support is appreciated. Thank you to Mr. Nathan Franka for providing me with experimental data. Also, thank you to my former and current colleagues for their feedback and recommen-

dations during our research group meetings.

Finally, I would like to thank my family. To the love of my life, my husband Toño for his unconditional love, support, and understanding. He made my career a priority and followed me to Virginia for me to get my doctorate. To my children, Brenda and Patrick, for their love and patience, they are my strength, my inspiration, and the joy of my life. To my parents, Emma and Nestor, for their love, for teaching me the value of education, and for all the sacrifices they made to give me a college education.

TABLE OF CONTENTS

LIST OF TABLES

LIST OF FIGURES

CHAPTER 1. Introduction

1.1 Background

Fluidization is the process by which gas flowing at sufficient velocity through a granular material causes this material to behave like a liquid [1]. One example of fluidization that takes place in a cylindrical column is shown in Fig. 1.1. A perforated plate, called the distributor plate, is located at the bottom and its purpose is to uniformly distribute the gas into the bed. The bed is composed of granular material, which is located in the lower region where fluidization takes place. The granular material is usually injected into the bed through a side port. The freeboard is the upper region above the bed occupied primarily of the gases. Gases leaving the freeboard are taken for further treatment, such as particle removal and gas separation, before the gases can be used for process heating or as a fuel.

The velocity at which the material begins to fluidize is called the minimum fluidization velocity. Increasing the gas velocity beyond this point will produce voids, commonly called "bubbles", within the fluidized bed. The size, shape, and location of the voids constantly change due to their very dynamic behavior in the gas-solid flow. Flow rates above the minimum fluidization result in either bubbling, slugging or turbulent flow regimes. In the bubbling regime, vigorous movement of particles, and channeling and bubbling of the gas is observed with bubbles coalescing and growing as they rise. When the bubbles grow as large as the bed width, a slugging bed develops. In the turbulent regime, the terminal velocity of the solids is exceeded and the flow is characterized by agitated motions of solid clusters, considerable entrainment, and the upper surface of the bed is not clearly defined.

Fluidization can be characterized by particle and fluid properties. Geldart [2] classified particle behavior into four groups based on particle size, and the difference between the particle

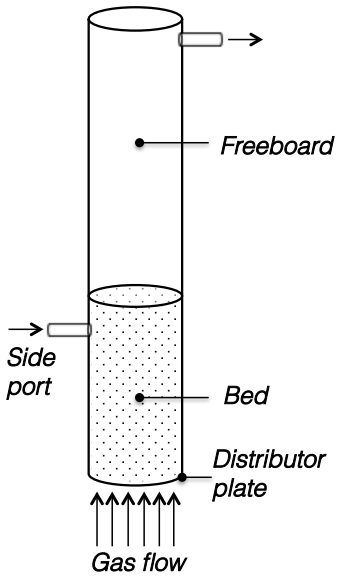

Figure 1.1: Geometry of a gasifier

and fluid density :

1. Group A (aeratable) are small or low density particles that easily fluidize with small bubbles at high fluid velocities.

2. Group B (sandlike) fluidizes well with intense bubble formation and coalescence.

3. Group C (cohesive) is comprised of very fine particles extremely difficult to fluidize.

4. Group D (spoutable) are large or dense particles that fluidize with difficulty, where extreme channeling and exploding bubbles show their irregular behavior.

Generally, Geldart B particles are used as bed material for gasification processes due to their uniform fluidization.

Fluidized beds are found in many industrial processes, which include gasification, pyrolysis, and combustion of different particles. Some advantages of fluidized bed operation include nearly isothermal conditions due to the rapid mixing of particles, high heat and mass transfer rates, resistance to sudden changes in operation conditions such as temperature, and the ability to work with particles of various sizes [1, 3]. The use of biomass particles in fluidized beds is

of current interest because biomass is a renewable resource that can be obtained from waste materials and it does not produce greenhouse gases. Biomass hydrodynamics in a fluidized bed are extremely important to industries that are using biomass material in gasification processes to yield high quality producer gas. The use of biomass is considered as a biorenewable alternative energy resource that can potentially replace natural gas and provide low cost power production or process heating needs. It is also important for pyrolysis of biomass, which is a thermal conversion process that produces liquid fuel and chemicals with the potential of substituting fossil fuels.

Although biomass gasifiers are being built and used in biorefineries, there are problems with fluidizing the media. Biomass particles are typically difficult to fluidize due to their peculiar shape and a second inert material, such as sand, alumina, or calcite, is typically added to the bed. The large differences in size and density between the biomass and inert particles lead to nonuniform distribution of the biomass within the fluidized bed, and particle interactions and mixing become major issues. Therefore, the fluidization characteristics of biomass particles are of critical importance because of known problems such as particle agglomeration, defluidization, elutriation, and segregation [4–9].

Agglomeration in fluidized beds is the formation of particle aggregates that begins when part of the fuel ash melts and causes bed particles to adhere to one another. It has mostly been attributed to the presence of alkali species in the ash of biomass fuels, which at high temperatures and under prolonged operation form a permanent bond among bed particles [10]. Agglomeration leads to defluidization of the bed, that is, the bed will no longer have liquid-like behavior. Elutriation is defined as the removal of fine particles from a mixture, as particles moves from the bed to the freeboard, which is the boundary that separates the primary bed from the gas flow. When particles of a varying sizes are present in the freeboard, larger particles tend to fall back into the bed while finer particles (fines) may leave the bed. Elutriation occurs to a certain extent at all freeboard heights. At small freeboard heights most of the larger particles are entrained by the gas; this does not happen at larger freeboard heights [1]. Segregation is the separation of material due to a wide particle size distribution or particles of

different densities. Heavier particles will tend to travel to the bottom of the bed after bubbles pass by them.

Typically, experiments are used to design and optimize fluidized beds; however pilot plants are also used since a laboratory scale reactor may not accurately reproduce the hydrodynamics of the bed. Building a pilot plant is an expensive approach for research and development, and computational fluid dynamics (CFD) offers an alternative method to study solid-gas behavior of fluidized beds. CFD calculations can provide quantitative property and flow information such as pressure, temperature, volume fraction, velocity, etc., throughout the reactor for a better understanding of the conditions and distribution of the particles. Furthermore, CFD can be used to assist in the design of reactors through parametric studies and provide visual information to researchers.

Most of the research on biomass gasification modeling has focused on the combustion process, predicting gas temperature, composition, and moisture content for the combustion efficiency of the reactor. Other aspects of biomass fluidization, such as minimum fluidization and fluidizability, and residence time of biomass particles, have been studied and a summary can be found in Ref. [3]. Most of the reported research on hydrodynamic aspects of biomass fluidized beds is experimental work. To date, there is little published information on fluidized bed hydrodynamics, especially when biomass is injected into a reactor.

1.2 Research Objective and Approaches

The goal of this research is to computationally model biomass and biomass-inert cold-flow fluidized beds using the open source software Multiphase Flow with Interphase eXchanges (MFIX) and to compare and validate the models with experiments when available. For the work on biomass fluidized beds, experimental data was provided by Franka et al. [11, 12] for measurements using X-ray computed tomography and X-ray radiography. For the pressure fluctuation analysis on biomass-inert material fluidized beds, simulation results have been compared with experimental data of Zhang et al. [13, 14]

In practice, biomass is not well characterized, and so the first part of this study is an

attempt to demonstrate how particle properties affect the hydrodynamics of a fluidized bed. Glass beads will be used to model the bed for purposes of validation between the experiments and computational models because the material is well characterized. Initial work is then pursued to study single component biomass gasification using ground walnut shell. Both glass beads and ground walnut shell particles correspond to Geldart type B classification. The simulations will consider factors such as particle sphericity, coefficient of restitution, and drag models. Results from the simulations will be compared with the particle distribution, bed height, and pressure drop obtained from experiments.

Another issue is the fluidizing biomass media; inert materials are used but segregation may still occur. Side air injection is used to enhance and promote mixing in the bed and serves as a means to inject biomass for gasification. From a computational resource point of view, two-dimensional simulations are easier to perform than three-dimensional simulations, but they may not capture the proper physics. The next step in this research is to compare two- and three-dimensional simulations in a fluidized bed with side air injection to determine when two-dimensional simulations are adequate to capture the bed hydrodynamics. Simulations are first completed for a glass bead fluidized bed and then applied to a biomass (walnut) fluidized bed. Furthermore, the effects of increasing fluidization air flow and side port air flow on the homogeneity of the bed material are studied. Two air injection ports diametrically opposed to each other are also considered to determine their effects on fluidization hydrodynamics.

Pressure fluctuation data obtained from fluidized bed combustors and gasifiers are a rich source of information on the hydrodynamic states of these systems [15,16]. The flow regimes of a fluidized bed can be determined with pressure fluctuation analysis. Pressure measurements are reliable, easy to obtain and are inexpensive. CFD can be used as a tool to aid in the design and parametric study of different operating conditions without the need to perform laboratory experiments. The resulting time series data can be investigated by different methods based on time domain, frequency domain and state space domain [17].Using standard deviation and power spectra density (PSD), the fluidization regimes of a biomass-inert media, specifically a cotton-sand fluidized bed have been studied. The same analysis has been performed in a

sand bed and compared with the binary mixture fluidized bed to determine the validity of the approximation for low biomass-to-inert material mass ratio. The analysis has been applied to fluidized beds with superficial gas velocities ranging from two to nine times the minimum fluidization velocity with the purpose of capturing bubbling to turbulent flow regimes.

1.3 Outline of the Dissertation

In Chapter 2, a survey of studies related to biomass hydrodynamics in fluidized beds is summarized including mixing and segregation and relevant CFD work. This chapter will also summarize a survey of methods for CFD modeling and drag models, and will briefly explore different approaches for pressure fluctuation analysis. Chapter 3 presents the hydrodynamics theory of multi-fluid modeling and the numerical formulation used by MFIX, a FORTRAN code developed by the National Energy Technology Laboratory (NETL). The formulation will include two relevant drag models. Chapter 4 describes the work related to validation of the multi-fluid model and grid resolution using a glass bead fluidized bed. Characterization of one biomass material, namely ground walnut shell, and the comparison of two drag models for biomass fluidized beds is discussed. Chapter 5 presents studies of a fluidized bed with one side injection ports. Two- and three-dimensional coordinate systems will be compared and then a study of the effects of increasing fluidization air flow and side port air flow on the homogeneity will be presented. Chapter 6 is an extensive study of pressure fluctuation analysis applied to single and binary fluidized beds of sand and cotton-sand, respectively, to determine different fluidization regimes and identify characteristics of each regime using different analysis methods. A summary of the main conclusions for chapter 4, 5 and 6 is presented in chapter 7. This chapter also describes proposed work to continue the research of CFD as a useful tool for modeling the hydrodynamics of biomass in a fluidized bed.

CHAPTER 2. Literature Review

This chapter presents a survey on different aspect of fluidized beds that includes basic theory in fluidization as well as experiments and numerical modeling of biomass fluidized beds, drag models, side injection ports and the use of pressure fluctuation to analyze the hydrodynamics of fluidized beds.

2.1 FluidizationTheory

2.1.1 Pressure Drop and Minimum Fluidization Velocity

Beginning with a packed (fixed) bed, the drag force produced by the inlet gas velocity to the bed material also increases as the gas velocity increases. Pressure drop through the bed will increase as the drag force increases until eventually the force due to pressure balances the weight of the bed material. When this happens, the bed is said to be at the onset of fluidization and the corresponding velocity is called minimum fluidization velocity, U_{mf}. After this point, the bed is fluidized and the pressure drop across the bed remains constant, as seen in Fig. 2.1.

Minimum fluidization velocity and pressure drop are important parameters used to characterize the fluidized bed and they can be determined with experiments or using well-known correlations established through experimentation. By performing a one-dimensional steady momentum balance in an incipient fluidized bed and neglecting the effects of solids-wall friction, gas-wall friction, and solids pressure gradient, the buoyant force will balance the drag force resulting in the following equation:

$$(1 - \epsilon_g)(\rho_s - \rho_g)g = \frac{\beta}{\epsilon_g}(u_g - u_s) \tag{2.1}$$

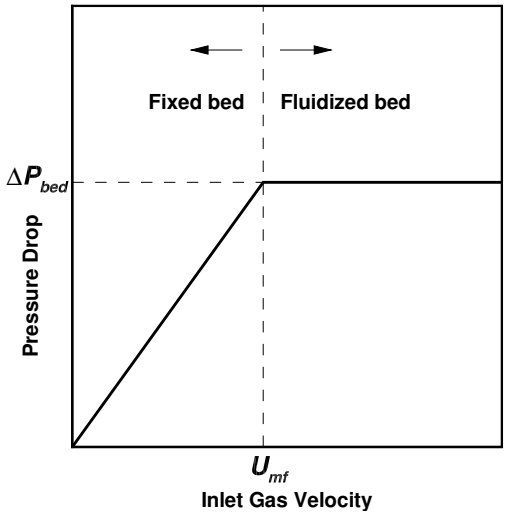

Figure 2.1: Pressure drop accross the bed versus inlet gas velocity.

where ϵ_g is void fraction, ρ_s and ρ_g are the solids and gas densities, β is the fluid-particle friction coefficient, and u_g and u_s are the gas and solids velocities. The fluid-particle friction coefficient can be found by applying the same momentum balance to a packed bed and neglecting acceleration, wall friction, and gravity, the resulting equation represents Darcy's law, a constitutive equation that describes the flow of a fluid through a porous media:

$$-\epsilon_g \frac{dP}{dz} = \frac{\beta}{\epsilon_g}(u_g - u_s) \tag{2.2}$$

The friction coefficient can also be found by comparing Eqn. 2.2 with the Ergun equation for packed beds [18]:

$$\frac{\Delta P}{\Delta z} = 150\frac{\mu_g(1-\epsilon_g)^2 U_g}{\epsilon_g^3(\psi d_p)^2} + 1.75\frac{(1-\epsilon_g)\rho_g U_g^2}{\epsilon_g^3 \psi d_p} \tag{2.3}$$

where U_g is the superficial gas velocity defined as $U_g = \epsilon_g(u_g - u_s)$. The comparison of Eqns. 2.2 and 2.3 will yield the following equation for $\epsilon_g < 0.8$:

$$\beta = 150\frac{\mu_g(1-\epsilon_g)^2}{\epsilon_g(\psi d_p)^2} + 1.75\frac{(1-\epsilon_g)\rho_g|u_g - us|}{\psi d_p} \tag{2.4}$$

At minimum fluidization velocity, the solids velocity (u_s) is zero. Therefore, Eqn. 2.1 and the first term of Eqn. 2.4 result in the known minimum fluidization velocity correlation based in

the Ergun equation for $Re_{mf} < 20$

$$U_{mf} = \frac{(\psi d_p)^2(\rho_s - \rho_g)g}{150\mu_g}\frac{\epsilon_{mf}^3}{1-\epsilon_{mf}} \tag{2.5}$$

where:

$$Re_{mf} = \frac{d_p U_{mf}\rho_g}{\mu} \tag{2.6}$$

Pressure drop can be calculated by comparing Eqns. 2.1 and 2.2, noting that dP/dz can be expressed as $\Delta P/\Delta z$ and given the linear variation of the pressure drop in the bed, the pressure gradient can be expressed in terms of the pressure drop through a bed of height h_0 as $\Delta P_bed/h_0$, thus:

$$\Delta P_{bed} = (1-\epsilon_g)(\rho_s - \rho_g)gh_0 \tag{2.7}$$

2.1.2 Binary Mixture and Segregation

One of the challenges with biomass fluidized beds is segregation. Biomass particles have a peculiar shape that makes it difficult to fluidize and an inert material, such as sand, is usually added to the bed. However, due to the differences in size and density of the bed material, segregation of these particles may occur. Segregation due to particle size has been studied by Hoffman et al. [19] and Wu and Baeyens [20] among many other researchers. They found that smaller particles segregated to the upper part of the fluidized bed, while larger particles segregated to the lower part. Others focused their research in density segregation [21] finding that particles with lower density segregated to the upper part of the bed and particles with higher density segregated to the lower part of the bed. Recently, Zhang et al. [14] highlighted the effect of fluidization regime in the segregation of cotton stalks and sand, where the size of the bubbles and inlet velocity played an important role in the mixing or segregation of the material. They found that for larger bubbles and mildly high velocities, mixing was enhanced. On the other hand, when smaller bubbles were present at lower and higher velocities, which corresponds to the bubbling and turbulent regimes, respectively, segregation was observed.

To characterize a binary mixture, properties for the mixture must be calculated, and different approaches have been proposed to describe binary mixtures. One of the approaches

requires calculating weighted averages of the Archimedes and Reynolds numbers, which can be used with single-component equations (e.g. Eqn. 2.5) to determine the minimum fluidization velocity, however Chien-Song et al. [22] have demonstrated that this method does not appropriately capture the behavior of the system. Another approach is to develop correlations for a specific system; however the applicability of these correlations is limited by the particular set of properties and operating conditions of the system. The most commonly accepted approach involves the definition of mixture properties bases on the mass fraction and properties of the individual components. Chien-Song et al. [22] summarizes three methods that use this approach and suggests the following correlations as one of the most reliable for determining the mixture density, ρ_M, and mixture diameter, d_M:

$$\rho_M = \left[\sum \left(X_i/\rho_i\right)\right]^{-1} \tag{2.8}$$

$$d_M = \left[\rho_M \sum \left(X_i/d_i/\rho_i\right)\right]^{-1} \tag{2.9}$$

where X_i is the mass fraction of each component (i) of the mixture.

If one of the particles comprising the mixture has a non-spherical shape, a mean diameter is determined. The Sauter mean diameter, originally developed by Sauter [23], is defined as the diameter of a sphere whose volume-to-surface area ratio is the same as the nonspherical particle of interest:

$$\frac{V_p}{A_p} = \frac{\frac{4}{3}\pi(d_p/2)^3}{4\pi(d_p/2)^2} \tag{2.10}$$

Therefore:

$$d_p = 6\frac{V_p}{A_p} \tag{2.11}$$

Sphericity (ψ) is a measure of how spherical a particle and is defined as the ratio of the surface area of a sphere with the same volume as the given particle to the surface area of the particle [24]:

$$\psi = \frac{\pi^{\frac{1}{3}}(6V_p)^{\frac{2}{3}}}{A_p} \tag{2.12}$$

The void fraction of the mixture, ϵ_M, can be determined by solving the Eqn. 2.5 with the mixture properties. The initial bed height, h_0, of the mixture can be estimated by the definition

of the solids volume fraction of the mixture:

$$\epsilon_{s,M} = 1 - \epsilon_{g,M} = \sum \frac{V_i}{Ah_0} \tag{2.13}$$

Bulk densities of each component as part of the mixture are determined by:

$$\rho_{b,i} = \frac{m_i}{Ah_0}. \tag{2.14}$$

2.1.3 Fluidization Regimes

Fluidization can be classified by a number of regimes according to the gas inlet velocity. As the inlet velocity increases beyond the minimum fluidization, the fluidized bed will either begin to bubble, expand, or channel. Based on experimental evidence, a fluidized bed of Geldart B particles will display a bubbling behavior for moderate inlet gas flowrates.. As bubbles rise to the upper surface of the bed, they increase in size due to bubble coalescence as shown in the schematic of Fig. 2.2 (a).

Increasing the inlet gas velocity will cause the coalescing bubbles to extend across most of the bed cross-section. The bubbling behavior is no longer observed and the bubbles move in a single periodic wave known as the slugging regime, shown in Fig. 2.2 (b). When the gas inlet velocity approaches the terminal velocity of the particles, a turbulent fluidization regime will develop. Fluidized beds operating in the turbulent fluidization regime show irregular voids, agitated mixing of solids, and an upper surface that is not well defined (Fig. 2.2 (c)). Further increasing the velocity will cause particles to become entrained and elutriate. Circulating fluidized beds normally operate in this mode, known as the fast fluidization regime.

2.2 Biomass in Fluidized Beds

Since biomass particles are difficult to fluidize due to their shape, an inert material is typically added to the bed. The large differences in size and density between the biomass and inert particles lead to a nonuniform distribution of the biomass within the fluidized bed and problems such as particle agglomeration, defluidization, elutriation, and segregation have been investigated.

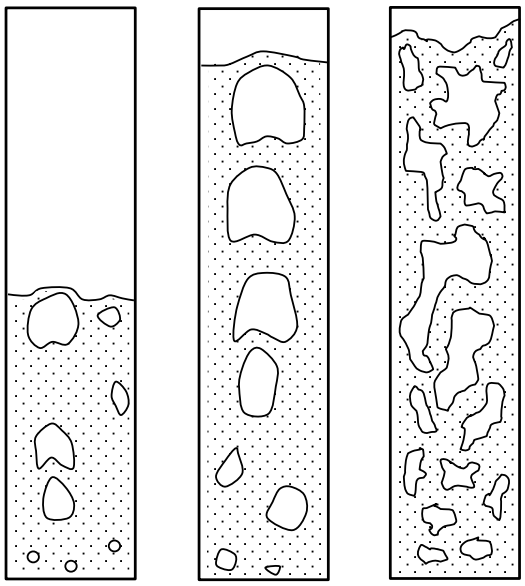

Figure 2.2: Fluidization regimes for fluidized beds (a) bubbling, (b) slugging, and (c) turbulent.

Six different biomass fuel materials (bark, Lucerne, reed canary grass, bagasse, olive flesh, and cane trash) were tested to identify agglomeration during gasification and combustion in fluidized beds by Ohman et. al [4]. After gasification, all the materials showed an thick homogeneous inner layer of silicates and and outer thick layer of accumulated particles. The same trend was shown during combustion for all fuel materials except Lucerne, which suggested that generally, the same mechanisms of agglomeration are present during gasification and combustion. Scala et al. [5] studied the relevance of attrition in the combustion of three biomass materials. Their findings revealed that wood chips were extremely prone to fragmentation after devolatilization, pine seed shells fragmented moderately and olive husks were very resistant to fragmentation. Primary fragmentation seemed to have a significant effect on the average particle size, and the particle size distribution of biomass particles after devolatilization and could not be neglected.

Defluidization of the bed occurs when the bed material agglomerates. Tendency for agglomeration was found to be enhanced by material size respective to the biomass sand, combustor size, and the presence of internals (i.e. the horizontal cooling tubes) as reported by Chirone

et al. [6]. They also reported that when the formation of stable bonds between bed particles prevailed over the breaking of agglomerated sand, defluidization was quickly achieved. They were able to predict the onset of defluidization by analyzing the pressure variance inside the bed, since the bed size distribution and fluid dynamics of the bed changed with the presence of sand aggregates. Nijenhuis [8] also used a pressure fluctuation method to detect agglomeration before defluidization occurs; pressure was measure at high frequencies with the Early Agglomeration Recognition System (EARS). They used this system and designed the attractor comparison method, which is insensitive to variations in gas velocity and bed mass up to 10%. Tests were performed for a cold-flow bed of miscanthus and two other fuels and then applied the technique to an 80-MW wood-fired fluidized-bed combustion plant. Bartels et al. [9] used the attractor comparison for early detection of agglomeration, and concluded that increasing the superficial gas velocity to break up agglomerates led to a blocked cyclone inlet, temporarily decreasing the temperature below the melting point of potassium silicates and increasing the temperature later will again cause agglomeration. Therefore a semi-continuous change in bed material, although not ideal, might be needed.

2.3 Numerical Models of Biomass Fluidized Beds

To date, there is little published information on fluidized bed hydrodynamics when biomass is injected into a reactor. Most of the CFD work has been performed with the purpose of predicting combustion performance parameters such as combustion efficiency, gas composition, temperature, and moisture content of biomass.

Limited research has been performed using CFD to analyze the hydrodynamics of fluidized beds containing biomass. Zhang and Brandani [25] proposed a modified particle bed model for bubbling fluidized beds; their CFD simulations for a fluidized bed showed that pressure fluctuations, and bubble size and number increased with the superficial velocity. Ravelli et al. [26] used CFD to study the combustion of refuse-derived fuel (RDF), which is produced by shredding and dehydrating municipal solid waste, in a full–scale fluidized bed combustor. Although more emphasis was put on modeling the combustion in the freeboard, the use of a

Lagrangian approach qualitatively predicted the trajectories followed by RDF particles in the bed.

More work has been conducted by Papadikis et al. [27, 28] with the purpose of studying some aspects of hydrodynamics of biomass particles in a fluidized bed. They first studied one biomass particle in a fluidizing sand bed using a Lagrangian–Eulerian approach with the purpose of modeling the momentum transport from the fluidized bed to the biomass particle and concluding that the drag force on the particle is the parameter that defines its motion [27]. In another study, three different particle were tested to determine their effects on char entrainment and Papadikis et al. [28] concluded that smaller particles are efficiently entrained from the reactor.

Zhang et al. [13, 14] have worked on the characterization of segregation in cotton-sand fluidized beds with different mass ratios. The have used standard deviation of pressure fluctuation signals for a wide range of inlet velocities to analyze and determine the velocity at which the regime changes from bubbling to turbulent flow.

2.4 Drag Models

Several drag models have been reported in the literature to account for the gas-solid hydrodynamics of fluidized beds. Taghipour et al. [29] compared the Syamlal–O'Brien, Gidaspow, and Wen–Yu models with experimental data and found that for relatively large Geldart B particles, the models predicted the hydrodynamics of the bed reasonably well. Du et al. [30] studied five drag models in a spouted fluidized bed and found that for dense phase simulations the models produced noticeable differences. Among the five drag models [30] tested, namely, the Richardson–Zaky, Arastoopour, Gidaspow (blending), Di Felice, and Syamlal–O'Brien, the Arastoopour and Syamlal–O'Brien models gave good predictions of the flow, but the Gidaspow drag model gave the best agreement with the experimental data. Another extensive model comparison in fluidized beds was made by Mahinpey et al. [31] for bed expansion and pressure drop at different superficial velocities in a fluidized bed using the Di Felice, Gibilaro, Koch, Syamlal–O'Brien, Arastoopur, Syamlal–O'Brien (adjusted), Di Felice (adjusted), Gidaspow,

Zhang–Reese, and Wen–Yu drag models. All of the models gave acceptable qualitative agreement with experimental data; however results for the adjusted models of Syamlal–O'Brien and Di Felice showed an improvement in quantitative predictions of the bed hydrodynamics.

Finding an appropriate drag model for biomass fluidized beds is of particular interest to the research herein. The underlying issue is that the drag models cited previously, which gave better predictions, require information about the bed hydrodynamics that is not always known for biomass particles or can be easily measured experimentally. For example, the adjusted models of Di Felice or Syamlal–O'Brien require minimum fluidization velocity to tune the drag correlations. In addition, the Syamlal–O'Brien model requires void fraction of the packed bed and particle density. Furthermore, the aforementioned drag model studies used glass beads as the solid particle in the fluidized beds; however none of the drag models have been tested to validate the hydrodynamics of a fluidized bed using biomass particles. Two models, the adjusted Syamlal–O'Brien and the Gidaspow with a blending function, will be compared in this study to assess the hydrodynamics of a biomass fluidized bed. Our choice of models to test is based on results and recommendations of the previous studies [29–31].

2.5 Side Injection Port

Side air injection is used to enhance and promote mixing in the fluidized bed. Earlier work on horizontal injection mainly focused on finding empirical correlations to measure the jet penetration length [32–35]. Geometry parameters of the injection port, including shape, diameter, and location, and flow conditions such as superficial velocity and injection velocity, have been considered to determine their effects on jet penetration.

Experimental studies of Rajan et al. [36] found that side air injection influenced the circulation pattern of the fluidized bed. Low jet flow promoted mixing and enhanced solid circulation while high flow rates showed a tendency to increase elutriation and in small diameter beds and caused slugging. Chyang et al. [37] experimentally studied the modes of gas discharge from a single jet in a 2D fluidized bed. They identified three regimes (bubbling, transition, and jetting) by comparing a modified Froude number (Fr^*) and the ratio of nozzle to particle di-

ameter. The bubbling regime was characterized by low Fr^* and the jetting regime occurred at high Fr^*. Chen and Weinstein [38] numerically and experimentally investigated a 2D fluidized bed with horizontal jet injection. They compared solids volume fraction in the jet–influenced area and found three different regions: coherent voids, bubble trains, and a zone of surrounding compaction. Another important contribution was made by Xuereb et al. [39] who experimentally determined the penetration length and expansion angle as well as the effects of inlet and jet velocity and particle diameter. They confirmed that close to the injection point, there is a dragging zone of particles from the dense phase into the jet.

Hong et al. [35] proposed a correlation for inclined jets, based on Merry's correlation [32] for horizontal jets and validated it with experimental data and numerical simulations using a two-fluid model for fluidization. The influences of gas velocity of the jet, nozzle diameter, inclination, and location were studied in detail. The correlation can be simplified for horizontal jet injection at small angles of inclination. Numerical simulations conducted by Tyler and Mees [40] compared three discretization schemes (Hybrid, Minmod, and Superbee), and found that simulating the bed with the Superbee scheme resulted in bubble and jet behavior, shape, and formation consistent with what was observed in experiments. From their preliminary study with qualitative comparisons, they concluded that 3D simulations were in best agreement with experiments. More numerical simulations have been done by Li et al. [41] by proposing a scaled Gilbaro drag model in a 3D cylindrical reactor to avoid overprediction of bed expansion and agglomeration of particles in the bed. The results of the simulations were tested quantitatively by comparing the jet penetration length and angle with experiments and three empirical correlations. Li et al [42] also investigated the effects of single and multiple jets in the hydrodynamics of a rectangular fluidized bed. They concluded that multiple jets do not influence each other significantly until they start to overlap. Another conclusion was that gas injection strongly affects the fluid behavior of the bed that is above the injection port when the injection flow rate is relatively high, and side effects are negligible in the part below the injection port. It was also concluded that deep penetration of jet enhanced solid circulation in the core; however deeper penetration could lead to a slugging bed flow.

2.6 Pressure Fluctuation Analysis

Pressure fluctuation data obtained from fluidized bed combustors and gasifiers are a rich source of information on the hydrodynamic states of these systems [15,16]. The measurements use a single pressure transducer connected to holes tapped in the side of the fluidization vessel. In order to keep particles out of the pressure sampling lines, fine screens or purge gas are used. The resulting time series data can be analyzed by a number of different methods, including standard deviation, probability density functions, autocorrelation analysis, and power spectral density (PSD) analysis [17,43].

One of the most common pressure fluctuation analyses is standard deviation. It has often been used to identify different regimes in fluidized beds, where a maximum value with respect to inlet gas velocity is associated with the transition from a bubbling to turbulent fluidization regime. Standard deviation has also been used to determine minimum fluidization velocity [44–47] and to detect the onset of defluidization in operating fluidized beds [48]. Bi and Grace [49] and Bi et al. [50–52] extensively studied the use of standard deviation to determine the transition to a turbulent fluidization regime. Two velocities were identified as delimiters for regime transition. The lower velocity marked the transition from a bubbling to turbulent regime and it was located where the standard deviation reached its maximum. The transition is also known as the slugging fluidization regime. The other identified velocity marked the transition from turbulent to fast fluidization regime, where standard deviation remains approximately constant as inlet gas velocity increases. Recently, Zhang et al. [13,14] used standard deviation to study the transition from bubbling to turbulent regime in cotton-sand fluidized beds of different mass ratios and this work will be discussed further in Chapter 6.

Another tool for studying pressure data is frequency domain analysis, which is performed using a Fourier transform. A method for obtaining the frequencies associated with a system is a power spectral density approach. The objective is to determine dominant frequencies in the time-series and relate them to physical phenomena [53]. Other authors, such as Brue and Brown [16] and Nicastro and Glicksman [54] have used PSD to validate dynamic similitude and scale-up by comparing spectra of models, proptotypes, and full-scale units. Using a Gaussian

curve, Parise et al. [55] fitted power spectra to detect defluidization of a bed using changes in the average and the standard deviation. At the beginning of this decade, most PSD analyses were based on experimental data; finding of some of the researchers are detailed below. Later, CFD validation with experiments have been reported.

In 2001, Brown and Brue [15] revised the sampling techniques commonly used for scaling beds. They determined that sampling of at least 20 minutes and as long as 60 minutes was necessary to capture important low-frequency dynamical information. They also determined that at least 15 periodograms had to be averaged for an accurate estimate of the PSD. Another finding was that bubbling as well as circulating fluidized beds behaved as multiple second-order dynamical systems and that unique peaks were identified by the PSD analysis caused by different operation conditions. Johnsson et al. [56] analyzed a circulating fluidized bed (CFB) at different ambient conditions and fluidization regimes; PSD helped identify three regions, one macro-structure due to bubble flow and two other regions at high frequency due to finer structures. Van der Schaaf et al. [57] determined bubble, gas slug, and cluster length scales from pressure fluctuation data measured in the bed and the plenum. The results compared remarkably well with their experiments. Gou et al. [58] compared the dynamic behavior of a fluidized bed at high temperatures (1000°C) for three different size ash particles using PSD, wavelet, and chaos analysis. PSD peaks coincide with the bubble formation frequency found with the other methods of analysis. Shou and Leu [59] compared standard deviation with PSD and wavelet analysis to find the critical gas velocities for fluidization regime transition and found good agreement between the methods used to analyze the dynamics of the bed.

The first CFD models to predict pressure fluctuation were performed by Wachem et al. [60] and Benyahia et al. [61]. They both used a 2D Eulerian-Eulerian model and reported reasonable agreement with experiments. Van der Lee et al. [62] and Chandrasekaran et al. [63] used a 2D Eulerian-Eulerian approach to investigate the behavior of linear low density polyethylene (LLDP) particles in a fluidized bed and compared their results with experimental data obtained with X-ray tomography. They studied the pressure fluctuation and bubble properties and the effects of bubble velocities, superficial gas velocity and initial bed height

on the hydrodynamics of the bed. Polyethylene is a particle with non-ideal characteristics of shape and size distribution, and therefore, the numerical model was not in good agreement with the experiments. It was suggested that coefficient of restitution and angle of internal friction be determined experimentally and to properly develop a formulation for modeling the solid-phase stress tensor.

Johansson et al. [64] tested different closure models, compressibility, and inflow modes. They determined that the kinetic theory of granular flow (KTGF) for the particles compared well with experimental data and compressibility did not have a significant effect on the simulation results. On the contrary, the air feeding system was crucial for predicting the overall dynamic behavior of the bed. This conclusion was also reported by Sasic et al. [65] when they found that under certain conditions, a strong interaction between the inlet supply system and the gas-solid fluidized bed in the form of pressure waves was propagated.

A rectangular bed with a single jet operating in a bubbling fluidization regime was studied by Utikar and Ranade [66] using glass and polypropylene as bed material. Dominant frequency of PSD near the sparger was greater for simulations than for experiments but compared well at higher locations. They suggested quantifying sensitivity of solids viscosity, coefficient of restitution, and frictional stresses to improve the model. Most recently, Mansourpour et al. [67] used a Lagrangian-Eulerian method to model a bubbling fluidized bed of polyethylene particles. They investigated the influence of pressure on bubble characteristics (rise velocity, size, break-up rate) and found that pressurizing the bed promoted more uniform bed expansion. Wang et al. [68] concluded that pressure fluctuations originated above the distributor when a pulse of gas was injected in the bed. They also found that the amplitude of pressure fluctuation increased with the inlet velocity for bubbling fluidized beds, where two peaks where identified in the spectrum. Fluctuations were associated with bubble formation above the distributor and bubble eruption in the bed surface.

Acosta-Iborra et al. [69] found that using a 3D domain was necessary to model a bubbling fluidized bed to obtain good predictions for power spectra and bubble behavior compared to the experiments. Using a 2D Eulerian-Eulerian model to compare simulations with experi-

mental pressure fluctuation and acoustic emission energy, Sun et al. [70] studied a bubbling bed of LLPD particles. PSD for simulations using the Syamlal-O'Brien drag model compared better with results obtained from experimental pressure fluctuations. The computed vertical turbulent energy spectrum of particles was used to study the intensity of particle motion.

In closing, this chapter serves as a review to acknowledge the progress that has been made and the limitations that researchers have encountered. Each of these areas will be studied and presented in the following chapters. In Chapter 4, two drag models will be validated for a biomass fluidized bed. Chapter 5 will discuss side injection in a fluidized bed, and Chapter 6 will explore the use of pressure fluctuation analysis in single and binary mixtures, and determine characteristic features in fluidized beds of three different fluidization regimes.

CHAPTER 3. Theory and Numerical Formulation

In this chapter, a mathematical model for multiphase flow is presented. The model includes governing equations and constitutive relationships needed to close the system. Governing equations are discretized using finite volume schemes and a modified version of the SIMPLE algorithm is used to solve algebraic equations for multiphase flow.

3.1 Governing Equations

The FORTRAN code, Multiphase Flow with Interphase eXchanges (MFIX), is used for all simulations in this work. A multifluid Eulerian-Eulerian model is employed in MFIX [71] and assumes that each phase behaves as interpenetrating continua with its own physical properties. The instantaneous variables are averaged over a region that is larger than the particle spacing but smaller than the flow domain. Volume fractions are introduced to track the fraction each phase occupies in the averaging volume, where ϵ_g is the gas phase volume fraction (also referred to as the void fraction) and ϵ_s is the solid phase volume fraction for the m^{th} solid phase. The volume fractions must satisfy the relation:

$$\epsilon_g + \sum_{m=1}^{M} \epsilon_{sm} = 1 \tag{3.1}$$

For a mixture of particles, each distinct particle type to be modeled is represented as a solid phase m for a total of M phases. Each solid phase is described with an effective particle diameter d_p and characteristic material properties, and a conservation equation is solved for each solid phase.

The continuity equations for the gas phase and the solids phases, respectively, are:

$$\frac{\partial}{\partial t}(\epsilon_g \rho_g) + \nabla \cdot (\epsilon_g \rho_g \mathbf{u}_g) = \sum_{n=1}^{N_g} R_{gn} \tag{3.2}$$

$$\frac{\partial}{\partial t}(\epsilon_{sm} \rho_{sm}) + \nabla \cdot (\epsilon_{sm} \rho_{sm} \mathbf{u}_{sm}) = \sum_{n=1}^{N_{sm}} R_{smn} \tag{3.3}$$

The subscripts g and s indicate the gas and solid phases. Other variables include the density (ρ) and velocity vector ($\mathbf{u}$). The right-hand sides of the equations represent the interphase mass transfer due to chemical reactions or physical processes. For the present work these terms are set to zero.

The momentum equations for the gas and solid phases have the form:

$$\frac{\partial}{\partial t}(\epsilon_g \rho_g \mathbf{u}_g) + \nabla \cdot (\epsilon_g \rho_g \mathbf{u}_g \mathbf{u}_g) = -\epsilon_g \nabla P_g + \nabla \cdot \bar{\bar{\sigma}}_g + \sum_{m=1}^{M} \mathbf{I}_{gm} + \epsilon_g \rho_g \mathbf{g} \tag{3.4}$$

$$\frac{\partial}{\partial t}(\epsilon_{sm} \rho_{sm} \mathbf{u}_{sm}) + \nabla \cdot (\epsilon_{sm} \rho_{sm} \mathbf{u}_{sm} \mathbf{u}_{sm}) = -\epsilon_{sm} \nabla P_g + \nabla \cdot \bar{\bar{\sigma}}_{sm} - \mathbf{I}_{gm} + \epsilon_{sm} \rho_{sm} \mathbf{g} + \sum_{m=1, l \neq m}^{M} \mathbf{I}_{ml} \tag{3.5}$$

The expressions on the left side are the net rate of momentum increase and the net rate of momentum transfer by convection. The right side includes contributions for buoyancy caused by the fluid pressure gradient, the stress tensors ($\bar{\bar{\sigma}}$), gravity ($\mathbf{g}$), and the interaction forces ($\mathbf{I}$) accounting for the momentum transfer between the gas and solid phases; this will be discussed in detail in Section 3.2.4.

The granular temperature θ for the solid phase can be related to the granular energy, defined as the specific kinetic energy of the random fluctuating component of the particle velocity:

$$\frac{3}{2}\theta = \frac{1}{2} < \mathbf{C}^2 > \tag{3.6}$$

and the fluctuation in the particle velocity is $\mathbf{C} = \mathbf{u}$ - $\mathbf{C}_m$, where $\mathbf{C}_m$ is the instantaneous translational particle velocity and the symbol $< >$ designates the operation of taking an average. The resulting transport equation for the granular temperature [72] is:

$$\frac{3}{2}\left[\frac{\partial}{\partial t}(\epsilon_{sm} \rho_{sm} \theta_m) + \nabla \cdot (\epsilon_{sm} \rho_{sm} \theta_m) \mathbf{u}_{sm}\right] = \bar{\bar{\sigma}}_{sm} : \nabla \mathbf{u}_{sm} - \nabla \cdot \mathbf{q}_{\theta_m} - \gamma_{\theta_m} + \phi_{gm} + \sum_{l=1, l \neq m}^{M} \phi_{lm} \tag{3.7}$$

where $\mathbf{q}_{\theta_m}$ is the diffusive flux of granular energy, γ_{θ_m} is the rate of granular energy dissipation due to inelastic collisions [73], ϕ_{gm} is the transfer of granular energy between the gas phase and the m^{th} solid phase, and ϕ_{lm} accounts for the transfer of granular energy between the m^{th} and l^{th} solid phases. Since the numerical simulations will model a cold-flow fluidized bed, the energy equation will not be employed in MFIX and therefore is not presented here.

3.2 Constitutive Relationships

Kinetic theory for granular flow is used to calculate the solid stress tensor and solid-solid interaction forces in the rapid granular flow regime [71]. There are two distinct flow regimes in granular flow: a viscous or rapidly shearing regime in which stresses arise due to collisional or translational momentum transfer, and a plastic or slowly shearing regime in which stresses arise due to Coulomb friction between solids in close contact. A blending function to provide a smooth transition between each regime is employed [74]. For this study we investigate the coefficient of restitution, therefore we will show the relevant equations in detail; further details related to the models can be found in the MFIX theory guide [71].

3.2.1 Gas-solid equation of state

It is assumed that the gas density can be modeled using the ideal gas law:

$$\rho_g = \frac{p_g M_w}{R T_g} \tag{3.8}$$

where p_g is the gas pressure, M_w is the gas molecular gas weight, R is the universal gas constant and T_g is the gas temperature

3.2.2 Solid phase stress tensor

The constitutive relationship for the solid phase stress tensor (Eqn. 3.5) is:

$$\bar{\bar{\sigma}}_{sm} = \begin{cases} -P_{sm}^{pl}\bar{\bar{I}} + \bar{\bar{\tau}}_{sm}^{pl} & \text{for } \epsilon_g \leq \epsilon_g^* \\ -P_{sm}^{v}\bar{\bar{I}} + \bar{\bar{\tau}}_{sm}^{v} & \text{for } \epsilon_g > \epsilon_g^* \end{cases} \tag{3.9}$$

where P_{sm}, $\bar{\bar{\tau}}_{sm}$, $\bar{\bar{I}}$, and ${\epsilon_g}^*$ are the solid pressure, viscous stress for the m^{th} solid phase, identity tensor, and void fraction at minimum fluidization, respectively. To describe the stress in the granular phase, the theory of Lun et al. [73] was extended by Ma and Ahmadi [75] to take into account interstitial fluid effects, where the granular pressure and stresses are:

$$P_{sm}^{v} = K_{1m}\epsilon_{sm}^{2}\theta_m \tag{3.10}$$

$$\bar{\bar{\tau}}_{sm}^{v} = 2\mu_{sm}^{v}\bar{\bar{D}}_{sm} + \lambda_{sm}^{v}tr(\bar{\bar{D}}_{sm})\bar{\bar{I}} \tag{3.11}$$

The second coefficient of viscosity (λ_{sm}^{v}), the shear viscosity (μ_{sm}^{v}), and the rate of strain tensor ($\bar{\bar{D}}_{sm}$) are given by:

$$\lambda_{sm}^{v} = K_{2m}\epsilon_{sm}\sqrt{\theta_m} \tag{3.12}$$

$$\mu_{sm}^{v} = K_{3m}\epsilon_{sm}\sqrt{\theta_m} \tag{3.13}$$

$$\bar{\bar{D}}_{sm} = \frac{1}{2}\left[(\nabla\ \mathbf{u}_{sm}) + (\nabla\ \mathbf{u}_{sm})^{T}\right] \tag{3.14}$$

The coefficients K_{1m}, K_{2m}, and K_{3m} are functions of coefficient of restitution (e_{mm}), particle density (ρ_{sm}), particle diameter (d_p), and radial distribution function (g_{0mm}), where:

$$K_{1m} = 2(1+e_{mm})\rho_{sm}g_{0mm} \tag{3.15}$$

$$K_{2m} = \frac{4d_p\rho_{sm}(1+e_{mm})\epsilon_{sm}g_{0mm}}{3\sqrt{\pi}} - \frac{2}{3}K_{3m} \tag{3.16}$$

$$K_{3m} = \frac{d_p\rho_{sm}}{2}\left[\frac{\sqrt{\pi}}{3(3-e_{mm})}\left[1+0.4(1+e_{mm})(3e_{mm}-1)\epsilon_{sm}g_{0mm}\right] + \frac{8\epsilon_{sm}g_{0mm}(1+e_{mm})}{5\sqrt{\pi}}\right] \tag{3.17}$$

In the plastic regime, an arbitrary function from the frictional flow theory [76] allows certain compressibility in the solid phase and is expressed as:

$$P_{sm}^{pl} = \epsilon_{sm}P^{*} \tag{3.18}$$

an empirical power law is used to express P^{*}:

$$P^{*} = A(\epsilon_g^{*} - \epsilon_g)^{n} \tag{3.19}$$

where $A = 10^{25}$ and $n = 10$. The solid stress tensor for the m^{th} solid phase is calculated using the formulation by Schaeffer [77]

$$\bar{\bar{\tau}}_{sm}^{pl} = 2\mu_{sm}^{pl}\bar{\bar{D}}_{sm} \tag{3.20}$$

3.2.3 Gas phase stress tensor

The gas phase stress tensor is a function of the gas pressure and the Newtonian viscous stress tensor and is expressed as:

$$\bar{\bar{\sigma}}_g = -P_g \bar{\bar{I}} + \bar{\bar{\tau}}_g \tag{3.21}$$

The viscous stress tensor ($\bar{\bar{\tau}}_g$) and the strain rate tensor for the gas phase ($\bar{\bar{D}}_g$) are given by:

$$\bar{\bar{\tau}}_g = 2\epsilon_g \mu_g \bar{\bar{D}}_g + \epsilon_g \lambda_g tr(\bar{\bar{D}}_g)\bar{\bar{I}} \tag{3.22}$$

$$\bar{\bar{D}}_g = \frac{1}{2}\left[(\nabla\ \mathbf{u}_g) + (\nabla\ \mathbf{u}_g)^T\right] \tag{3.23}$$

3.2.4 Gas–solids momentum transfer

The interaction force ($\mathbf{I}_{gm}$) in the momentum Eqns. (3.4) and (3.5) accounts for the gas-solid momentum transfer:

$$\mathbf{I}_{gm} = F_{gm}(\mathbf{u}_{sm} - \mathbf{u}_g) \tag{3.24}$$

which is the product of interphase drag coefficient between the gas and solid phases (F_{gm}) and the slip velocity between the two phases ($\mathbf{u}_{sm} - \mathbf{u}_g$). The interphase drag coefficient is different for each drag model.

It should be noted that for cases where the particle diameter is not perfectly spherical, the particle diameter used in the correlations is modified. The sphericity is the particle property that indicates how spherical a particle is, where a sphericity of unity signifies that the particle is a perfect sphere. Therefore, the modified particle diameter is:

$$d_p = \psi \bar{d}_p \tag{3.25}$$

where $\bar{d}_p$ is the mean diameter and ψ is the estimated sphericity of the actual particles. Two drag models are analyzed to determine how well they predict biomass fluidization. The first model, the adjusted Syamlal-O'Brien model, requires knowledge of U_{mf} to tune the drag coefficients, which can only be obtained from experiments. The second model, the Gidaspow model, is based on semi-empirical correlations. Both models are discussed next.

3.2.4.1 Adjusted Syamlal–O'Brien Model

Syamlal and O'Brien derived a correlation for the interphase drag coefficient that converts the terminal velocity correlations to drag correlations [71]:

$$F_{gm} = \frac{3\epsilon_{sm}\epsilon_g\rho_g}{4V_{rm}^2 d_p} C_{Ds}\left(\frac{Re_m}{V_{rm}}\right)|\mathbf{u_{sm}} - \mathbf{u_g}| \tag{3.26}$$

where the single sphere drag function [78] has the form:

$$C_{Ds}\left(\frac{Re_m}{V_{rm}}\right) = \left(0.63 + \frac{4.8}{\sqrt{Re_m/V_{rm}}}\right)^2 \tag{3.27}$$

The terminal velocity correlation (V_{rm}) and the Reynolds number (Re_m) of the particle are represented as follows:

$$V_{rm} = 0.5\left(A - 0.06Re_m + \sqrt{(0.06Re_m)^2 + 0.12Re_m(2B - A) + A^2}\right) \tag{3.28}$$

$$Re_m = \frac{d_p\,|\mathbf{u}_s - \mathbf{u}_g|\,\rho_g}{\mu_g} \tag{3.29}$$

The Syamlal–O'Brien drag model can be adjusted using experimental parameters to match the minimum fluidization velocity U_{mf} [79]. The functions A and B in Eqn. 3.28 are:

$$A = \epsilon_g^{4.14} \tag{3.30}$$

$$B = \begin{cases} c\,\epsilon_g^{1.28} & \text{for} \quad \epsilon \leq 0.85 \\ \epsilon_g^{d} & \text{for} \quad \epsilon > 0.85 \end{cases} \tag{3.31}$$

The coefficients c and d are part of the adjustments that can be made to the model and must satisfy the relation:

$$c\,0.85^{1.28} = 0.85^d \tag{3.32}$$

3.2.4.2 Gidaspow model with blending function

The Gidaspow model [80] calculates the interphase drag drag coefficient using two correlations depending on the local void fraction and a blending function. For void fractions less than 0.8, the Ergun equation is used to calculate the interphase drag coefficient, and for void

fractions greater than or equal to 0.8 the Wen-Yu equation is used. To avoid a discontinuity between the models, the blending function φ_{gs} introduced by [81] is:

$$\varphi_{gs} = \frac{\arctan\left[150 \times 1.75(0.2 - \epsilon_s)\right]}{\pi} + 0.5 \tag{3.33}$$

The interphase drag coefficient for the Gidaspow model has been implemented into MFIX using the form [82]:

$$F_{gm} = (1 - \varphi_{gs})F_{gm(Ergun)} + \varphi_{gs}F_{gm(Wen-Yu)} \tag{3.34}$$

where F_{gm} for the dense phase uses the Ergun equation when $\epsilon_g < 0.8$:

$$F_{gm(Ergun)} = 150\frac{\epsilon_{sm}^2\mu_g}{\epsilon_g {d_p}^2} + 1.75\frac{\rho_g\epsilon_{sm}}{d_p}\left|\mathbf{u}_{sm} - \mathbf{u}_g\right| \tag{3.35}$$

and F_{gm} for the dilute phase uses the Wen-Yu equation when $\epsilon_g \geq 0.8$:

$$F_{gm(Wen-Yu)} = \frac{3}{4}C_D\frac{\rho_g\epsilon_g\epsilon_{sm}}{d_p}\left|\mathbf{u}_{sm} - \mathbf{u}_g\right|\epsilon_g^{-2.65} \tag{3.36}$$

where

$$C_D = \begin{cases} 24\left[1 + 0.15(\epsilon_g Re_m)^{0.687}\right]/(\epsilon_g Re_m) & \text{for} \quad Re < 1000 \\ 0.43 & \text{for} \quad Re \geq 1000 \end{cases} \tag{3.37}$$

using the same definition of Reynolds number shown in Eqn. 3.29.

3.2.5 Solids–solids momentum transfer

The momentum transfer ($\mathbf{I}_{ml}$) between solids in the momentum Eqn. 3.5 is

$$\mathbf{I}_{ml} = F_{sml}(\mathbf{u}_{sl} - \mathbf{u}_{sm}) \tag{3.38}$$

which is the product of the coefficient for the interphase force between the solid phases m and l (F_{sml}) and the slip velocity between the two solid phases ($\mathbf{u}_{sl} - \mathbf{u}_{sm}$). The coefficient for the interphase force is derived from a simplified version of the kinetic theory [79].

$$F_{sml} = \frac{3(1 + e_{lm})(\pi/2 + C_{flm}\pi^2/8)\epsilon_{sl}\rho_{sl}\epsilon_{sm}\rho_{sm}(d_{pl} + d_p)^2 g_{0lm}\left|\mathbf{u_{sl}} - \mathbf{u_{sm}}\right|}{2\pi(\rho_{sl}d_{pl}^3 + \rho_{sm}d_p^3)} \tag{3.39}$$

where e_{lm} and C_{flm} are the coefficient of restitution and coefficient of friction between the l^{th} and m^{th} solid-phase particles, respectively, and g_{0lm} is the radial distribution function at contact for a mixture of hard spheres.

3.2.6 Granular energy

The constitutive relationships for the the transfer of granular energy between the gas phase and the m^{th} solids phase (ϕ_{gm}) and the diffusive flux of granular energy ($\mathbf{q}_{\theta_m}$) are

$$\phi_{gm} = -3F_{gm}\theta_m \tag{3.40}$$

$$\mathbf{q}_{\theta_{sm}} = -\frac{15d_p\rho_{sm}\epsilon_{sm}\sqrt{\pi\theta_{sm}}}{4(41-33\eta)}\left[1+\frac{12}{5}\eta^2(4\eta-3)\epsilon_{sm}g_{0mm}+\frac{16}{15\pi}(41-33\eta)\eta\epsilon_{sm}g_{0mm}\right]\nabla\theta_{sm}$$

where

$$\eta = \frac{1}{2}(1+e_{mm}) \tag{3.41}$$

The constitutive relationship for the rate of granular energy dissipation (γ_{θ_m}) is

$$\gamma_{\theta_m} = \frac{12}{\sqrt{\pi}}(1-e_{mm}^2)\frac{\rho_{sm}\epsilon_{sm}^2}{d_p}g_{0mm}\theta_{sm}^{3/2} \tag{3.42}$$

The partial slip boundary conditions for the particle-wall interactions [83] are employed, where the slip velocity is:

$$\mathbf{u}_{sm,slip}\cdot\bar{\bar{\sigma}}_{sm}\cdot\mathbf{n}+\frac{\pi\sqrt{3}}{6\epsilon_{sm,max}}\epsilon'\epsilon_{sm}\rho_{sm}g_{0mm}\theta_{sm,t}{}^{1/2}|\mathbf{u}_{sm,slip}|^2=0 \tag{3.43}$$

and the boundary condition for the flux of the translational fluctuation energy is:

$$-\mathbf{n}\cdot\mathbf{q}_{sm}=\frac{\pi\sqrt{3}}{4\epsilon_{sm,max}}(1-e_w^2)\epsilon_{sm}\rho_{sm}g_{0mm}\theta_{sm,t}{}^{3/2}+\mathbf{u}_{sm,slip}\cdot\bar{\bar{\sigma}}_{sm}\cdot\mathbf{n} \tag{3.44}$$

The slip velocity is defined as:

$$\mathbf{u}_{sm,slip}=\mathbf{u}_{sm}-\mathbf{u}_w \tag{3.45}$$

where $\mathbf{u}_w$ is the wall boundary velocity.

3.3 Numerical Methodology

The numerical discretization of the equations for multiphase flows uses a finite volume approach to ensure the conservation laws for mass, momentum and granular energy. In cases where a fine grid is computationally expensive, the conservative property of finite volume methods presents an advantage.

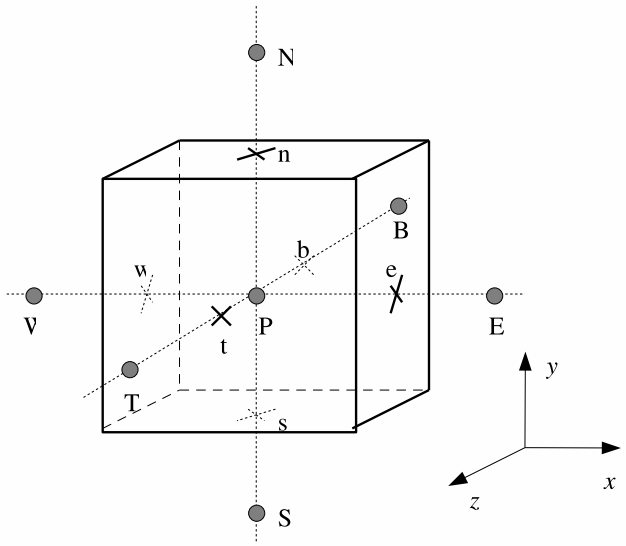

Figure 3.1: Complete staggered arrangement cell.

3.3.1 Grid Scheme

Partial differential equations are discretized using a complete staggered grid, where scalars are stored at the cell center and velocity components are stored a the cell surfaces. Complete staggered and non-staggered grids are discussed in the following section.

3.3.1.1 Complete staggered grid

Harlem and Welch [84] introduced the staggered grid shown in Fig. 3.1. For this arrangement, velocities are defined at the cell faces and pressure and other scalars such as void fraction, mass fraction, and temperature are defined at the cell center. If velocity and pressure were stored on the same grid points, pressure for two alternate grid points would appear in the momentum equations. Therefore, the zigzag pressure field for one–dimensional domains and checkerboard pressure for two–dimensional domain resulted in an acceptable solution. Three–dimensional domains had more complex fields. Unphysical pressure and velocity fields will not occurred in a staggered grid due to two neighboring grid points appearing in the momentum equations.

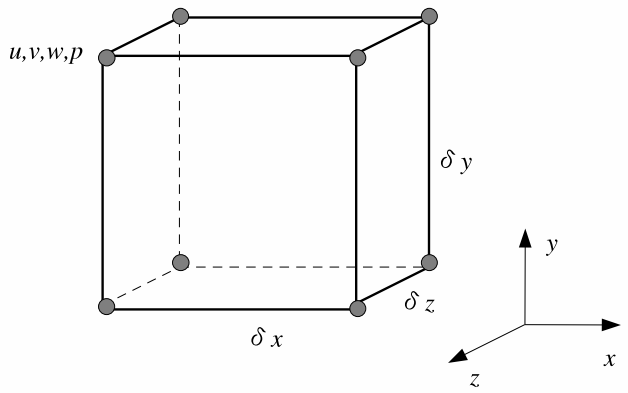

Figure 3.2: Non-staggered primitive variable arrangement for a grid cell at each node

It is important during discretization to select points in the domain where unknown dependent primitive variables are to be computed. The most important advantage of the staggered grid is the strong coupling between velocities and pressure, alleviating convergence problems and oscillations in the pressure and velocity [85]. However, a disadvantage is that only one of the velocity components is defined on each side of the domain boundary. Therefore, ghost cell outside the domain are necessary to enforce boundary condition.

The non-staggered grid [86] defines pressure and velocities at the grid nodes as shown in Fig. 3.2. Some advantages of this arrangement is its simplicity and having the velocity defined on the boundary where is generally prescribed. It is also advantageous in complex geometries and where unstructured grids are needed. However, since pressure is also defined on the boundary, the discretized equations for a node have no direct coupling between pressure and velocities, and results in odd-even splitting of the solutions. Non-staggered central-difference schemes do not perform well because of pressure-velocity decoupling leading to instability especially for high Reynolds number turbulent flows [85].

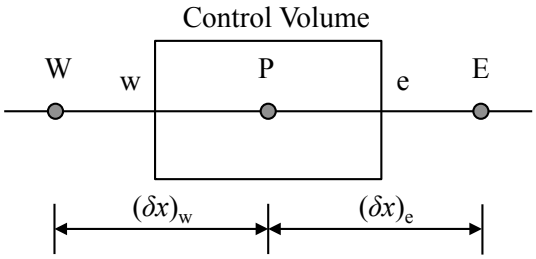

Figure 3.3: Nomenclature for the discretization on the x-direction.

3.3.2 Discretization

The following transport equation for a scalar variable Φ will be used to discuss discretization of the governing equations of the general form:

$$\frac{\partial}{\partial t}(\epsilon_m \rho_m \Phi) + \frac{\partial}{\partial x_i}(\epsilon_m \rho_m v_{mi} \Phi) = \frac{\partial}{\partial x_i}\left(\Gamma_\Phi \frac{\partial \Phi}{\partial x_i}\right) + R_\Phi \tag{3.46}$$

where $m = 0$ denotes the gas phase, $m = 1$ to M denotes the solids phases, Γ_Φ is the diffusion coefficient for Φ and R_Φ is the source term. Equation 3.46 has the form of an equation for multiphase flow except for the interphase transfer term, which will discussed later in this section. The equation is integrated over a control volume as shown in Fig. 3.1 [87]. The point P is at the center of the control volume and its neighboring points are E, W, N, S, T, and B. The half-node positions are e, w, n, s, t, and b.

Convection–diffusion terms in the x-direction are as follows:

$$\rho u \frac{\partial \Phi}{\partial x} - \frac{\partial}{\partial x}\left(\Gamma \frac{\partial \Phi}{\partial x}\right) \tag{3.47}$$

If Eqn. 3.47 is integrated over a control volume dV in the x-direction as shown in Fig. 3.3, the result of such an integration will be:

$$\int \left[\rho u \frac{\partial \Phi}{\partial x} - \frac{\partial}{\partial x}\left(\Gamma \frac{\partial \Phi}{\partial x}\right)\right] dV = \left[\rho u \Phi_e - \left(\Gamma \frac{\partial \Phi}{\partial x}\right)_e\right] A_e - \left[\rho u \Phi_w - \left(\Gamma \frac{\partial \Phi}{\partial x}\right)_w\right] A_w \tag{3.48}$$

Assuming a piecewise-linear profile between the grid points, the diffusive flux with second order accuracy at the east-face becomes:

$$\left(\Gamma \frac{\partial \Phi}{\partial x}\right)_e \approx \Gamma_e \frac{(\Phi_E - \Phi_P)}{\delta x_e} \tag{3.49}$$

Convection terms are discretized using higher-order schemes to prevent numerical diffusion that typically occurs with first-order schemes such as the upwind method. If first-order schemes are used to simulate a bubbling fluidized bed, the predicted bubbles appear as a pointed shape [87]. However, when discontinuities are present, high-order schemes tend to be deficient due to oscillations. Schemes, such as the total variation diminishing (TVD) scheme use a limiter on the dependent variables [88]. The following is an example of Φ_e at the east face using the TVD scheme:

$$\Phi_e = \xi_e \Phi_E + (1 - \xi_e)\Phi_P \tag{3.50}$$

where ξ_e is the convection weighting factor and can be calculated from the down-wind factor dwf_e as follows:

if $u_e \geq 0$

$$\Phi_e = dwf_e \Phi_E + (1 - dwf_e)\Phi_P$$

$$\xi_e = dwf_e$$

if $u_e < 0$

$$\Phi_e = dwf_e \Phi_P + (1 - dwf_e)\Phi_E$$

$$\xi_e = 1 - dwf_e$$

The down-wind factor calculated using the Superbee method can be applied to explicit conservative convection and diffusion schemes of any order of accuracy [89] such that:

$$dwf_e = \frac{1}{2}\max\left[0, \min(1, 2\theta), \min(2, \theta)\right]$$

Using the MUSCL discretization method, the down-wind factor is defined as:

$$dwf_e = \frac{1}{2}\max\left[0, \min(2\theta, 0.5 + 0.5\theta, 2)\right]$$

where $\theta = \tilde{\Phi}_C/(1 - \tilde{\Phi}_C)$ and $\tilde{\Phi}_C$ can be calculated using the following expressions:

if $u_e \geq 0$

$$\tilde{\Phi}_C = \frac{\Phi_P - \Phi_W}{\Phi_E - \Phi_W}$$

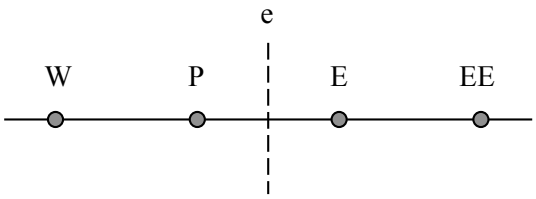

Figure 3.4: Node locations for the TVD scheme.

if $u_e < 0$

$$\tilde{\Phi}_C = \frac{\Phi_P - \Phi_{EE}}{\Phi_E - \Phi_{EE}}$$

Figure 3.4 shows the locations of P, W, E, and EE in the x-direction.

The discretized form of the transient term is:

$$\int \left[\rho u \frac{\partial \Phi}{\partial x} - \frac{\partial}{\partial x}\left(\Gamma \frac{\partial \Phi}{\partial x}\right)\right] dV \approx \left[(\epsilon_m \rho_m \Phi)_P - (\epsilon_m \rho_m \Phi)_P^0\right] \frac{\delta V}{\delta t} \tag{3.51}$$

where the superscript 0 indicates previous time step values. Since source terms are usually nonlinear, they are linearized in Φ_P as:

$$R_\Phi \approx \bar{R}_\Phi - R'_\Phi \Phi_P \tag{3.52}$$

The integration of the source term is:

$$\int R_\Phi dV \approx \bar{R}_\Phi \delta V - R'_\Phi \Phi_P \delta V \tag{3.53}$$

The coefficient R'_Φ must be greater than zero to ensure the stability of the iteration.

All scalar equations can be linearized in the following form

$$a_P \Phi_P = \sum_{nb} a_{nb} \Phi_{nb} + r \tag{3.54}$$

where r is the source term.

The continuity equations for multiphase flows have a source term for interphase mass transfer $\sum R_{lm}$ that can be discretized as:

$$\Phi_P \sum R_{lm} = \Phi_P \langle R_{lm} \rangle - \Phi_P \langle -R_{lm} \rangle \tag{3.55}$$

where l denotes gas phase and

$$\langle R \rangle = \begin{cases} 0 & \text{if } R \leq 0 \\ R & \text{if } R > 0 \end{cases}$$

The first term on the right side of Eqn. 3.55 corresponds to the source term r in Eqn. 3.54 and the term $\langle -R_{lm} \rangle$ corresponds to a_P in Eqn. 3.54.

The components of velocity and temperature are strongly coupled amongst the phases by the interphase momentum and energy transfer terms $\sum F_{ml}(u_l - u_m)$ and $\sum \gamma_{ml}(T_l - T_m)$; these terms should be made fully implicit. However, solving the equations for each velocity component together leads to a non-standard matrix structure. To decouple the equations a partial elimination of interphase coupling is used [90].

3.3.3 Modified SIMPLE Method

The semi-implicit method for pressure-linked equations (SIMPLE) was developed for the single flow field [85]. MFIX uses an extension of this method to solve the discretized equations with the proper modifications for multiphase flow. The SIMPLE algorithm derives the pressure correction equation to handle the terms in the momentum equations. Velocities solved for the momentum equations with this pressure must satisfy the continuity equations. In multiphase flows, the solids volume fraction correction is used instead of the solids pressure correction because the pressure correction requires that the term $\partial P_s / \partial \epsilon_s$ does not vanish when $\epsilon_s \to 0$.

The solids pressure increases exponentially with the solids volume fraction for regions densely packed. Thus, a small increase in volume fraction will cause a large increase in the solids pressure. Solids volume fraction corrections are under-relaxed for numerical stability as follows:

$$\text{If } (\epsilon_m)_{new} > \epsilon_p \text{ and } \epsilon'_m > 0$$

$$\epsilon'_m = \omega_{\epsilon_m} \epsilon'_m \tag{3.56}$$

where ϵ_p is the volume fraction for the packed region, ω_{ϵ_m} is an under-relaxation factor, and ϵ'_m is the correction value of solids volume fraction with guessed value of ϵ^*_m where

$$\epsilon_m = \epsilon^*_m + \epsilon'_m \tag{3.57}$$

Gas–solids flow are inherently unstable, therefore transient simulations are performed. To ensure the numerical stability, small time steps and under relaxation are used in the iterations.

CHAPTER 4. CFD Modeling and X-ray Imaging of Biomass in a Fluidized Bed

A paper published in *Journal of Fluids Engineering, 131 (11), Paper 111303*

Mirka Deza, Nathan P. Franka,Theodore J. Heindel and Francine Battaglia

Abstract

Computational modeling of fluidized beds can be used to predict operation of biomass gasifiers after extensive validation with experimental data. The present work focused on validating computational simulations of a fluidized bed using a multifluid Eulerian-Eulerian model to represent the gas and solid phases as interpenetrating continua. Simulations of a cold-flow glass bead fluidized bed, using two different drag models, were compared to experimental results for model validation. The validated numerical model was then used to complete a parametric study for coefficient of restitution and particle sphericity, which are unknown properties of biomass. Biomass is not well characterized, and so this study attempts to demonstrate how particle properties affect the hydrodynamics of a fluidized bed. Hydrodynamic results from the simulations were compared to X-ray flow visualization computed tomography studies of a similar bed. It was found that the Gidaspow (blending) model can accurately predict the hydrodynamics of a biomass fluidized bed. The coefficient of restitution of biomass did not affect the hydrodynamics of the bed for the conditions of this study; however the bed hydrodynamics were more sensitive to particle sphericity variation.

4.1 Introduction

Biomass hydrodynamics in a fluidized bed are extremely important to industries that are using biomass material in the gasification processes to yield high quality producer gas. Producer gas can be considered as a biorenewable, alternative energy resource that can potentially replace natural gas and provide low cost power production and process heating needs. Since biomass particles are typically difficult to fluidize due to their peculiar shape, a second inert material, like sand, alumina, or calcite, is typically added to the bed [3]. However, the large differences in size and density between the biomass and inert particles lead to nonuniform distribution of the biomass within the fluidized bed, and particle interactions and mixing become major issues.

Given the nature of biomass particles (shape, moisture content, pliability), their fluidization characteristics are of critical importance because of known problems such as particle agglomeration, defluidization, elutriation, and segregation [4–9]. Ideally, experiments can provide information on the fluidization characteristics of biomass, but the opacity of the bed material impedes visualization techniques. Since fluidization is a dynamic process, invasive monitoring methods can influence the internal flow, thereby reducing the reliability of the measurements [91]. As stated by Heindel et al. [92], noninvasive monitoring techniques for multiphase flows include electrical capacitance tomography, ultrasonic computed tomography, gamma densitometry tomography, X-ray fluoroscopy (radiography/stereography), and X-ray computed tomography. Franka et al. [11] used X-ray computed tomography (CT) and radiography to analyze differences in materials for fluidized beds operating under three gas flow rates. The CT images showed that glass beads fluidized much more uniformly compared to melamine, walnut, and corncob beds, and that walnut shell fluidized more uniformly as gas flow rate increased.

Most of the research on biomass gasification modeling has focused on the combustion process, predicting the composition of the resulting gas, and studying effects such as temperature, composition, and moisture content of the biomass for the combustion efficiency of the reactor. Some other aspects of biomass fluidization, such as terminal settling velocities, minimum flu-

idization and fluidizability, and residence time of biomass particles, have been studied and a summary can be found in [3]. To date, there is little published information on fluidized bed hydrodynamics when biomass is injected into a reactor. Zhang and Brandani [25] proposed a modified particle bed model in bubbling fluidized beds; their CFD simulations for a circulating fluidized bed showed that pressure fluctuations and bubble size and number increased with the superficial velocity.

Several drag models have been reported in the literature to account for the gas-solid hydrodynamics of fluidized beds. Taghipour et al. [29] compared the Syamlal–O'Brien, Gidaspow, and Wen–Yu models with experimental data and found that for relatively large Geldart B particles, the models predicted the hydrodynamics of the bed reasonably well. Du et al. [30] studied five drag models in a spouted fluidized bed and found that for dense phase simulations the models produced noticeable differences. Among the five drag models [30] tested, namely, the Richardson–Zaky, Arastoopour, Gidaspow (blending), Di Felice, and Syamlal–O'Brien, the Arastoopour and Syamlal–O'Brien models gave good predictions of the flow, but the Gidaspow drag model gave the best agreement with the experimental data. Another extensive model comparison in fluidized beds was made by Mahinpey et al. [31], for bed expansion and pressure drop with different superficial velocities in a fluidized bed using the Di Felice, Gibilaro, Koch, Syamlal–O'Brien, Arastoopur, Syamlal–O'Brien (adjusted), Di Felice (adjusted), Gidaspow, Zhang–Reese, and Wen–Yu drag models. All of the models gave acceptable qualitative agreement with experimental data; however results for the adjusted models of Syamlal–O'Brien and Di Felice showed an improvement in quantitative predictions of the bed hydrodynamics.

Finding an appropriate drag model for biomass fluidized beds is of particular interest to the research herein. The underlying issue is that the drag models cited previously, which gave better predictions, require information about the bed hydrodynamics that is not always known for biomass particles or can be easily measured experimentally. For example, the adjusted models of Di Felice or Syamlal and O'Brien require minimum fluidization velocity to tune the drag correlations. In addition, the Syamlal and O'Brien model requires void fraction of the packed bed and particle density. Furthermore, the aforementioned drag model studies used

glass beads as the solid particle in the fluidized beds; however none of the drag models have been tested to validate the hydrodynamics of a fluidized bed using biomass particles. Two models, the adjusted Syamlal–O'Brien and the Gidaspow with a blending function, will be compared in this study to assess the hydrodynamics of a biomass fluidized bed. Our choice of models to test is based on results and recommendations of the previous studies [29–31].

Hence, the goal of this research is to computationally model a cold-flow fluidized bed and to compare and validate the model with experiments. In practice, biomass is not well characterized, and so this study is an attempt to demonstrate how particle properties affect the hydrodynamics of a fluidized bed. The experiments will be accomplished using X-ray computed tomography and X-ray radiography. Glass beads will be used to model the bed for purposes of validation between the experiments and computational models because the material is well characterized. Initial work is then pursued to study single component biomass gasification using ground walnut shell. Both glass beads and ground walnut shell particles correspond to Geldart's type B classification, which according to [93], satisfactorily fluidize. In this work, the simulations of the fluidized beds will be employed using the open source software Multiphase Flow with Interphase eXchanges (MFIX). The simulations will consider factors such as particle sphericity, coefficient of restitution, and drag model. Results from the simulations will be compared with the particle distribution, bed height, and pressure drop obtained from the experiments.

4.2 Experimental Setup

4.2.1 Fluidized Bed Reactor

The fluidized bed reactor used in the experiments consisted of a 9.5 cm ID, 40 cm tall acrylic tube (a), illustrated in Fig. 4.1a. Air entered the acrylic plenum chamber (b) through a 1.0 cm air inlet fitting (c) and passed through a pipe (d) drilled with 16, 0.6 cm diameter holes. This drilled pipe served to gradually expand gas into the plenum chamber and avoid jetting phenomena. The plenum contained two 1.0 cm pressure taps (e) used for measuring pressure drop across the bed. Air left the plenum through a distributor plate drilled with

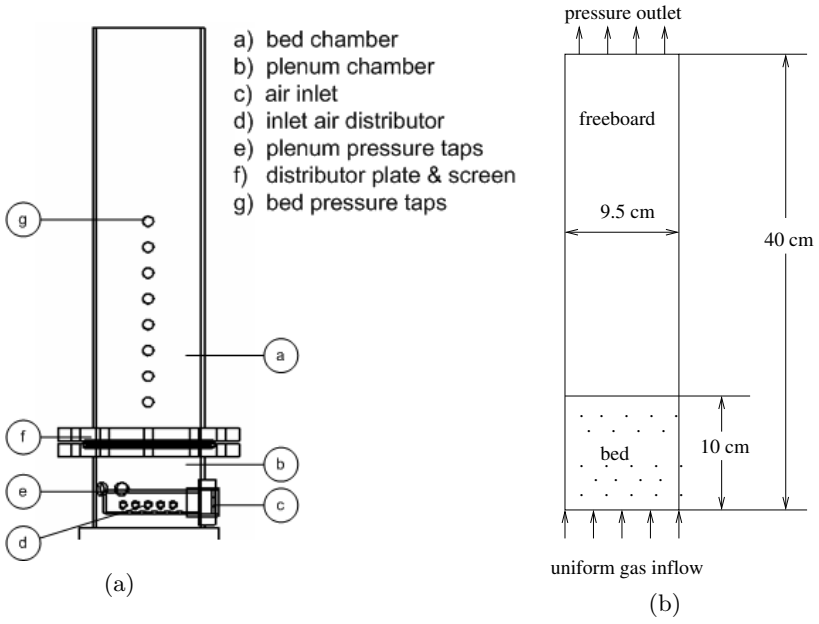

Figure 4.1: Schematic of the (a) experimental setup for a 9.5 cm ID fluidized bed and (b) the 2-D plane representing the simulated bed chamber of the cylindrical reactor.

100, 0.1 cm diameter holes; each hole was spaced 0.4 cm apart on a square grid. To eliminate coarse bed particles from becoming lodged inside the distributor plate holes, a 45 mesh screen with openings of 0.04 cm was attached to the plate. The top of the vessel was open to the atmosphere. The bed chamber included several tapped holes (g) for pressure measurements; however, these were not employed in the present study. Inlet air flow rate was controlled by a 0–3,300 cm^3/s flow meter and pressure regulator. The accuracy of the flow meter was ± 2% of the full scale reading (± 67 cm^3/s).

4.2.2 Material Selection and Minimum Fluidization

The fluidization behavior of two materials was investigated in this study. Glass beads were studied as a benchmark since the fluidization of glass is well characterized and because glass has similar properties to inert sand used in gasification. Additionally, modeling glass bead fluidization is ideal due to its high sphericity, uniform density, narrow particle size distribution, and resistance to breaking. Ground walnut shell was studied as an alternative bed material.

Ground walnut shell particles have lower density than glass beads and aspect ratios near unity. Both materials fell within Geldart's type B classification in order to maintain similar fluidization hydrodynamics between the beds. Particle diameter ranges for glass beads and ground walnut shell were 500–600 μm and 500–700 μm, respectively, and the static bed height was 10 cm for both materials (H/D=1.05).

The minimum fluidization velocity U_{mf} for each bed was experimentally measured using well-established procedures [94]. Initially, the beds were fluidized with air at a superficial gas velocity $U_g = 28$ cm/s and pressure was measured using a 0–3.7 kPa pressure gauge connected to a pressure tap in the plenum. Gas flow was decreased in increments of 1.2 cm/s and the total pressure across the bed and distributor plate was measured. By measuring pressures as the gas flow decreased, bed packing effects were removed. This was necessary because packing effects create a hysteresis loop in the pressure data when flow rate is increased. The procedure was repeated for an empty reactor in order to find the pressure drop across the distributor plate. By subtracting the empty reactor data from the total pressure drop data, the pressure drop across the bed was calculated. On the resulting plot the pressure drop across the bed appears to linearly increase with increasing superficial velocity until it reaches a point at which the pressure drop becomes constant. This point is defined as the minimum fluidization velocity. For the materials and bed conditions of this study, $U_{mf} = 19.9$ cm/s for glass beads and 18.7 cm/s for ground walnut shell. For each material, flow conditions of $1.1U_{mf}$, $1.3U_{mf}$, and $1.5U_{mf}$ were tested; for this study, the numerical model will be validated with the inflow velocity of $1.3U_{mf}$.

4.2.3 X-ray System

Iowa State University's XFloViz facility was used to image the fluidized beds and has been described in detail in the literature [92]. Consequently, only a brief outline will be presented here. Two LORAD LPX200 portable X-ray tubes provide the X-ray energy. Current and voltage can be adjusted from 0.1 to 10.0 mA and 10 to 200 kV, respectively, with a maximum power of 900 W. Low energy radiation is suppressed by 1 mm thick copper and aluminum

filters. Located opposite each X-ray source is an X-ray detector/CCD camera pair. The CCD camera with image intensifier has a temporal resolution ranging from 10 frames per second (fps) to 60 fps, depending on binning options, and is primarily used for radiographic imaging. The image intensifier is a 40.6 cm diameter Precise Optics PS164X screen detector with a 35.0 mm output image diameter. A DVC-1412 monochrome digital camera captures the image from the intensifier. Generally, 2×2 binning (640×512 active pixels) at 20 fps is used for radiographic movies in order to maximize picture quality while maintaining adequate temporal resolution. A second detector/camera pair is primarily used for CT imaging because of its high spatial resolution. This camera is located opposite the second source and is connected to a square 44×44 cm cesium-iodide scintillator screen which transforms radiation into visible light. A 50 mm Nikon lens captures images which are digitized by an Apogee Alta U9 system. This system has 3072×2048 pixels and is thermoelectrically cooled to allow long exposure times. Usually, an exposure time of 1 second with 4×4 binning is chosen to minimize acquisition time while maintaining the signal strength. Both cameras and sources are located on a 1.0 m ID rotation ring that can rotate 360° around the fluidized bed. CT and radiographic data are acquired using software developed by Iowa State University's Center for Nondestructive Evaluation (CNDE) and a personal computer with 4 GB of RAM. The software allows for control of both camera/detector pairs, as well as motion control for the rotation ring. Volumetric reconstruction of the CT images is performed using CNDE's 64-node LINUX cluster.

4.2.4 CT Images

In X-ray computed tomography with a conical X-ray beam, a series of two-dimensional projections are captured at various angles and reconstructed into a three-dimensional volumetric image. Since multiple images must be acquired for one CT, the resulting 3-D image is necessarily time-averaged. This image is a map of CT intensity values which are proportional to X-ray attenuation, which in turn is proportional to density. In this study, CT images of the glass bead fluidized bed were taken at 135 kV, 1.6 mA for every one degree around a 360° rotation. Ground walnut shell images were taken at 130 kV and 4.2 mA to improve contrast.

For all tests, the exposure time was 1 second at 4×4 binning per degree, and each test took approximately 45 minutes. A total of 260 vertical slices were captured for glass bead beds and 300 vertical slices were captured for ground walnut shell beds. The height was adjusted because the bed height expansion of ground walnut shell was larger than for glass beds, however, the difference in height did not affect the CT data.

To minimize image acquisition noise, the CCD camera was cooled to 0°C using the thermo-electric cooler. Two calibrations were applied to the CT data to remove image artifacts [92]. To account for pixel non-uniformity, linear normalization was employed. This calibration employed a linear interpolation routine to adjust pixels to respond identically to incident X-ray energy. The second calibration was only applied to the glass bead CTs and accounted for beam hardening. This artifact is often present in high density materials and occurs due to the preferential attenuation of polyenergetic X-rays. The result is that the center of an object appears less dense than the surroundings. To correct for beam hardening, an "effective λ" calibration was applied to the raw CT files before reconstruction. After calibration, the 2-D projections were reconstructed into 3-D images using CNDE software.

4.2.5 Gas Holdup

In order to quantify the CT data, time-averaged local gas holdup (void fraction) was calculated for each flow condition. The local gas holdup, ϵ_g, can be determined by knowing the local X-ray attenuation for the flow (λ), the particle (λ_p), and the gas (λ_g). Since the attenuation is proportional to the CT intensity (CTI), the local gas holdup can be calculated by knowing CT intensity data for the flow, the particle (CTI_p), and the gas (CTI_g). Therefore, the local gas holdup is defined as:

$$\epsilon_g = \frac{\lambda - \lambda_p}{\lambda_g - \lambda_p} = \frac{CTI - CTI_p}{CTI_g - CTI_p} \tag{4.1}$$

It is difficult to determine the CT intensity for a single particle due to its small size, however, the CT intensity for a static (bulk) bed of particles (CTI_b) can be used. From Eqn. (4.1), the void fraction for the bulk material can be calculated using local CT intensities for the bed,

where:

$$\epsilon_{g,b} = \frac{CTI_b - CTI_p}{CTI_g - CTI_p} \tag{4.2}$$

For a granular material, the void fraction of the bulk material ($\epsilon_{g,b}$) is defined as:

$$\epsilon_{g,b} = 1 - \frac{\rho_b}{\rho_p} = \text{Constant} \tag{4.3}$$

The bed material bulk density (ρ_b) and particle density (ρ_p) can be found experimentally and in property tables, respectively. Substituting CTI_p from Eqn. (4.2) into Eqn. (4.1) and rearranging yields an equation to find local gas holdup based on CTs for the flow condition, the gas, and the bulk material:

$$\epsilon_g(i,j,k) = \frac{CTI(i,j,k) - CTI_b(i,j,k) + [CTI_g(i,j,k) - CTI(i,j,k)]\epsilon_{g,b}}{CTI_g(i,j,k) - CTI_b(i,j,k)} \tag{4.4}$$

and i, j, k represent the locations of individual voxels in the three-dimensional (3-D) volume, where a voxel is a 3-D pixel. For each material in this study, CT data were acquired for a bed of static bulk material and the empty reactor (air only) at identical power settings used to capture fluidization (flow) CT data. Using Eqn. (4.4), each flow file was converted to show local gas holdup and a smoothing method was employed to reduce noise. The resulting time-averaged gas holdup values are determined on a 3-D grid with an approximate voxel size of 0.6 mm $\times$ 0.6 mm $\times$ 0.6 mm. Estimated absolute uncertainly in the local gas holdup is $\pm$ 0.04, which is a worst-case estimate with most data falling within an absolute gas holdup error of $\pm$ 0.02.

Three-dimensional images were viewed using internally developed visualization software, which allowed viewing of the volumetric images at any location within the imaging volume, and to adjust color mapping schemes. Since volume files contain information outside the cylindrical region of interest, a clipping feature was also used to isolate the fluidized bed. Once isolated, the spatial range was modified to show the vertical $y-z$ plane (x-slice) and the vertical $x-z$ plane (y-slice) through the column center, as well as horizontal $x-y$ planes (z-slices) at heights of 4 cm and 8 cm from the distributor plate.

4.2.6 Radiographs

In radiography, a two-dimensional projection of the 3-D attenuation is generated which is related to the density profile. Because of the high temporal resolution, multiple radiographic images may be acquired and compiled into a video to show dynamic features of an object. In this study, a 30 second movie at 20 frames per second and 2×2 binning (640×512 pixels) was captured for each flow and material condition. The radiographic images were acquired at 82 kV, 1.6 mA for the glass bead bed, and 82 kV, 1.0 mA for the ground walnut shell bed. The use of the image intensifier system resulted in a warping artifact in the resultant images, which appears as a distortion in an image's coordinate system; some regions appear to be rotated and squeezed relative to the horizontal and vertical axes [92]. To overcome this artifact, a second-order polynomial correction algorithm was applied to each warped image. Unwarped images were subsequently compiled and compressed into '.avi' movie files. Image unwarping and movie generation were performed with a script written in MATLAB to automate the process. Radiographic images in this paper are selected still frames from the resulting movies.

4.3 Two-fluid Model

4.3.1 Governing Equations

The FORTRAN code, Multiphase Flow with Interphase eXchanges (MFIX), is used for all simulations in this work. A multifluid Eulerian-Eulerian model is employed in MFIX [71] and assumes that each phase behaves as interpenetrating continua with its own physical properties. The instantaneous variables are averaged over a region that is larger than the particle spacing but smaller than the flow domain. Volume fractions are introduced to track the fraction each phase occupies in the averaging volume, where ϵ_g is the gas phase volume fraction (also referred to as the void fraction) and ϵ_s is the solid phase volume fraction for the m^{th} solid phase. The volume fractions must satisfy the relation:

$$\epsilon_g + \sum_{m=1}^{M} \epsilon_{sm} = 1 \tag{4.5}$$

For a mixture of particles, each distinct particle type to be modeled is represented as a solid phase m for a total of M phases. Each solid phase is described with an effective particle diameter d_p and characteristic material properties, and a conservation equation is solved for each solid phase. For this study, only one solid phase is modeled, therefore $M = 1$; the remaining discussion will present equations accordingly.

The continuity equations for the gas phase and the solids phases, respectively, are:

$$\frac{\partial}{\partial t}(\epsilon_g \rho_g) + \nabla \cdot (\epsilon_g \rho_g \mathbf{u}_g) = 0 \tag{4.6}$$

$$\frac{\partial}{\partial t}(\epsilon_s \rho_s) + \nabla \cdot (\epsilon_s \rho_s \mathbf{u}_s) = 0 \tag{4.7}$$

The subscripts g and s indicate the gas and solid phases. Other variables include the density (ρ) and velocity vector ($\mathbf{u}$). Note that there is no mass transfer and therefore the right-hand sides of the equations are set to zero. It is further assumed that the gas density can be modeled using the ideal gas law.

The momentum equations for the gas and solid phases have the form:

$$\frac{\partial}{\partial t}(\epsilon_g \rho_g \mathbf{u}_g) + \nabla \cdot (\epsilon_g \rho_g \mathbf{u}_g \mathbf{u}_g) = -\epsilon_g \nabla P_g + \nabla \cdot \bar{\bar{\sigma}}_g + \mathbf{I}_g + \epsilon_g \rho_g \mathbf{g} \tag{4.8}$$

$$\frac{\partial}{\partial t}(\epsilon_s \rho_s \mathbf{u}_s) + \nabla \cdot (\epsilon_s \rho_s \mathbf{u}_s \mathbf{u}_s) = -\epsilon_s \nabla P_g + \nabla \cdot \bar{\bar{\sigma}}_s - \mathbf{I}_g + \epsilon_s \rho_s \mathbf{g} \tag{4.9}$$

The expressions on the left side are the net rate of momentum increase and the net rate of momentum transfer by convection. The right side includes contributions for buoyancy caused by the fluid pressure gradient, the stress tensors ($\bar{\bar{\sigma}}$), gravity ($\mathbf{g}$), and the interaction forces ($\mathbf{I}$) accounting for the momentum transfer between the gas and solid phases; this will be discussed in detail later in this section. The constitutive equations for the gas phase tensor can be found in [71].

The granular temperature θ for the solid phase can be related to the granular energy, defined as the specific kinetic energy of the random fluctuating component of the particle velocity. The resulting transport equation for the granular temperature [72] is:

$$\frac{3}{2}\left[\frac{\partial}{\partial t}(\epsilon_s \rho_s \theta) + \nabla \cdot (\epsilon_s \rho_s \theta)\mathbf{u}_s\right] = \bar{\bar{\sigma}}_s : \nabla \mathbf{u}_s - \nabla \cdot \mathbf{q}_\theta - \gamma_\theta + \phi_g \tag{4.10}$$

where $\mathbf{q}_\theta$ is the diffusive flux of granular energy, γ_θ is the rate of granular energy dissipation due to inelastic collisions [73], and ϕ_g is the transfer of granular energy between the gas phase and solid phase. Since the numerical simulations will model a cold-flow fluidized bed, the energy equation will not be employed in MFIX and therefore is not presented here.

4.3.2 Drag Models

The interaction force ($\mathbf{I}_g$) in the momentum Eqns. (4.8) and (4.9) accounts for the gas-solid momentum transfer:

$$\mathbf{I}_g = F_g(\mathbf{u}_s - \mathbf{u}_g) \tag{4.11}$$

which is the product of the coefficient for the interphase force between the gas and solid phases (F_g) and the slip velocity between the two phases ($\mathbf{u}_s - \mathbf{u}_g$). The coefficient for the interphase force is different for each drag model.

It should be noted that for cases where the particle diameter is not perfectly spherical, the particle diameter used in the correlations is modified. The sphericity is the particle property that indicates how spherical a particle is, where a sphericity of unity signifies that the particle is a perfect sphere. Therefore, the modified particle diameter is:

$$d_p = \psi \bar{d}_p \tag{4.12}$$

where $\bar{d}_p$ is the mean diameter and ψ is the estimated sphericity of the actual particles. Two drag models are analyzed to determine how well they predict biomass fluidization. The first model, the adjusted Syamlal-O'Brien model, requires knowledge of U_{mf} to tune the drag coefficients, which can only be obtained from experiments. The second model, the Gidaspow model, is based on semi-empirical correlations. Both models are discussed next.

4.3.2.1 Adjusted Syamlal–O'Brien Model

Syamlal and O'Brien derived a correlation for the coefficient for the interphase drag force that converts the terminal velocity correlations to drag correlations [71]:

$$F_g = \frac{3\epsilon_s \epsilon_g \rho_g}{4 V_r^2 d_p} C_{Ds} \left(\frac{Re}{V_r} \right) |\mathbf{u_s} - \mathbf{u_g}| \tag{4.13}$$

where the single sphere drag function [78] has the form:

$$C_{Ds}\left(\frac{Re}{V_r}\right) = \left(0.63 + \frac{4.8}{\sqrt{Re/V_r}}\right)^2 \tag{4.14}$$

The terminal velocity correlation (V_r) and the Reynolds number (Re) of the particle are represented as follows:

$$V_r = 0.5\left(A - 0.06Re + \sqrt{(0.06Re)^2 + 0.12Re(2B - A) + A^2}\right) \tag{4.15}$$

$$Re = \frac{d_p\,|\mathbf{u}_s - \mathbf{u}_g|\,\rho_g}{\mu_g} \tag{4.16}$$

The Syamlal–O'Brien drag model can be adjusted using experimental parameters to match the minimum fluidization velocity U_{mf} [79]. The functions A and B in Eq. 4.15 are:

$$A = \epsilon_g^{4.14} \tag{4.17}$$

$$B = \begin{cases} c\,\epsilon_g^{1.28} & \text{for} \quad \epsilon \leq 0.85 \\ \epsilon_g^{d} & \text{for} \quad \epsilon > 0.85 \end{cases} \tag{4.18}$$

The coefficients c and d are part of the adjustments that can be made to the model and must satisfy the relation:

$$c\,0.85^{1.28} = 0.85^d \tag{4.19}$$

4.3.2.2 Gidaspow model with blending function

The Gidaspow model [80] calculates the interphase drag force coefficient using two correlations depending on the local void fraction value and blending function. For void fractions less than 0.8, the Ergun equation is used to calculate the interphase force coefficient, and for void fractions greater than or equal to 0.8 the Wen-Yu equation is used. To avoid a discontinuity between the models, the blending function φ_{gs} introduced by [81] is:

$$\varphi_{gs} = \frac{\arctan\left[150 \times 1.75(0.2 - \epsilon_s)\right]}{\pi} + 0.5 \tag{4.20}$$

The interphase drag force for the Gidaspow model has been implemented into MFIX using the form [82]:

$$F_g = (1 - \varphi_{gs})F_{g(Ergun)} + \varphi_{gs}F_{g(Wen-Yu)} \tag{4.21}$$

where F_g for the dense phase uses the Ergun equation when $\epsilon_g < 0.8$:

$$F_{g(Ergun)} = 150\frac{\epsilon_s^2 \mu_g}{\epsilon_g {d_p}^2} + 1.75\frac{\rho_g \epsilon_s}{d_p}\left|\mathbf{u}_s - \mathbf{u}_g\right| \tag{4.22}$$

and F_g for the dilute phase uses the Wen-Yu equation when $\epsilon_g \geq 0.8$:

$$F_{g(Wen-Yu)} = \frac{3}{4}C_D\frac{\rho_g \epsilon_g \epsilon_s}{d_p}\left|\mathbf{u}_s - \mathbf{u}_g\right|\epsilon_g^{-2.65} \tag{4.23}$$

where

$$C_D = \begin{cases} 24\left[1 + 0.15(\epsilon_g Re)^{0.687}\right]/(\epsilon_g Re) & \text{for} \quad Re < 1000 \\ 0.43 & \text{for} \quad Re \geq 1000 \end{cases} \tag{4.24}$$

using the same definition of Reynolds number shown in Eqn. 4.16.

4.3.3 Numerical Methodology

To discretize the governing equations in MFIX, a finite volume approach for a staggered grid is used to reduce numerical instabilities [90]. Velocities are stored at the cell surfaces, and scalars, such as void fraction and pressure, are stored at the center of the cell. Discretization of time derivatives are first-order and discretization of spatial derivatives are second-order. An important feature is the use of a higher-order discretization scheme for the convective terms, known as the Superbee method [95], which improves convergence and accuracy of the solution. A modification of the SIMPLE algorithm is used to solve the governing equations [90]. The first modification uses an equation for the solid volumes fraction that includes the effect of the solids pressure to help facilitate convergence for a both loosely and densely packed regions. The second modification uses a variable time-stepping scheme to improve convergence and execution speeds.

4.3.4 Domain Specification

The cylindrical reactor for the cold-flow experiments is modeled as a two–dimensional (2-D) plane representing the centerplane of the cylinder with a 9.52 cm diameter and 40 cm height, as shown in Fig. 4.1b. A Cartesian coordinate system is used to capture the random bubble dynamics characteristic of fluidized beds, and Xie et al. [74] have validated the accuracy of

Table 4.1: Particle properties and flow conditions

	Glass beads	**Walnut shells**
$\bar{d_p}$ (cm)	0.055	0.062
ρ_p (g/cm^3)	2.60	1.30
ρ_b (g/cm^3)	1.63	0.62
ψ (–)	0.9	0.5, 0.6, 0.7
e (cm/s^2)	0.95	0.75, 0.85, 0.95
U_{mf}(cm/s)	19.9	18.7
ϵ_g^* (–)	0.373	0.522
U_g (cm/s)	25.8	24.3

a 2-D approach. A uniform inlet velocity is specified at the bottom equal to the superficial gas velocity and atmospheric pressure is specified at the exit. The no-slip condition is used to model the gas-wall interactions and a partial-slip condition for the particle-wall interactions.

The packed bed height for all cases is 10 cm. Two solid materials are simulated to predict the fluidization experiments and evaluate the current computational modeling efforts. Glass beads will be used to initially validate the simulations with the experiments because the properties of glass beads are well characterized. Of particular concern is the coefficient of restitution (e) and sphericity (ψ) of the materials, especially for biomass. Glass beads have a high value of e and ψ; however, biomass properties are not always known. The material used to represent biomass is ground walnut shell because (i) it tends to fluidize uniformly [11], (ii) it falls within the Geldart type B classification, (iii) it has a density similar to saw dust but is less heterogeneous, and (iv) it is readily available (Opta Minerals, Inc). Table 4.1 summarizes the particle properties and flow conditions in this study.

4.4 Cases and Results

4.4.1 Grid Resolution Study

A fluidized bed consisting of glass beads as the bed material is used to validate the numerical modeling and will also be used to determine appropriate grid resolution. Six grid resolution cases are used to discretize the flow domain into rectangular cells with aspect ratios of 1:1

Table 4.2: Grid resolution cases

# cells	Δx(cm)	Δz(cm)
19×40	0.50	1.00
38×80	0.25	0.50
76×160	0.13	0.25
19×80	0.50	0.50
38×160	0.25	0.25
76×380	0.13	0.13

or 1:2, as shown in Table 4.2. All numerical data are time-averaged from 5 to 40 seconds using equally spaced time intervals of 0.01 s with 3,500 time realizations. Time-averaged void fraction profiles for all six grid resolutions are shown in Fig. 4.2 for the bed heights of $z = 4$ and 8 cm. Upon examining the profiles for increasing grid resolution, there is no discernible trend and all six profiles fall within similar ranges for each bed height. The largest discrepancy in the profiles is for the coarsest resolution of 19×40, as seen in Fig. 4.2(b). Based on a Richardson's extrapolation, the largest relative error is less than 1% for the coarsest grid. For the remainder of the grid study discussion, results will be presented for the worst-case grid resolution scenarios with a cell aspect ratio of 1:2.

The gas-solid distributions at approximately 10 s intervals are shown in Fig. 4.3. Each subfigure shows two images: radiographs from the experiments on the left and numerical simulations on the right. The experimental images are obtained using X-ray radiography. The comparisons between experiments and simulations are not at the exact same time but rather in a time frame of $\pm$ 1 second. The gray scale legend corresponds to the CFD predictions of void fraction and is shown to compare to the X-ray images. The X-ray images have been enhanced to more clearly show gas bubbles but the X-ray projections do not represent void fraction. The enhanced X-ray images show qualitative bubble locations in the fluidized bed because they are actually projections of the entire 3-D volume; hence the images do not show the three-dimensionality of the flow nor the solid particles in front of or behind the bubbles in the viewing direction and thus, these results are qualitative. It can be observed that small bubbles develop near the bottom and coalesce forming larger bubbles toward the top of the

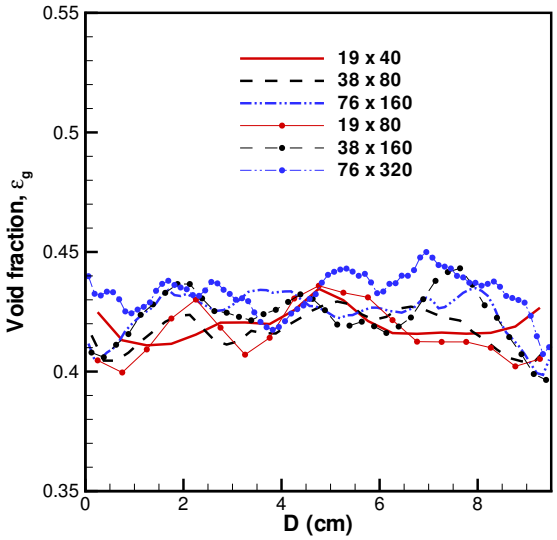

(a) $z = 4$ cm

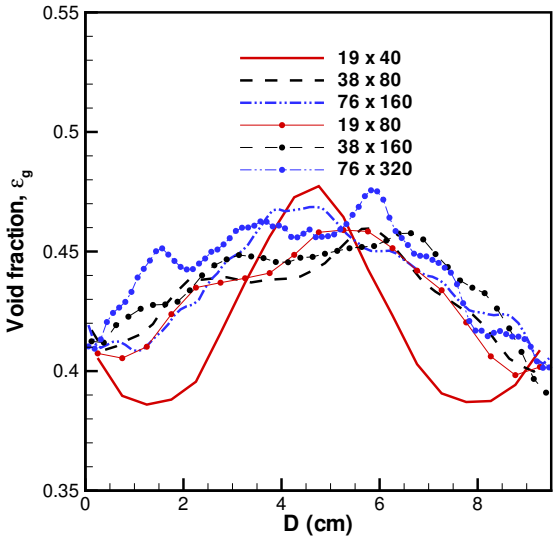

(b) $z = 8$ cm

Figure 4.2: Time-averaged void fraction for the glass bead simulations comparing six grid resolutions at (a) $z = 4$ cm and (b) $z = 8$ cm.

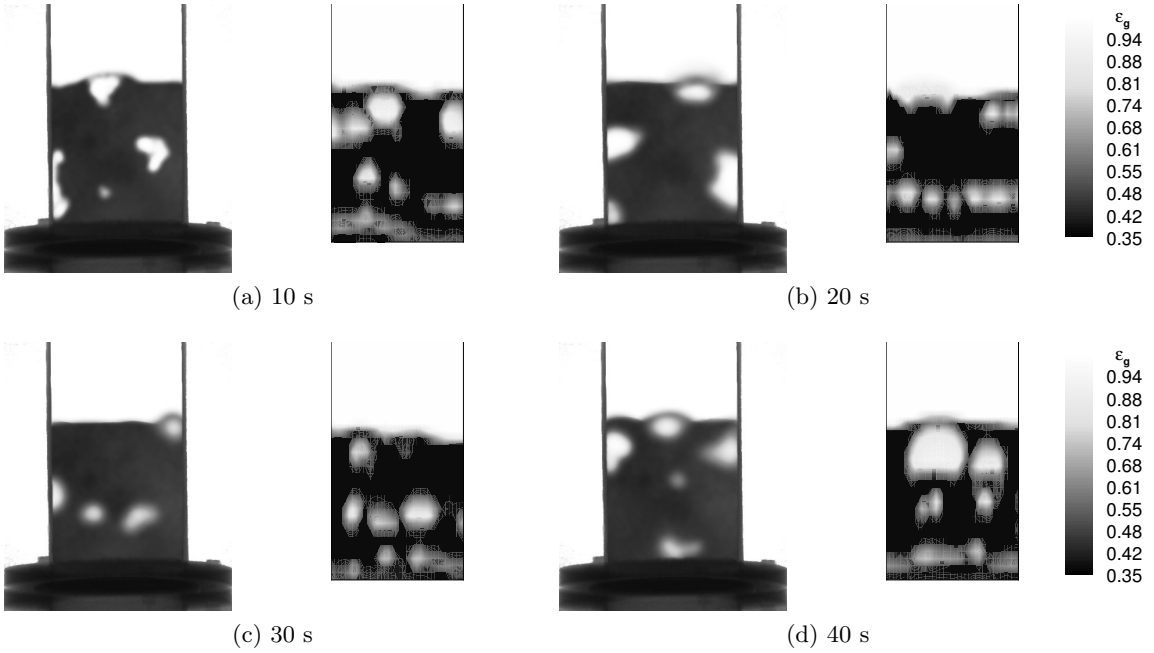

Figure 4.3: Instantaneous gas-solid distributions for the glass bead fluidized bed. For each pair of images, the left side is the X-ray radiograph and the right side is the void fraction contour from the simulation using the medium grid size at (a) 10 s, (b) 20 s, (c) 30 s, and (d) 40 s. Note: the gray scale legends are only applicable to the simulations.

bed. The qualitative correspondence between the experiment and simulation is very good.

Time-averaged void fraction (ϵ_g) contours for the entire domain for each grid size and two perpendicular planes of the CT scan images are shown in Fig. 4.4. It is obvious that the coarse grid (Fig. 4.4a) predicts a nonhomogeneous flow with dense pockets of glass beads near the top of the bed. The medium and fine grids (Fig. 4.4b,c) predict a more even distribution of bubbles throughout the bed. Comparisons of the average void fraction indicate that the medium and fine grid predictions compare better with the experiments (Fig. 4.4d,e).

The void fraction profiles at two bed heights of $z = 4$ and 8 cm are shown in Fig. 4.5 comparing the simulations with the experiments. The error bars in Fig. 4.5 represent an absolute gas holdup error of ± 0.02, which is typical of most data. A single error bar is provided for each set of experimental data in each figure to avoid confusion, but the error magnitude should be applied to all experimental data. The variations in the experimental

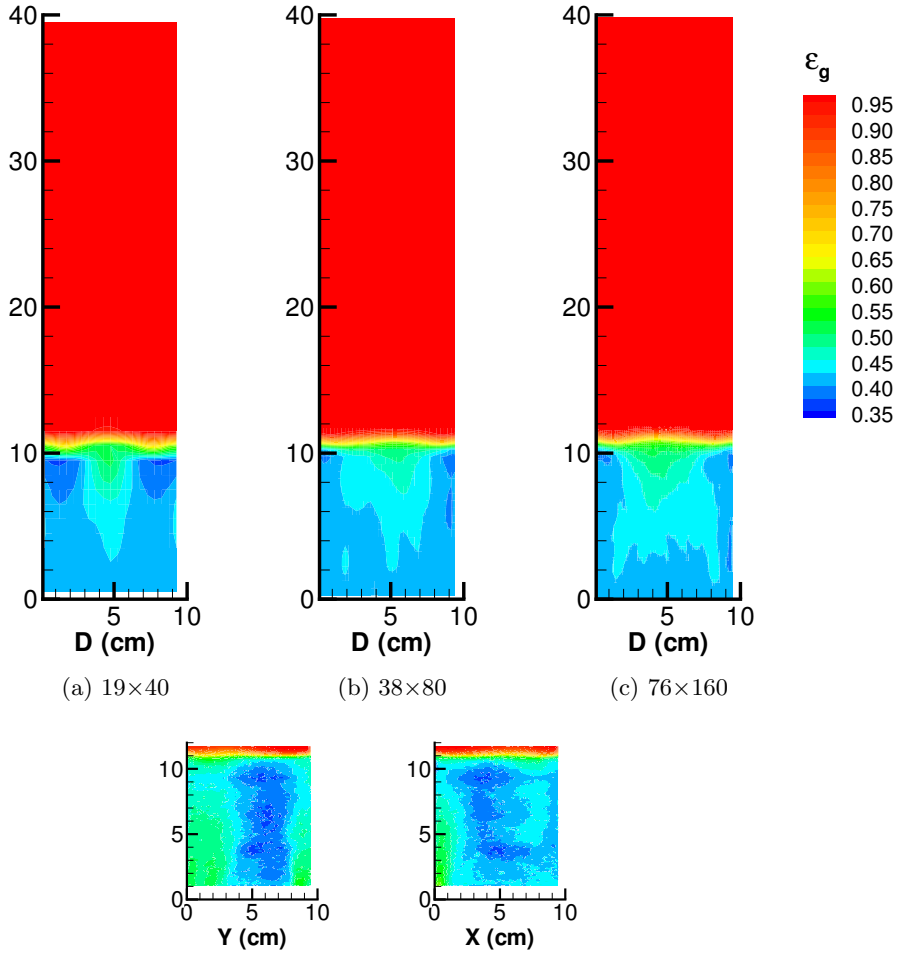

(a) 19×40 (b) 38×80 (c) 76×160

(d) X-slice (e) Y-slice

Figure 4.4: Time-averaged void fraction of the glass bead bed from numerical simulations with three different grids (a)–(c), and experiment CT images for an (d) X-slice and (e) Y-slice.

data are attributed to the nonuniform inlet conditions that result from the 100 discrete air inlet holes. At the lower bed height, the void fraction distribution is similar for all three grid resolutions. It can be seen that there are qualitative differences in the profiles for the coarse grid as compared to the medium and fine grids at the higher bed height. The lower two minima in the coarse grid profile correspond to the presence of more bead material near the region where the bed expands. Therefore, simulations are assumed independent of the grid size at a resolution of 38×80.

The time-averaged local void fractions shown in Fig. 4.5 modestly compare between the simulations and 3-D experiments, with the results on the same order of magnitude. Similar discrepancies have been shown by others [29, 30, 96, 97]. Two possible reasons may cause this discrepancy. First, the orientation of the experimental x- and y-slice locations, which are mutually perpendicular, is arbitrary. The 3-D volume could be rotated about the central axis for slightly different x- and y-slice experimental data. Second, as stated by [29], the hydrodynamics near the base of the bed can be significantly affected by the distributor design, which was not modeled in the CFD simulations because of the computational expense (each aeration hole would have to be resolved in the computational grid). The influence of the distributor design on the bed hydrodynamics was also identified by [98]. We believe the distributor has a significant influence on the time-averaged local void fraction, and this is not captured in the simulations that use a uniform velocity profile inlet condition. Clearly, the data shown closer to the distributor (Fig. 4.5a) show much greater variations.

Although the time-averaged local void fraction across the bed width accentuates the local hydrodynamic influences of the experiments, averaging these values across a horizontal line dampens local variations and provides a better comparison. For example, the void fraction averaged across the bed width versus the domain height for each grid size is compared to the experiments in Fig. 4.6. Again, the error bars represent typical experimental error in the measured data. The bed height expands to approximately 11.3 cm, which compares well with the expansion height of 11.2 cm measured in the experiments.

The similarity in instantaneous gas-solid distributions between the experiments and simu-

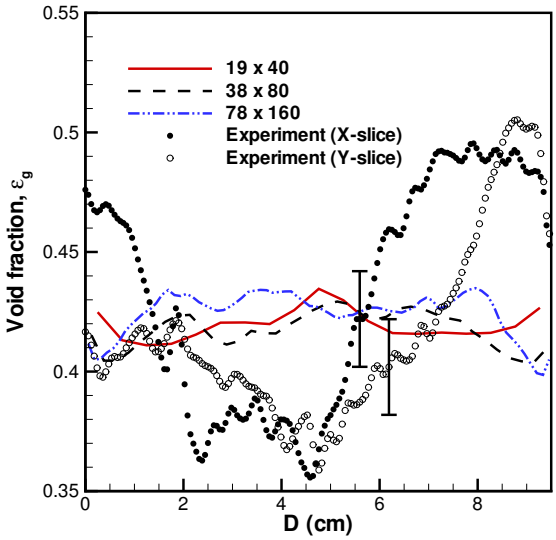

(a) $z = 4$ cm

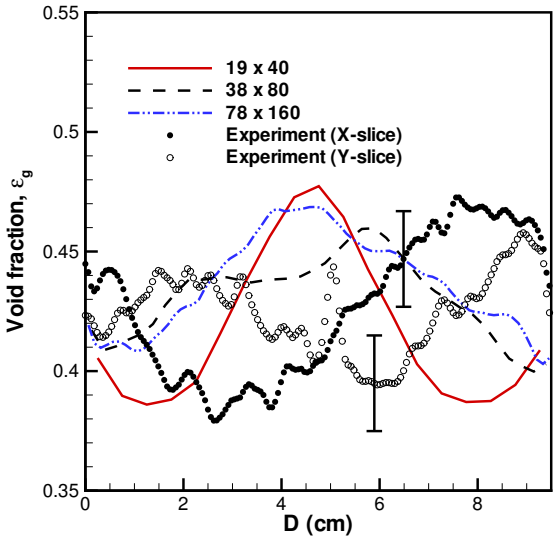

(b) $z = 8$ cm

Figure 4.5: Time-averaged void fraction for the glass bead simulations using different grid resolutions and the experimental data at (a) $z = 4$ cm and (b) $z = 8$ cm.

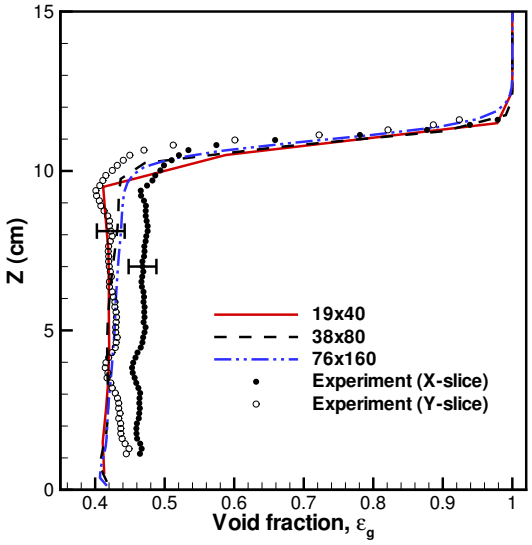

Figure 4.6: Time-averaged void fraction for the glass bead simulations using different grid resolutions and the experimental data spatially averaged across the bed width versus axial direction.

lations and quantitative comparisons of void fraction distribution throughout the bed provide confidence in the computational modeling. Based on the validation study of the glass bead bed, it is concluded that a medium grid resolution will be sufficient for use in the following studies.

4.4.2 Drag Model Study

The drag models of Syamlal-O'Brien and Gidaspow (with the blending function) are compared to experimental data for glass beads. Figure 4.7 represents the pressure drop in the glass bead bed versus superficial gas velocity for the simulations with the two drag models and the experiments. Once the bed fluidizes at a superficial gas velocity of 25 cm/s, both drag models have a pressure drop of 1,550 Pa, which agrees very well with the theoretical value and is reasonably close to 1,470 Pa obtained in the experiments. It should be noted that the Syamlal-O'Brien drag model predictions may not compare well with the measured pressure drop for $U_g < U_{mf}$ because the models were developed for drag forces in a state of fluidization.

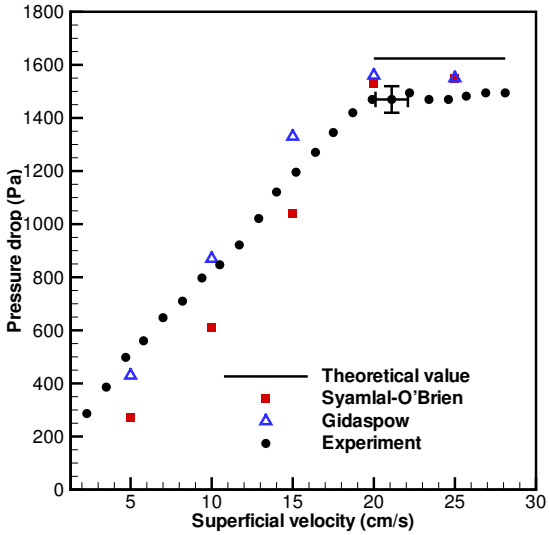

Figure 4.7: Pressure drop versus superficial gas velocity for the glass bead simulations using different drag models and for the experiments.

Figure 4.8 compares the average void fraction in the fluidized bed for both drag models with the results obtained from the CT images. The predictions using the different drag models (Fig. 4.8a,b) are similar to the experiments (Fig. 4.8c,d); however, the Gidaspow model predicts a more uniform distribution across the bed. The void fraction (ϵ_g) at two bed heights of z = 4 and 8 cm are shown in Fig. 4.9; in both cases, the average void fraction is greater for the Gidaspow model. A comparison of the simulations and experiments is also shown in Fig. 4.10, which represents the void fraction averaged across the bed width versus the domain height. The average height of the expanded bed from the experiment is 11.2 cm, while numerical simulations yield an average bed height of 11.1 and 11.3 cm for Syamlal–O'Brien and Gidaspow drag models, respectively.

Of particular interest to this study is the use of a drag model that does not completely require *à priori* information from experiments, e.g., the minimum fluidization velocity. Biomass materials are not well characterized and therefore make computational modeling challenging.

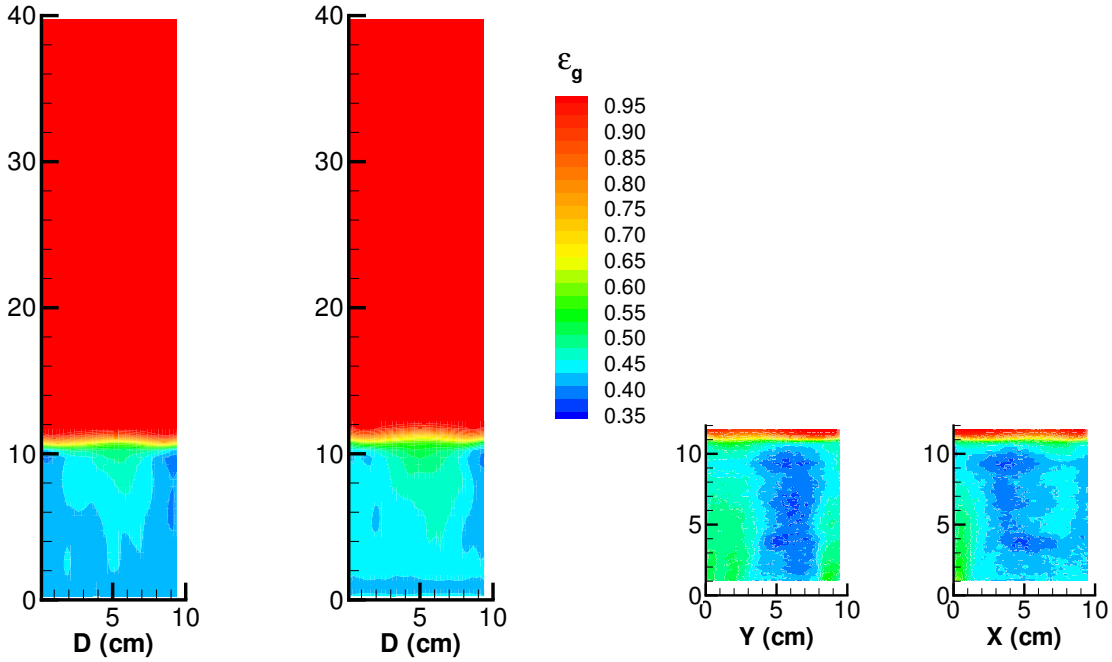

(a) Syamlal-O'Brien (b) Gidaspow (c) X-slice (d) Y-slice

Figure 4.8: Time-averaged void fraction of the glass bead bed from numerical simulation with the (a) Syamlal–O'Brien model and (b) Gidaspow drag model, and CT images for an (c) X-slice and (d) Y-slice.

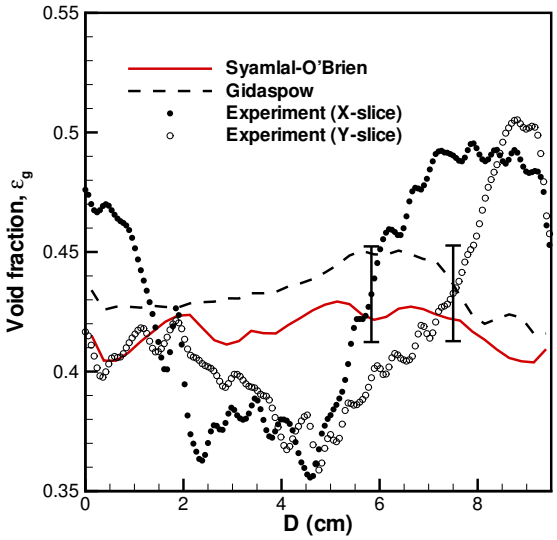

(a) $z = 4$ cm

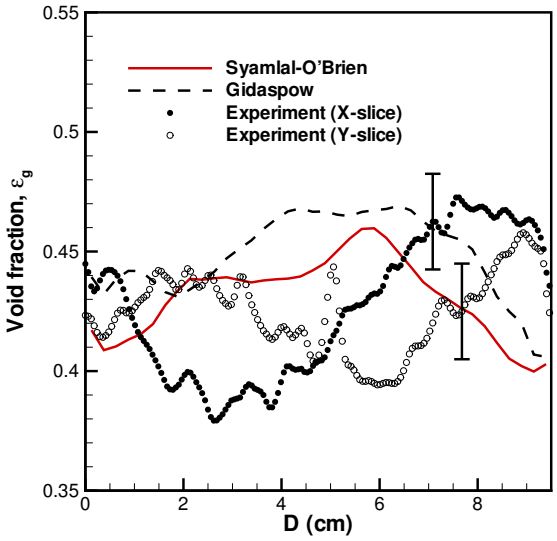

(b) $z = 8$ cm

Figure 4.9: Time-averaged void fraction for the glass bead simulations using different drag models and the experimental data at (a) $z = 4$ cm and (b) $z = 8$ cm.

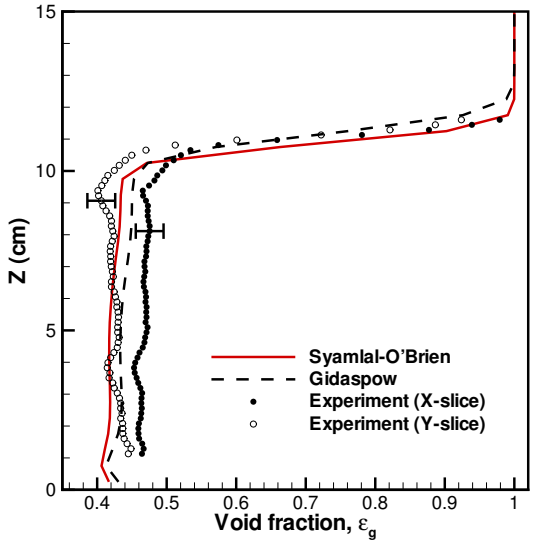

Figure 4.10: Time-averaged void fraction for the glass bead simulations using different drag models and the experimental data spatially averaged across the bed width versus axial direction.

The quantitative comparisons just presented indicate that the Gidaspow model is suitable for modeling fluidized beds and will be used in the parametric study to determine the coefficient of restitution and particle sphericity for biomass. The advantage of the Gidaspow model is that it only requires basic particle properties such as mean diameter and sphericity. However, irrespective of the drag model, the coefficient of restitution is needed for the solid-solid interactions. Thus, the next section explores properties such as sphericity and the coefficient of restitution on biomass fluidization.

4.4.3 Biomass modeling validation

Ground walnut shell particles are used as a case study for a biomass fluidized bed. Particle properties and flow conditions are found in Table 4.1. As a starting point, a qualitative comparison is made between the experiments and simulations. The gas-solid distributions at approximately 10 s intervals are shown in Fig. 4.11. Each subfigure shows images of the radiographs on the left and numerical simulations (using $e = 0.85$ and $\psi = 0.6$) on the right.

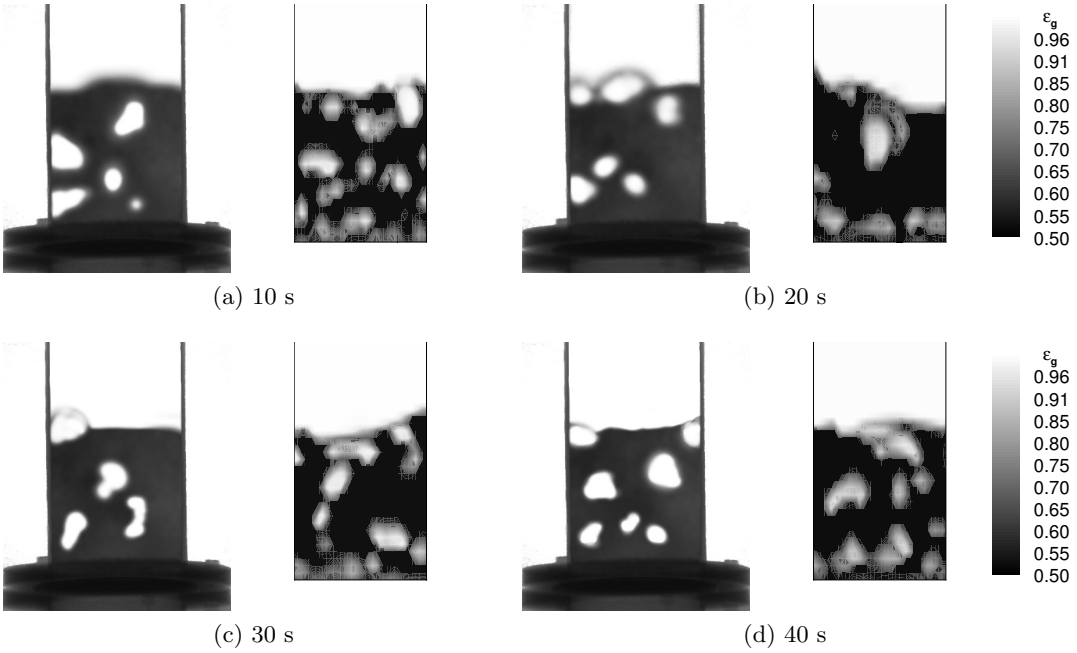

(a) 10 s (b) 20 s

(c) 30 s (d) 40 s

Figure 4.11: Instantaneous gas-solid distributions for the ground walnut shell fluidized bed. For each pair of images, the left side is the X-ray radiograph and the right side is the void fraction contour from the simulation using the the Gidaspow drag model at (a) 10 s, (b) 20 s, (c) 30 s, and (d) 40 s. Note: the gray scale legends are only applicable to the simulations.

The comparisons between experiments and simulations are not at the exact same time but rather in a time frame of ± 1 second. As with the glass bead bed, there is good qualitative agreement with the formation and coalescence of bubbles. The similarities in instantaneous gas-solid distributions between the experiments and simulations provide initial confidence with using the Gidaspow model to predict biomass fluidization.

Pressure drop across the ground walnut shell bed was calculated for a superficial gas velocity of $1.3U_{mf} = 24.3$ cm/s for a combination of coefficients of restitution ($e = 0.75$, 0.85, and 0.95) and particle sphericity ($\psi = 0.5$, 0.6, 0.7, and 0.8) using the Gidaspow drag model. Results from the computational simulations, shown in Fig 4.12, indicate that with a particle sphericity of 0.8, irrespective of the coefficient of restitution, the pressure drop is 500 Pa, compared with 590 Pa for all of the other $\psi - e$ combinations and the experimentally measured value of 570 Pa. The reason that the simulations using a particle sphericity of 0.8 do not compare well

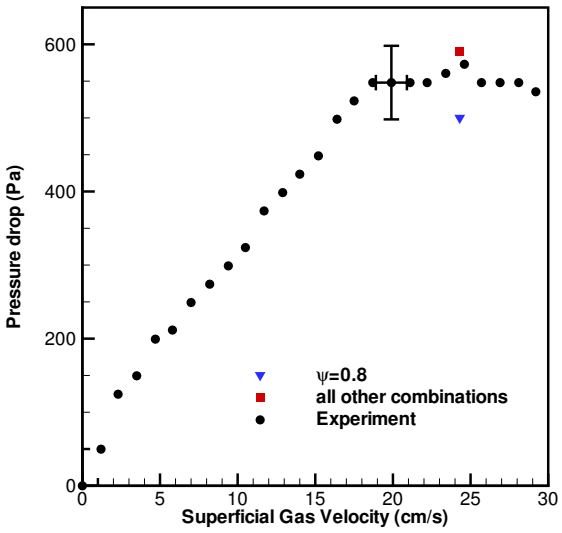

Figure 4.12: Pressure drop versus superficial gas velocity for the ground walnut shell bed experiments and for simulations using the Gidaspow drag model at $U_g = 1.3U_{mf} = 24.3$ cm/s.

is because the bed has not fluidized. As presented in Eqn. (4.12), the sphericity reduces the mean particle diameter; thus, sphericity values smaller than 0.8 represent smaller, more irregular particles that can easily fluidize.

The hydrodynamics of the bed are first analyzed to study the effects of coefficient of restitution with sphericity fixed at 0.6. The coefficient of restitution cannot be easily determined experimentally for the irregular shaped ground walnut shell particles; one way to find a value that best represents the actual coefficient is through a parametric study. The results should provide how sensitive the hydrodynamics are to the coefficient of restitution and how it affects the overall performance of the fluidized bed. Time-averaged void fraction contours from 5 to 40 seconds for the numerical simulations are shown in Fig. 4.13a–c for different coefficients of restitution. No considerable differences are observed between these three results. The parametric study for coefficient of restitution indicates that this variable does not have a significant influence on the bed hydrodynamics for these flow conditions, perhaps due to the lower superficial inlet gas velocity of 1.3 U_{mf}.

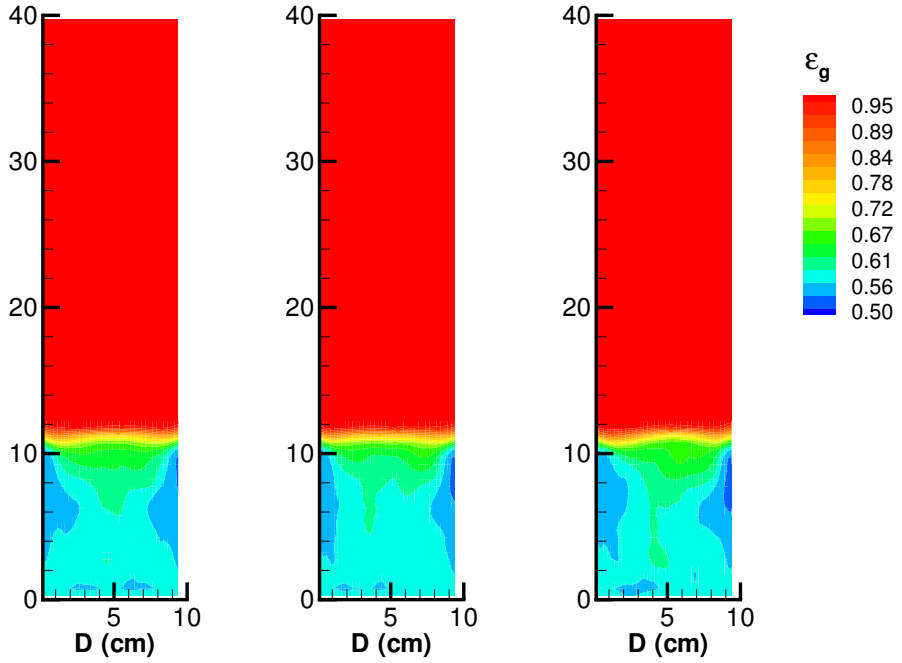

(a) $e = 0.75$ (b) $e = 0.85$ (c) $e = 0.95$

Figure 4.13: Time-averaged void fraction for the ground walnut shell fluidized bed using (a) $e = 0.75$, (b) $e = 0.85$, and (c) $e = 0.95$; $\psi = 0.6$.

Another parameter tested is the biomass particle sphericity. The coefficient of restitution is fixed at 0.85 and the superficial gas velocity is $1.3U_{mf}$. Time-averaged void fraction contours from 5 to 40 seconds for the simulations and two perpendicular planes of the CT scan images are shown in Fig. 4.14. It can be seen that the particles with sphericity of 0.5 and 0.6 tend to have noticeable areas of higher concentration along the walls near $z = 8$ and 6 cm, respectively. The distribution of particles with sphericity of 0.7 is mostly constant throughout the bed. As the sphericity increases, the effective mean particle diameter increases, the particle distribution is more uniform in the bed and the overall bed height decreases. A comparison of the simulations with the experiments is shown in Fig. 4.15, which presents the void fraction averaged across the bed width versus the domain height. The sphericity parametric study indicates that sphericity does change the bed hydrodynamics and is a sensitive value in modeling biomass. Based on the results shown in Fig. 4.15, the numerical simulations compare well with the experiments when $\psi = 0.6$. The average height of the expanded bed from the experiment is 11.3 cm while numerical simulations for particle sphericities of 0.5, 0.6, and 0.7 yielded an average bed height of 12.3, 11.4, and 10.3 cm, respectively.

4.5 Conclusions

Glass beads were used to establish the validity of the multifluid Eulerian-Eulerian model to numerically simulate and predict the hydrodynamics of a fluidized bed. Glass beads were also used to determine an adequate grid resolution and then to validate the Syamlal-O'Brien and Gidaspow drag models. Numerical simulations of the bubbling regime for an inflow gas velocity of $1.3U_{mf}$ were compared to CT and X-ray radiograph images for the gas-solid distribution to demonstrate the qualitative agreement in bubble formation and bed fluidization. The pressure drop, void fraction and mean bed height expansion were in quantitative agreement between the experiments and simulations using both drag models. It was encouraging that the Gidaspow model predictions were in close agreement because the model does not require knowing the minimum fluidization as an input, which is an issue when biomass is the bed material because in practice, the minimum fluidization velocity is not typically known.

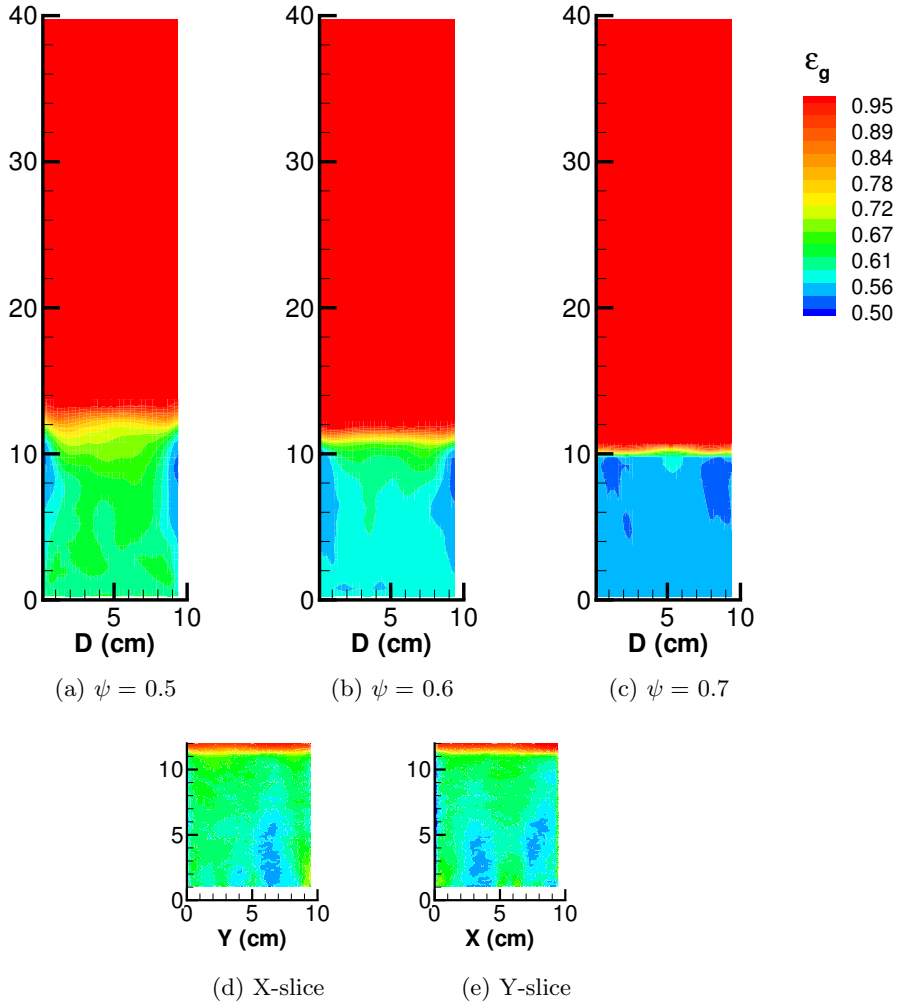

(a) $\psi = 0.5$ (b) $\psi = 0.6$ (c) $\psi = 0.7$

(d) X-slice (e) Y-slice

Figure 4.14: Time-averaged void fraction for the ground walnut shell simulations using (a) $\psi = 0.5$, (b) $\psi = 0.6$, and (c) $\psi = 0.7$ and CT images for an (d) X-slice and (e) Y-slice.

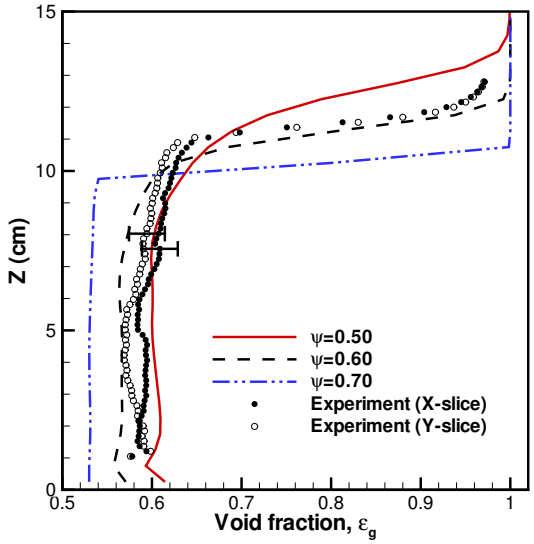

Figure 4.15: Time-averaged void fraction for the ground walnut shell simulations using different particle sphericity and the experimental data spatially averaged across the bed width versus axial direction.

Ground walnut shells were used to represent biomass because the material fluidizes uniformly and is classified as a Geldart type B particle. Simulations of ground walnut shells were analyzed to determine parameters that can not easily be measured experimentally. Both coefficient of restitution and sphericity were varied to determine the effects on the predictions. The coefficient of restitution study showed no significant differences in the hydrodynamics of the fluidized bed for values between 0.75 and 0.95. However, the particle sphericity study showed that sphericity does affect the behavior of the fluidized bed. It was shown that with decreasing sphericity, the bed more readily fluidized because the effective mean particle diameter decreased. Thus, higher sphericity values either underpredicted the bed expansion or the bed did not fluidize, whereas lower sphericities overpredicted the bed expansion.

This research showed qualitative and quantitative comparisons between numerical and experimental data. Although this study is specific to the bed medium, it does demonstrate that biomass can be modeled using the Gidaspow correlations. Furthermore, the parametric study for ground walnut shell indicated that the material can be characterized with a medium

sphericity (≈ 0.6) and a relatively large coefficient of restitution (≈ 0.85).

Nomenclature

C_D	Drag coefficient
CTI	Intensity of the CT scan image
d	Diameter
$\bar{d}$	Mean diameter
e	Coefficient of restitution
F	Coefficient of the interphase momentum transfer
$\mathbf{g}$	Gravitational acceleration
$\mathbf{I}$	Interphase momentum transfer
P	Pressure
$\mathbf{q}$	Diffusive flux of granular energy
Re	Reynolds number
t	Time
$\mathbf{u}$	Velocity vector
U	Fluidization velocity
V_r	Terminal velocity correlation

Greek Letters

ϵ	Volume fraction
ϕ	Transfer of granular energy
φ	Blending function
γ	Rate of granular energy dissipation due to inelastic collisions
λ	Local X-ray attenuation
μ	Dynamic viscosity
θ	Granular temperature
ρ	Density of gas or solid

$\bar{\bar{\sigma}}$	Viscous stress tensor
ψ	Particle sphericity

Superscripts/Subscripts

b	Bulk
g	Gas phase
mf	Minimum fluidization
p	Particle
s	Solid phase

CHAPTER 5. Effects of Mixing using Side Port Air Injection on a Biomass Fluidized Bed

A paper published in *Journal of Fluids Engineering, 133 (11), Paper 111302*

Mirka Deza, Theodore J. Heindel and Francine Battaglia

Abstract

Fluidized beds are being used in practice to gasify biomass to create producer gas, a flammable gas that can be used for process heating. However, recent literature has identified the need to better understand and characterize biomass fluidization hydrodynamics, and has motivated the combined experimental-numerical effort in this work. A cylindrical reactor is considered and a side port is introduced to inject air and promote mixing within the bed. Comparisons between the computational fluid dynamics (CFD) simulations with experiments indicate that three-dimensional simulations are necessary to capture the fluidization behavior of the more complex geometry. This paper considers the effects of increasing side port air flow on the homogeneity of the bed material in a 10.2 cm diameter fluidized bed filled with 500-600 μm ground walnut shell particles. The use of two air injection ports diametrically opposed to each other is also modeled using CFD to determine their effects on fluidization hydrodynamics. Whenever possible, the simulations are compared to experimental data of time-average local gas holdup obtained using X-ray computed tomography. This study will show that increasing the fluidization and side port air flows contribute to a more homogeneous bed. Furthermore, the introduction of two side ports results in a more symmetric gas-solid distribution.

5.1 Introduction

Fluidized bed gasifiers are found in many industrial processes to convert feedstocks with low-carbon content into valuable products such as fuels, basic chemicals, and hydrogen. Some advantages of fluidized bed operation include nearly isothermal conditions due to rapid mixing of particles, high heat and mass transfer rates, and the ability to work with particles of various sizes [1, 3]. The use of biomass in fluidized beds is of current interest because biomass is considered a renewable alternative energy resource that can potentially provide low cost power production or process heating needs. Although biomass gasifiers are being built and used in biorefineries, there are problems with fluidizing the media. Biomass particles are typically difficult to fluidize due to their peculiar shape and a second inert material, such as sand, alumina, or calcite, is typically added to the bed. The large differences in size and density between the biomass and inert particles lead to nonuniform distribution of the biomass within the fluidized bed, and particle interactions and mixing become major issues. Therefore, the fluidization characteristics of biomass particles are of critical importance because of known problems such as particle agglomeration, defluidization, elutriation, and segregation [4–9].

One method to enhance and promote mixing in a fluidized bed is with the inclusion of a side port injection, where either additional gas, biomass or some combination is fed into the reactor bed. There have been studies on the effects of injecting gas through a side port and the influence on fluidization and gasification. Experimental studies of Rajan et al. [36] found that side air injection influenced the circulation pattern of the fluidized bed. Low jet flow promoted mixing and enhanced solid circulation, while high flowrates showed a tendency to increase elutriation, and in small diameter beds, caused slugging. Chyang et al. [37] experimentally studied the modes of gas discharge from a single jet in a two-dimensional (2D) fluidized bed. They identified three regimes for either a bubbling, transition, or jetting flow by comparing a modified Froude number and the ratio of nozzle-to-particle diameter. Chen and Weinstein [38] numerically and experimentally investigated a 2D fluidized bed with horizontal jet injection. They compared solids volume fraction in the jet–influenced area and found three different regions: coherent voids, bubble trains and a zone of surrounding compaction. Another important contribution

was made by Xuereb et al. [39] who experimentally determined the jet penetration length and expansion angle as well as the effects of inlet and jet velocity and particle diameter. They confirmed that close to the injection point, there is a dragging zone of particles from the dense phase into the jet.

Earlier work on horizontal injection mainly focused on finding empirical correlations to measure the jet penetration length [32–34]. Geometric parameters that characterize the injection port (e.g., shape, diameter, and location) and flow conditions such as fluidizing gas velocity and side air injection velocity, have been considered to determine their effects on jet penetration. Hong et al. [35] proposed a correlation for inclined jets, based on Merry's correlation [32] for horizontal jets and validated it with experimental data and numerical simulations using a two-fluid model for fluidization. The influences of gas velocity of the jet, nozzle diameter, inclination, and location were studied in detail. Numerical simulations conducted by Tyler and Mees [40] compared three discretization schemes (hybrid, minmod, and Superbee), and found that simulating the bed with the Superbee scheme resulted in bubble and jet behavior, shape, and formation consistent with what was observed in experiments. From their preliminary study with qualitative comparisons, they concluded that three-dimensional (3D) simulations were in best agreement with experiments. More numerical simulations were performed by Li et al. [41] using a scaled Gilbaro drag model in a 3D cylindrical reactor to avoid overprediction of bed expansion and agglomeration of particles in the bed. Li et al. [42] also investigated the effects of single and multiple jets on the hydrodynamics of a rectangular fluidized bed. They concluded that multiple jets do not influence each other significantly until they start to overlap. Another conclusion was that gas injection strongly affects the fluid behavior of the bed that is above the injection port when the injection flowrate is relatively high, and side effects are negligible in the part below the injection port. It was also shown that deep penetration of the jet enhanced solid circulation in the core; however deeper penetration could lead to a slugging bed flow.

Initially, the use of two-dimensional versus three-dimensional simulations will be compared with experiments to determine the best approach to model and capture the bed hydrodynamics

adequately. From a computational resource point of view, 2D simulations are easier to perform than 3D simulations, but they may not capture the proper physics. Previous work of Xie et al. [74] and Deza et al. [99, 100] have shown very good agreement using a 2D approach for a cylinder reactor with no side air injection when the flow is limited to the bubbling regime for Geldart B particles. To examine the influence of side port air injection, glass beads were used for the bed material in the preliminary studies by Deza et al. [101] and Min et al. [102] because the properties of glass are well-characterized. The simulations for both 2D and 3D representations of the reactor compared well with the experiments. In this work, simulations of a fluidized bed reactor with side port using a medium of ground walnut shell, a Geldart B particle, will be studied to determine if 2D simulations are still appropriate to properly model the fluidization of biomass. This paper considers the effects of increasing fluidization air flow and side port air flow on the homogeneity of the bed material in a 10.2 cm diameter fluidized bed. Two air injection ports diametrically opposite to each other are also considered using CFD to determine how the ports affect the fluidization hydrodynamics. Whenever possible, the simulations are compared to experimental data of time-average local gas holdup obtained using X-ray computed tomography.

5.2 Experimental Setup

5.2.1 Fluidized Bed Reactor

A fluidized bed reactor with a side injection port and an internal diameter (ID) of 10.2 cm is used in the experiments. The three main components of the reactor are the top chamber (freeboard), bed chamber and plenum as illustrated in Fig. 5.1a. The material fluidizes in the bed chamber, which includes a single injection port on the sidewall 2.8 cm from the bottom of the bed chamber. A 1.1 cm ID polypropylene tube is attached to the injection port to supply additional air to improve mixing. The distributor located below the bed is comprised of 62 1-mm diameter holes in a circular grid distribution with approximately 1.3 cm hole spacing. A 45 mesh screen is attached to the distributor plate to avoid particles from accumulating in the holes. Under the distributor plate is the plenum filled with glass marbles to evenly distribute

the fluidizing gas. Above the chamber is a 61 cm tall freeboard region to avoid elutriation of bed material.

Pressure is measured with a 0–34.5 kPa pressure transducer. The pressure transducer is located in the air inlet plate and has a maximum error of ± 86 Pa, which corresponds to ±0.25% of the full scale. Fluidization and side injection air, supplied by the laboratory compressed air system, are controlled using ball valves, pressure regulators, and flow meters. The error of the flow meters is less than ±2% of the full scale reading.

5.2.2 X-ray System

Iowa State University's XFloViz facility was used to image the fluidized bed in this study and has been described in detail in the literature [92]. Consequently, only a brief outline will be presented here. Two LORAD LPX200 portable X-ray tubes provide the X-ray energy. Current and voltage can be adjusted from 0.1 to 10.0 mA and 10 to 200 kV, respectively, with a maximum power of 900 W. Low energy radiation is suppressed by 1 mm thick copper and aluminum filters. In this study, only X-ray computed tomography (CT) imaging is completed. For this purpose, located opposite one of the X-ray sources is a CCD camera connected to a square 44×44 cm cesium-iodide phosphor screen which transforms radiation into visible light. A 50 mm Nikon lens captures images which are digitized by an Apogee Alta U9 CCD system. This system has 3072×2048 pixels and is thermoelectrically cooled to allow long exposure times. Usually, an exposure time of 1 second with 4×4 binning is chosen to minimize acquisition time while maintaining the signal strength. The camera system and X-ray source are located on a 1.0 m ID rotation ring that can rotate 360° around the fluidized bed. CT data are acquired using software developed by Iowa State University's Center for Nondestructive Evaluation (CNDE) and a computer-control data acquisition system. The software allows for control of the camera/detector pair, as well as motion control for the rotation ring. Volumetric reconstruction of the CT images is performed using CNDE's 64-node LINUX cluster.

5.2.3 CT Images

In X-ray computed tomography with a conical X-ray beam, a series of two-dimensional projections are captured at various rotation angles and reconstructed into a three-dimensional volumetric image. Since multiple images must be acquired for one CT, the resulting 3-D image is necessarily time-averaged. This image is a map of CT intensity values which are proportional to X-ray attenuation, which in turn is proportional to density. In this study, only CT images of the fluidized bed filled with ground walnut shell were acquired; this consisted of recording 360 projections, one at every degree, at a power setting of 130 kV and 4.2 mA. For all tests, the exposure time was 1 second at 4×4 binning per degree, and each test took approximately 45 minutes. A total of 300 vertical slices were captured. To minimize image acquisition noise, the CCD camera was cooled to 0°C using the thermoelectric cooler. A pixel non-uniformity calibration was employed [92] to adjust individual pixels to respond identically to incident X-ray energy. After calibration, the 2-D projections were reconstructed into 3-D images using CNDE software.

5.2.4 Gas Holdup

In order to quantify the CT data, time-average local gas holdup (void fraction) was calculated for each flow condition. The time-average local gas holdup, ϵ_g, can be determined by knowing the local X-ray attenuation for the flow (λ), the particle (λ_p), and the gas (λ_g). Since the attenuation is proportional to the CT intensity (CTI), the time-average local gas holdup can be calculated by knowing time-average local CT intensity data for the flow, the particle (CTI_p), and the gas (CTI_g). Therefore, the time-average local gas holdup is defined as:

$$\epsilon_g = \frac{\lambda - \lambda_p}{\lambda_g - \lambda_p} = \frac{CTI - CTI_p}{CTI_g - CTI_p} \tag{5.1}$$

It is difficult to determine the CT intensity for a single particle due to its small size, however, the local CT intensity for a static (bulk) bed of particles (CTI_b) can be used. From Eqn. (5.1), the void fraction for the bulk material can be calculated using local CT intensities for the bed,

where:

$$\epsilon_{g,b} = \frac{CTI_b - CTI_p}{CTI_g - CTI_p} \tag{5.2}$$

For a granular material, the void fraction of the bulk material ($\epsilon_{g,b}$) is defined as:

$$\epsilon_{g,b} = 1 - \frac{\rho_b}{\rho_p} = \text{Constant} \tag{5.3}$$

The bed material bulk density (ρ_b) and particle density (ρ_p) can be found experimentally and in property tables, respectively. Substituting CTI_p from Eqn. (5.2) into Eqn. (5.1) and rearranging yields an equation to determine the local gas holdup based on CTs for the flow condition, the gas, and the bulk material:

$$\epsilon_g(i,j,k) = \frac{CTI(i,j,k) - CTI_b(i,j,k) + [CTI_g(i,j,k) - CTI(i,j,k)]\epsilon_{g,b}}{CTI_g(i,j,k) - CTI_b(i,j,k)} \tag{5.4}$$

and i, j, k represent the locations of individual voxels in the three-dimensional (3-D) volume, where a voxel is a 3-D pixel. In this study, CT data were acquired for a bed of static bulk material and the empty reactor (air only) at identical power settings used to capture fluidization (flow) CT data. Using Eqn. (5.4), each flow file was converted to show time-average local gas holdup and a smoothing method was employed to reduce noise. The resulting time-average gas holdup values are determined on a 3-D grid with an approximate voxel size of 0.6 mm $\times$ 0.6 mm $\times$ 0.6 mm. Estimated absolute uncertainly in the local gas holdup is $\pm$ 0.04, which is a worst-case estimate with most data falling within an absolute gas holdup error of $\pm$ 0.02.

Three-dimensional images were viewed using internally developed visualization software, which allowed viewing of the volumetric images at any location within the imaging volume, and to adjust color mapping schemes. Since volume files contain information outside the cylindrical region of interest, a clipping feature was also used to isolate the fluidized bed. Once isolated, the spatial range was modified to show the vertical $y-z$ plane (x-slice) and the vertical $x-z$ plane (y-slice) through the column center, as well as horizontal $x-y$ planes (z-slices) at heights of 3.2 cm and 9.0 cm from the distributor plate.

5.3 Two-Fluid Model

5.3.1 Governing Equations

A multifluid Eulerian-Eulerian model is employed in Multiphase Flow with Interphase eXchanges (MFIX) [71] and assumes that each phase behaves as interpenetrating continua with its own physical properties. The instantaneous variables are averaged over a region that is larger than the particle spacing but smaller than the flow domain. Volume fractions are introduced to track the fraction each phase occupies in the averaging volume, where ϵ_g is the gas phase volume fraction (also referred to as the void fraction) and ϵ_s is the solid phase volume fraction. The solid phase is described with an effective particle diameter d_p and characteristic material properties, and solved using conservation equations for the solid phase. The effective particle diameter is $d_p = \psi \bar{d}_p$, where $\bar{d}_p$ is the mean diameter and ψ is the estimated sphericity of the actual particles.

The continuity equations for the gas phase (g) and the solid phase (s), respectively, are:

$$\frac{\partial}{\partial t}(\epsilon_g \rho_g) + \nabla \cdot (\epsilon_g \rho_g \mathbf{u}_g) = 0 \tag{5.5}$$

$$\frac{\partial}{\partial t}(\epsilon_s \rho_s) + \nabla \cdot (\epsilon_s \rho_s \mathbf{u}_s) = 0 \tag{5.6}$$

with density ρ and velocity vector $\mathbf{u}$.

The momentum equations for the gas and solid phases have the form:

$$\begin{aligned} \frac{\partial}{\partial t}(\epsilon_g \rho_g \mathbf{u}_g) &+ \nabla \cdot (\epsilon_g \rho_g \mathbf{u}_g \mathbf{u}_g) \\ &= -\epsilon_g \nabla P_g + \nabla \cdot \bar{\bar{\sigma}}_g + \mathbf{I}_g + \epsilon_g \rho_g \mathbf{g} \end{aligned} \tag{5.7}$$

$$\begin{aligned} \frac{\partial}{\partial t}(\epsilon_s \rho_s \mathbf{u}_s) &+ \nabla \cdot (\epsilon_s \rho_s \mathbf{u}_s \mathbf{u}_s) \\ &= -\epsilon_s \nabla P_g + \nabla \cdot \bar{\bar{\sigma}}_s - \mathbf{I}_g + \epsilon_s \rho_s \mathbf{g} \end{aligned} \tag{5.8}$$

where $\bar{\bar{\sigma}}$ is the stress tensors, $\mathbf{g}$ is gravity, and $\mathbf{I}$ the interaction forces accounting for the momentum transfer between the gas and solid phases.

The granular temperature θ for the solid phase can be related to the granular energy, defined as the specific kinetic energy of the random fluctuating component of the particle

velocity. The resulting transport equation for the granular energy [72] is:

$$\frac{3}{2}\left[\frac{\partial}{\partial t}(\epsilon_s \rho_s \theta) + \nabla \cdot (\epsilon_s \rho_s \theta)\mathbf{u}_s\right] = \bar{\bar{\sigma}}_s : \nabla \mathbf{u}_s \\ -\nabla \cdot \mathbf{q}_\theta - \gamma_\theta + \phi_g \tag{5.9}$$

where $\mathbf{q}_\theta$ is the diffusive flux of granular energy, γ_θ is the rate of granular energy dissipation due to inelastic collisions [73], and ϕ_g is the transfer of granular energy between the gas phase and solid phase.

Kinetic theory for granular flow is used to calculate the solid stress tensor and solid-solid interaction force in the rapid granular flow regime [71]. There are two distinct flow regimes in granular flow: a viscous or rapidly shearing regime in which stresses arise due to collisional or translational momentum transfer, and a plastic or slowly shearing regime in which stresses arise due to Coulomb friction between solids in close contact. A blending function to provide a smooth transition between each regime is employed [74]. Further details related to the constitutive relations in Eqns. (5.7-5.9) can be found in the MFIX theory guide [71].

The interaction force accounts for the gas-solid momentum transfer, which is expressed as the product of the coefficient for the interphase drag force between the gas and solid phases and the slip velocity. The Gidaspow model [81] is used to represent the interphase drag force coefficient based on the Ergun and Wen-Yu equations, with a blending function to avoid a discontinuity between the use of the equations. Previous studies by the authors have shown the validity of using the model for glass beads and ground walnut shell [103].

5.3.2 Solution Methodology

To discretize the governing equations in MFIX, a finite volume approach for a staggered grid is used to reduce numerical instabilities [90]. Velocities are stored at the cell surfaces, and scalars, such as void fraction and pressure, are stored at the center of the cell. Discretization of time derivatives are first-order and discretization of spatial derivatives are second-order. An important feature is the use of a second-order discretization scheme for the convective terms, known as the Superbee method [95], which improves convergence and accuracy of the solution. A modification of the SIMPLE algorithm is used to solve the governing equations [90]. The

first modification uses an equation for the solid volume fraction that includes the effect of the solids pressure to help facilitate convergence for a both loosely and densely packed regions. The second modification uses a variable time-stepping scheme to improve convergence and execution speeds.

5.4 Results and Discussion

5.4.1 Problem Description

The schematic of the fluidized bed reactor used in the experiments is shown in Fig. 5.1a and the simulations model the bed chamber shown in Fig. 5.1b. For all simulations, air is uniformly provided at the bottom of the domain equal to the superficial gas velocity as a simplification of the flow across the distributor plate in the experiments. The side port injection is also modeled with uniform air velocity at the inlet. The no-slip condition is used to model the gas-wall interactions and a partial-slip condition is used for the particle-wall interactions [83]. Table 5.1 summarizes the ground walnut shell particle properties and flow conditions. To account for the nonspherical nature of the ground walnut shell (it is more chunk-like), the sphericity and coefficient of restitution were numerically estimated based on previous work by Deza et al. [103], whereas the other properties were provided from the experiments. Two inlet gas velocities are examined; the lower velocity of $U_g = 1.5U_{mf}$ represents a mild bubbling bed and the higher velocity of $U_g = 3.0U_{mf}$ represents a moderate industrial reactor flowrate [104], where U_{mf} is the minimum fluidization velocity. A base case with no side port air injection ($Q_{side} = 0$) and two additional cases of $Q_{side} = 5\%$ and $10\%Q_{mf}$ are studied, where Q_{mf} is the minimum fluidization volumetric flowrate based on the bed inlet characteristics. Finally, a comparison using two ports diametrically opposite to each other with $5\%Q_{mf}$ air is studied; however, this particular case is only explored numerically to demonstrate the effects of multiple ports in enhanced mixing.

The grid resolution study by Deza et al. [103] identified a sufficient number of cells that would produce an estimated numerical error less than 1%. The study was for a two-dimensional domain, where a total of 2400 grid cells provided adequate resolution of the domain. The

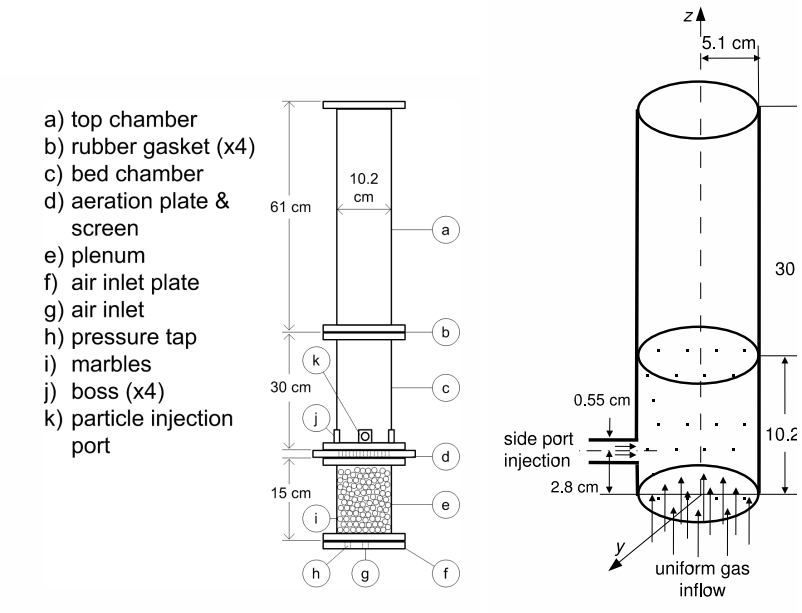

(a) (b)

Figure 5.1: Schematic of the (a) fluidized bed used in the experiment and (b) bed chamber used in the simulation including the side port injector.

Table 5.1: Properties and flow characteristics for walnut shell

particle diameter, $\bar{d}_p$ (cm)	0.055
particle density, ρ_p (g/cm^3)	1.3
bulk density, ρ_b (g/cm^3)	0.579
sphericity, ψ (–)	0.6
coefficient of restitution, e (–)	0.85
initial void fraction, ϵ_g^* (–)	0.555
minimum fluidization velocity, U_{mf} (cm/s)	18.4

work herein uses a resolution for the 3D domain with 40×60 cells in the radial and axial directions and 16 cells in the azimuthal direction that form parallelepiped cells due to the circular cross-section of the domain. Although the grid resolution may seem coarse, Table 5.2 compares the computational time required for simulations performed on an AMD Opteron cluster (dual processor, dual core 2.4 GHz AMD 280 Opteron). The time-step used by MFIX automatically adjusts to help the simulation converge. The mean time-step for a 3D simulation with $3.0U_{mf}, 10\%Q_{mf}$ was on the order of 0.00024 s. The simulations are time-averaged from 5 to 65 s (which represents the average of 6000 time-steps).

5.4.2 Two- and Three-Dimensional Simulations

The pressure drop across the ground walnut shell-filled fluidized bed versus the superficial gas inlet velocity when $Q_{side} = 0$ (base case) is shown in Fig. 5.2. The results compare the experimental measurements to that predicted using MFIX. Error bars are shown for both pressure and velocity on a sample of data to mantain clarity of the data presented. Once the bed is fluidized at $U_{mf} = 18.4$ cm/s, the measured pressure drop is approximately constant at 470 ± 86 Pa [105] whereas the predicted pressure drop is approximately 560 Pa. CFD modeling predicts the same pressure drop through the bed for both two- and three-dimensions. It should be noted that the the slight discrepancy of CFD predictions with experiments may be due to error associated with the irregular particle sizes for ground walnut shell. Furthermore, the simulations modeled a single particle diameter of 550 μm, whereas the experiments used ground walnut shell particles with diameters ranging from $500 - 600$ μm. It is particularly encouraging that for the base case, the 2D and 3D simulations are almost identical.

Figure 5.3(a-c) presents contours of the void fraction for the fluidized bed at $U_g = 1.5U_{mf}$ and $Q_s = 10\%Q_{mf}$. The 2D and 3D simulations, Fig. 5.3a and c, respectively, are compared to the experiments (Fig. 5.3b) using an interrogation region up to $z = 15$ cm and the bed diameter. The contours for the experiment and 3D simulation correspond to the $x - z$ plane (see Fig. 5.1b) through the bed centerline and injection port. Also shown is void fraction averaged along horizontal planes, which produce a spatial average that can vary in the axial

Table 5.2: Central processing unit information

	2D	3D
CPU time (s)	155,200	4,155,000
# time-steps	144,860	272,100
average Δt (s)	0.00044	0.00024
# cells	2400	19,200
μs/time-step/cell	446	795

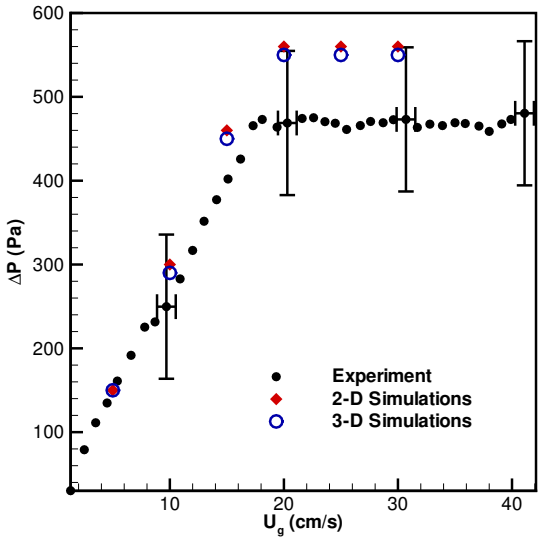

Figure 5.2: Pressure drop versus superficial gas velocity comparing experiments and simulations for the fluidized bed with no side port (Q_{side} =0).

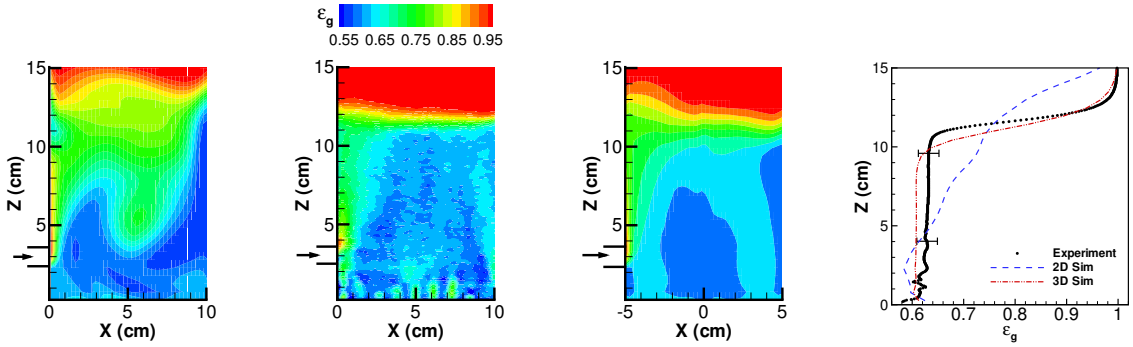

(a) 2D simulation (b) experiment (c) 3D simulation (d) x-average

Figure 5.3: Time-average void fraction of the fluidized bed at U_g=1.5U_{mf} and Q_s=10%Q_{mf} for the (a) 2D simulation, (b) experiment, (c) 3D simulation, and (d) horizontal averages across the reactor diameter versus axial direction.

direction. Therefore, the curve in Fig. 5.3d shows the horizontal-average void fraction versus axial direction, and identifies that the bed expands to approximately 11 cm after fluidization. For the 2D simulation, time-average void fraction was horizontally-averaged across the bed width, while for the experiment and 3D simulation, horizontal averaging was performed for the the $x-y$ plane (circular cross-section). These side-by-side comparisons help elucidate the hydrodynamic features between both the 2D and 3D simulations and their agreement with the experiments. The side port air injection tends to cause a slight nonuniformity of the fluidized media near the port, which is accompanied by higher void fraction (i.e., more gas). Overall the bed uniformly fluidizes; this feature is observed in the experiment and the 3D simulation also predicts the same fluidization hydrodynamics. The 2D simulation predicts relatively uniform fluidization, however, there is more gas present within the center of the bed, displacing the solid particles. Figure 5.3d confirms that the 2D simulation predicts higher void fraction, which increases from 0.6 to 0.7 within the fluidizing bed. The 3D simulation predicts slighly lower void fraction but it is very uniform, as indicated by the constant value of 0.6; the average void fraction measured in the experiment is 0.62. The error bars on the experimental data represent an absolute gas holdup error of ±0.02, which is typical of most data.

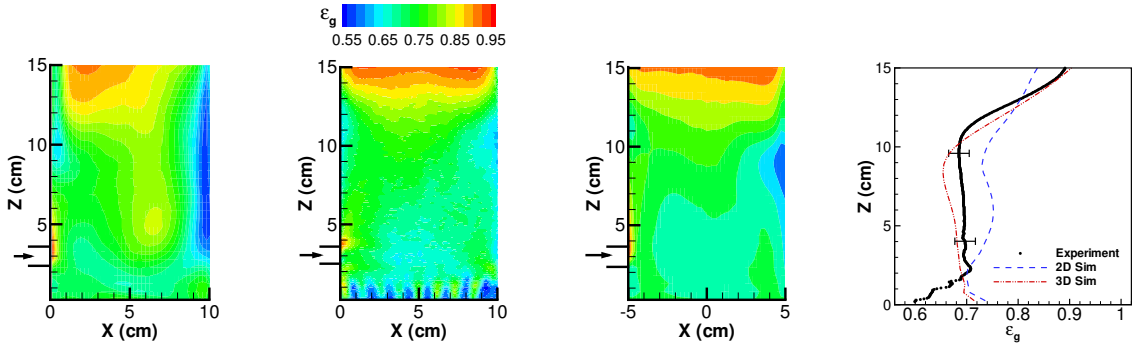

(a) 2D simulation (b) experiment (c) 3D simulation (d) x-average

Figure 5.4: Time-average void fraction of the fluidized bed at U_g=3.0U_{mf} and Q_s=10%Q_{mf} for the (a) 2D simulation, (b) experiment, (c) 3D simulation, and (d) horizontal averages across the reactor diameter versus axial direction.

The case for $U_g = 3.0U_{mf}$ and $Q_s = 10\%Q_{mf}$ is shown in Fig. 5.4. Examining the 2D void fraction contours (Fig. 5.4a), the nonuniformity of the fluidization is very apparent near the bed expansion height of 15 cm. The 3D simulation (Fig. 5.4c) compares remarkably well with the experiment (Fig. 5.4b), which is very encouraging because the inlet gas velocity U_g is large. The larger inlet gas velocity in combination with the side air injection suggests improved mixing throughout the bed, with a mean void fraction of 0.7. The 3D simulation slightly underpredicts the hydrodynamics, however, these discrepancies are most likely attributed to the single particle size used in the computational modeling or the estimate for the particle sphericity.

In an effort to further quantify and contrast the simulations with the experiments, time-average void fraction profiles at two axial locations, $z = 3.2$ and 9.0 cm, are shown in Fig. 5.5 at $3.0U_{mf}$ for $10\%Q_{mf}$. The experimental data and 3D simulations are local time-average values along a ray that passes through the centerline of the bed and side injection port at the given z height. The variations in the experimental data are attributed to the nonuniform inlet conditions that result from the 62 discrete air inlet holes of the distributor plate, and similar discrepancies have been shown by others [29,30,96,97]. The 3D prediction compares very well

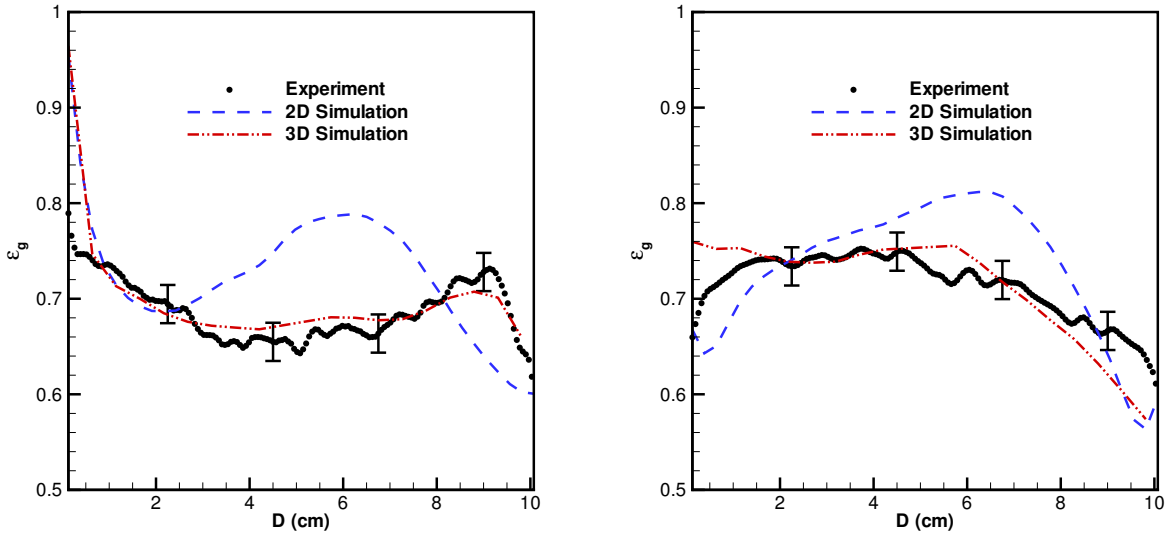

(a) $z = 3.2$ cm

(b) $z = 9.0$ cm

Figure 5.5: Time-average void fraction profiles of the fluidized bed at U_g=3.0U_{mf} and Q_s=10%Q_{mf} at (a) $z = 3.2$ cm and (b) $z = 9.0$ cm. Experimental data shown as symbols and simulations are shown as lines.

with the experiment, whereas the 2D simulation significantly overpredicts the presence of gas near the lower region of the bed (Fig. 5.5(a)).

Figures 5.3−5.5 elucidate the importance of modeling a 3D domain to capture the hydrodynamics for fluidizing biomass with side air injection. While 2D modeling is reasonable for midly bubbling beds (e.g., 1.5U_{mf}), it is not sufficient when simulating higher flow rates (e.g., 3U_{mf}), especially for reactors with side port injection. The most likely reason is the lack of freedom for the particles to move azimuthally, thus limiting the validity for using a two-dimensional domain. Therefore, the remainder of the discussion presents numerical results based on modeling the full three-dimensional domain.

5.4.3 Side Injection Flowrate

It has been established that injecting air through a horizontal port promotes mixing in the fluidized bed. The effects of increasing side injection rate at a moderate inlet velocity of 3.0U_{mf} will be examined next. Three side injection flowrates of 5%Q_{mf}, 10%Q_{mf}, and 20%Q_{mf} are

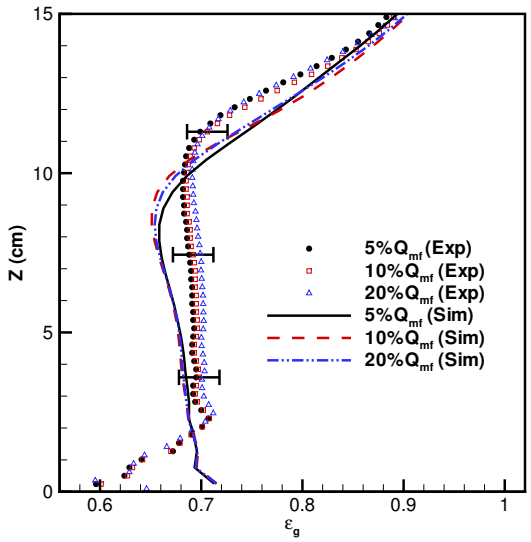

Figure 5.6: Time-average void fraction for the $3.0U_{mf}$ fluidized bed and side port injection flowrates of $Q_{side} = 5$, 10 and $20\%Q_{mf}$ horizontally-averaged across the reactor diameter. Experimental data shown as symbols and simulations are shown as lines.

presented in Fig. 5.6 for the time-average void fraction horizontally-averaged across the reactor diameter ($x-y$ plane). Results from the experiments are shown as symbols and lines are used for the simulation data. In general, the mean void fraction trends are very similar, irrespective of side port air flowrate. With increasing axial position, the mean void fraction is relatively uniform until 10 cm, above which the void fraction gradually increases from 0.7 to 0.9 by 15 cm. Furthermore, the comparisons between the simulations and experiments are in good agreement.

To better understand the mixing trends, simulations and experiments are shown in Figs. 5.7 (a)–(c) as contour plots of the void fraction for the centerplane of the cylindrical reactor through the injection port ($x-z$ plane) as well as two circular cross-sections ($x-y$ planes) located at heights of $z = 3.2$ cm (lower row) and 9.0 cm (upper row). For each case, experiments are on the left and 3D simulations on the right. The gas-solid distribution throughout the centerplane does not vary significantly with increasing side injection, except for the region near the port, where higher void fractions are present for higher side port air injection rates. The circular cross-sections at $z = 3.2$ cm show higher void fractions because additional air

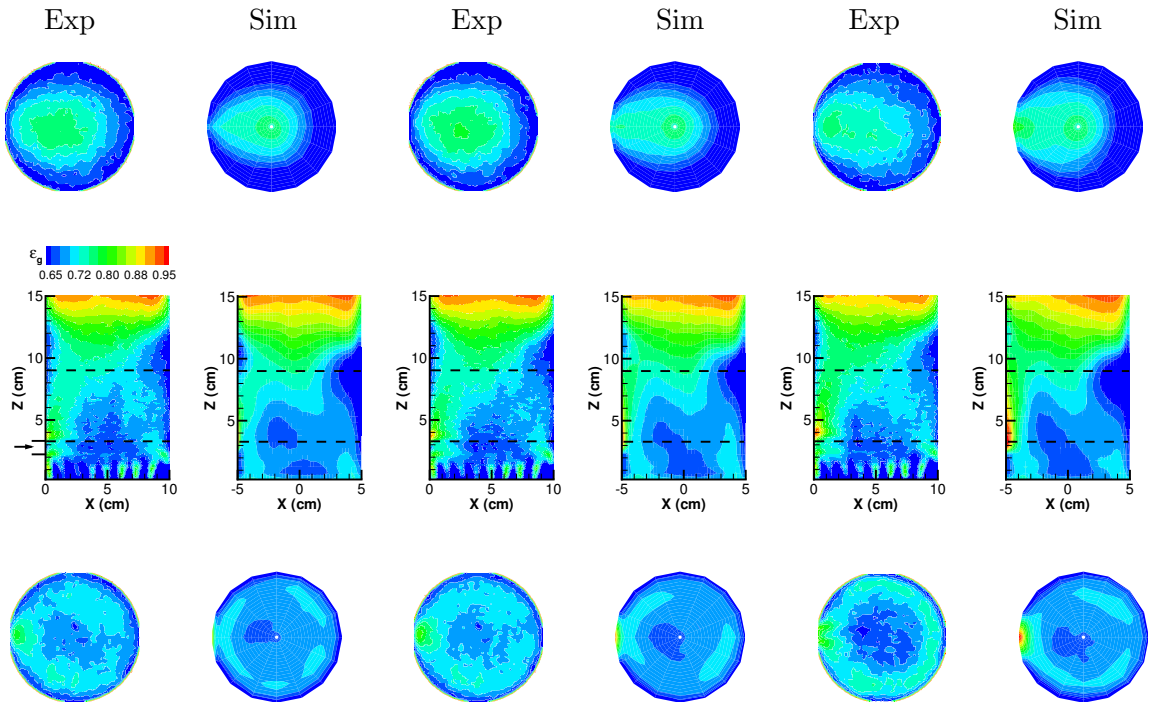

(a) $5\%Q_{mf}$ (b) $10\%Q_{mf}$ (c) $20\%Q_{mf}$

Figure 5.7: Time-average void fraction for the $3.0U_{mf}$ fluidized bed using side injection flowrates of (a) $5\%Q_{mf}$, (b) $10\%Q_{mf}$, and (c) $20\%Q_{mf}$. Upper row: circular cross-sections at $z = 9.0$ cm ($x - y$ plane), middle row: centerplanes through the port ($x - z$ plane), and lower row: circular cross-sections at $z = 3.2$ cm ($x - y$ plane).

injected through the port is present near this height. Annular sections of higher solid volume fraction are observed at $z = 9.0$ cm because the particles tend to move toward the wall opposite to the port. The same trend is observed in both the experiments and simulations.

5.4.4 One versus Two Injection Ports

Injection flowrates of 5% and $10\%Q_{mf}$ through one port and $5\%Q_{mf}$ through two ports (for a total of $10\%Q_{mf}$) have been further compared in Fig. 5.8 for the void fraction averaged across the reactor diameter versus axial direction. As previously mentioned, only one side port was manufactured for the reactor used in the experiments. Results from the experiments are shown as symbols (only for $5\%Q_{mf}$ and $10\%Q_{mf}$ through one side port) and lines are used for the simulation data. As was observed in Fig. 5.8, the simulations are in good agreement with

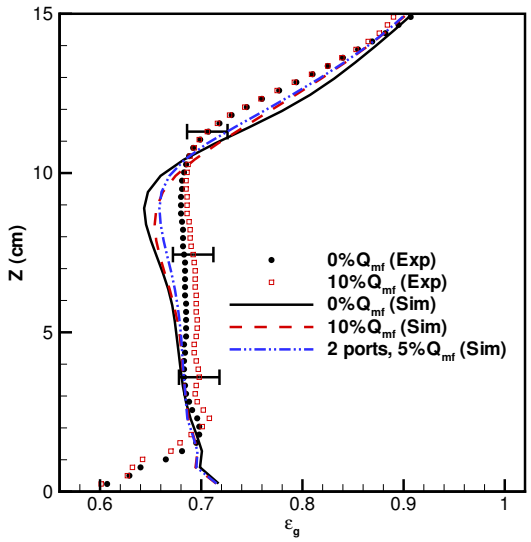

Figure 5.8: Time-average void fraction for the $3.0U_{mf}$ fluidized bed and side port injection flowrates of $Q_{side} = 0$, $10\%Q_{mf}$ and 2 ports with $5\%Q_{mf}$ through each port horizontally-averaged across the reactor diameter. Experimental data shown as symbols and simulations are shown as lines.

the experiments and the void fraction is relatively uniform through the bed. When comparing spatially and temporally average values, the effects of two side injectors is not sufficient for this fluidization flow rate.

Time-average local values, however, are affected by the number of side air injection ports. Figure 5.9(a)–(c) shows contour plots of the void fraction for no side port ($Q_{side} = 0$), one side air injection port with $10\%Q_{mf}$, and two side air injection ports each with $5\%Q_{mf}$, respectively. With one injection port the particles move toward the opposite wall. However, two side air ports diametrically opposed improve the gas-solid distribution in the bed and eliminates the asymmetry of the flow.

To further quantitatively compare 3D simulations with the experiments, time-average void fraction profiles at two axial locations, $z = 3.2$ and 9 cm, are shown in Fig. 5.10 for the same cases. Overall, the 3D predictions for local void fraction profiles compare well with the experiments. The void fraction is uniform at lower axial locations (Fig. 5.10(a)) irrespective of

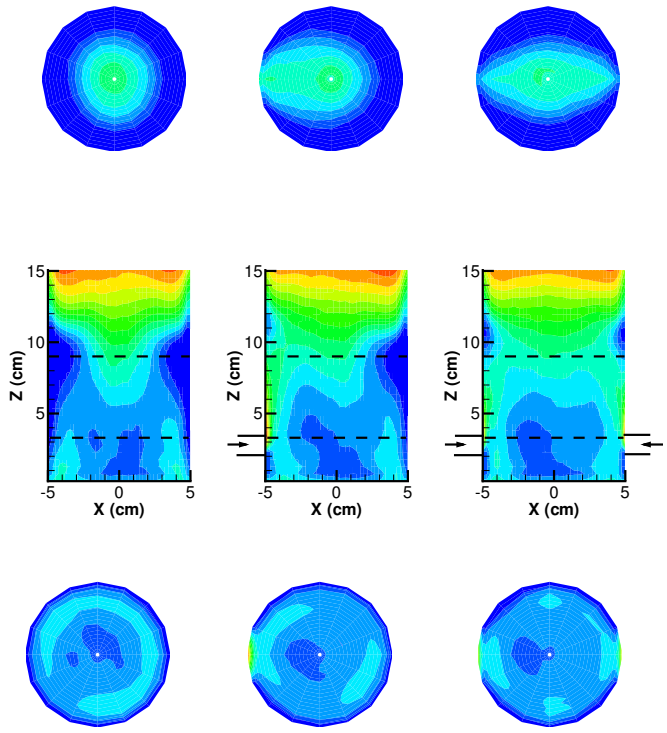

(a) $0\%Q_{mf}$ (b) $10\%Q_{mf}$ (c) 2 ports, $5\%Q_{mf}$

Figure 5.9: Time-average void fraction predictions for the $3.0U_{mf}$ fluidized bed using side injection flowrates of (a) $0\%Q_{mf}$, (b) $10\%Q_{mf}$, and (c) 2 ports with $5\%Q_{mf}$ each. Upper row: circular cross-sections at $z = 9.0$ cm ($x - y$ plane), middle row: centerplanes through the port ($x - z$ plane), and lower row: circular cross-sections at $z = 3.2$ cm ($x - y$ plane).

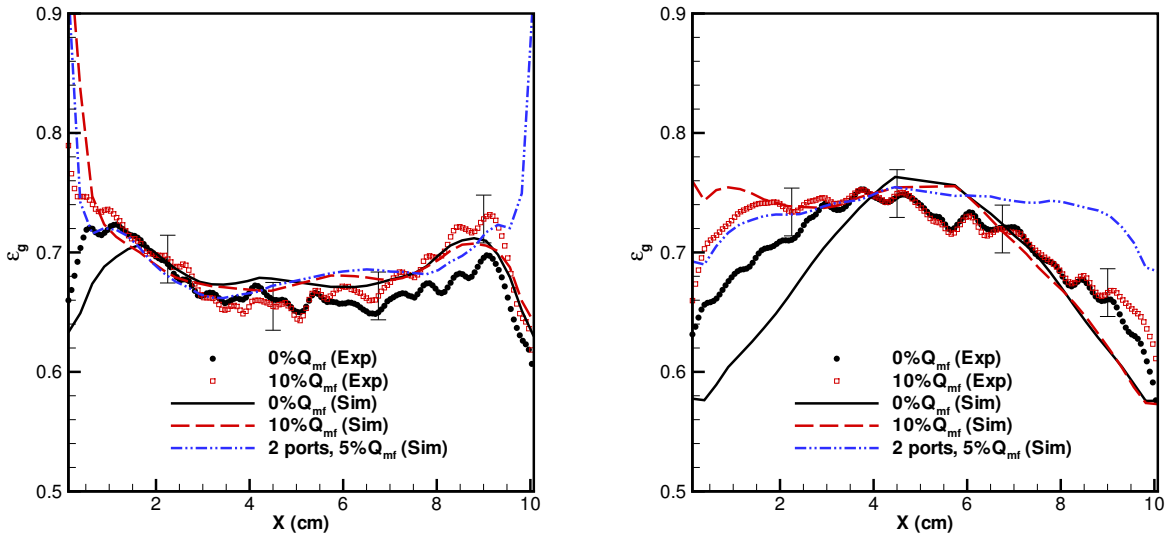

(a) z = 3.2 cm

(b) z =9.0 cm

Figure 5.10: Time-average void fraction profiles of the $3.0U_{mf}$ fluidized bed with side port injection flowrates of $Q_{side} = 0\%$ and $10\%Q_{mf}$ and 2 ports with $5\%Q_{mf}$ through each port at (a) z = 3.2 cm and (b) z = 9.0 cm. Experimental data shown as symbols and simulations are shown as lines.

the side port, but the side ports tend to promote more uniform gas-solid distribution at higher axial locations (Fig. 5.10(b)).

This study has demonstrated how side port injection affects the mixing characteristics of the fluidizing bed. In practice, industrial reactors rely on side ports to inject additional gas as well as biomass (or other granular material like coal). However, as was shown, a single port can adversely affect the homogeneity of the fluidizing material. These results elucidate that a second port may be advantageous to ensure proper mixing, which is extremely important for gasification to yield high quality producer gas. Future work will examine gasification of biomass and the effect of side port injection.

5.5 Conclusions

Numerical simulations of a biomass fluidizing bed with side air injection were compared to CT data for the gas-solid distribution to demonstrate the quantitative agreement for bed fluidization. Ground walnut shells in the range size of 500–600 μm were used to represent

biomass because the material fluidizes uniformly and is classified as a Geldart type B particle. An Eulerian-Eulerian multifluid model was used to simulate and analyze gas-solid hydrodynamic behavior of the fluidized bed. Two- and three-dimensional simulations were performed to determine if both modeling approaches would capture the salient bed features. The predictions for pressure drop through the biomass bed were initially validated with the experiments and were found to be in good agreement. The findings showed that 2D simulations overpredicted the fluidized bed expansion and the results did not demonstrate a uniformly fluidizing bed. The 3D simulations compared well for all cases. This study demonstrates the importance of using a 3D model for a truly 3D flow in order to capture the hydrodynamics of the fluidized bed for a complicated flow and geometry.

The effects of increasing side port air flow on the homogeneity of the bed were investigated next. It was found that increasing the side port injection flowrate up to $20\%Q_{mf}$ for a single port did not significantly affect the behavior of the bed, and the simulations compared well with the experimental measurements of void fraction. However, the simulations showed that adding a second side port injector on the opposite side of the reactor improved the mixing and overall homogeneity of the fluidized material. It would be of interest to study the effects of adding additional ports along the circumference of the reactor to further study their effect on the homogeneity of the bed.

Acknowledgments

The authors would like to extend their thanks to Mr. Nathan Franka of Iowa State University for providing the experimental data used in this work.

CHAPTER 6. Pressure Fluctuation Analysis in Fluidized Beds

Pressure fluctuation analysis has extensively been used to study the hydrodynamic features of fluidized beds and they are usually related to the motion of bubbles within the bed. Pressure can be easily measured, especially in tough industrial conditions, and pressure measurement systems are considered relatively non-intrusive, low-cost, robust, and reliable. However, analysis of the pressure data is rather complicated. Analysis of pressure fluctuations can be grouped according to their domain in time-, frequency-, and space-domain analysis. For these studies, time- and frequency-domain analyses have been used to characterize fluidized beds in different fludization regimes. In the time domain, plotting a sequence of pressure data points is the simplest method of analysis. Another method that has been broadly used is the estimation of the standard deviation of the pressure signals. Power spectral density (PSD) is a frequency-domain analysis to find dominant frequencies in the pressure data and relate them to physical phenomena.

Pressure fluctuation analyses have been widely reported with experimental data and a few researchers have used CFD to analyze pressure fluctuation in fluidized beds. The objective of this research is to demonstrate that pressure fluctuation analysis using CFD can be used in the characterization of fluidized bed regimes, thus providing a tool to analyze and design different configurations and operation conditions while avoiding high-cost pilot plants and experiments in laboratories. To achieve that, numerical simulations have been validated with experiments by Zhang et al. [13, 14].

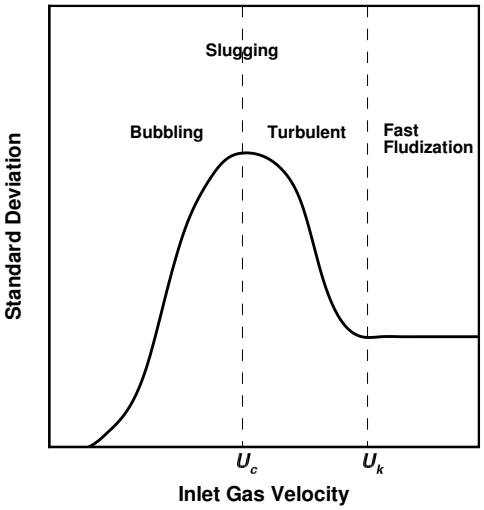

Figure 6.1: Standard deviation of pressure fluctuations versus inlet gas velocity.

6.1 Pressure Fluctuation Analysis

6.1.1 Standard Deviation

Standard deviation has often been used to identify different fluidization regimes in fluidized beds, where a maximum value with respect to inlet gas velocity is associated with the transition from the bubbling to turbulent regime. Standard deviation has also been used to determine minimum fluidization velocity [44–47] and to detect the onset of defluidization in operating fluidized beds [48]. The method of analysis has been widely used by many researchers. Bi and Grace [49] and Bi et al. [50–52] extensively studied the use of standard deviation to determine the transition to a turbulent fluidization regime. Two velocities, U_C and U_K, were identified as delimiters for regime transition. U_C marks the transition from a bubbling to turbulent fluidization regime and occurs when the standard deviation reaches its maximum. The transition is also known as the slugging regime. U_K marks the transition from a turbulent to a fast fluidization regime, where the standard deviation remains approximately constant. A schematic of the general trend of a standard deviation plot showing the transition velocities can be seen in Fig. 6.1.

The standard deviation (σ) for a time-series of pressure data, $p_i (i = 1, 2, ..., N)$, is:

$$\sigma = \sqrt{\frac{1}{N-1}\sum_{i=1}^{N}(p_i - \bar{p})^2} \tag{6.1}$$

where $\bar{p}$ is the average pressure for N time realizations.

6.1.2 Power Spectral Density (PSD)

Another tool for studying pressure data is frequency domain analysis, which is performed using a Fourier transform. A method for obtaining the frequencies associated with a system is power spectral density (PSD). The objective is to determine dominant frequencies in the time-series and relate them to physical phenomena [53]. Other authors have used PSD to validate dynamic similitude and scale-up by comparing spectra of models, prototypes, and full-scale units [16,54]. Using a Gaussian curve, Parise et al. [55] fitted power spectra to detect defluidization of the bed based on changes in the average pressure and the standard deviation.

A complete formulation of spectral analysis for random processes can be found in [106] and a summary of the main equations is shown in this work. The power spectral density function (S_{yy}) can be defined as the Fourier transform of the autocorrelation function (R_{yy}) of a continuous time series ($y(t)$):

$$S_{yy}(i\omega) = \int_{-\infty}^{+\infty} R_{yy}(\tau)\exp^{(-i\omega\tau)}\, d\tau \tag{6.2}$$

$$R_{yy}(\tau) = \lim_{T\to\infty}\frac{1}{T}\int_{-T/2}^{+T/2} y(t)y(t+\tau)\, dt \tag{6.3}$$

where ω is the angular frequency, τ is a time shift and T is the total length of the data set. However, time series are finite and an estimate can be obtained using the Fourier transform ($\Im(i\omega)$) of the continuous time series $y(t)$ as shown below:

$$S_{yy}(i\omega) = \lim_{T\to\infty} E\left\{\frac{1}{2T}|\Im(i\omega)|^2\right\} \tag{6.4}$$

$$\Im(i\omega) = \int_{-\infty}^{+\infty} y(t)\exp^{(i\omega\tau)}\, dt \tag{6.5}$$

where E is the expected operator and the quantity $(1/2T)|\Im(i\omega)|^2$ is the periodogram of the time series $y(t)$. To accuartely estimate a PSD, several periodograms will be required for averaging.

A fluidized bed can be described as a dynamical system, where the response, $y(t)$, can be studied with linear system identification techniques for small inputs, $x(t)$ [107]. The dynamics of a system can be represented by the linear relationship of the Laplace transform of the input and output time series, $X(s)$ and $Y(s)$, respectively, known as the transfer function ($G(s)$) that is related to the PSD functions of the input and output:

$$G(s) = \frac{Y(s)}{X(s)} \tag{6.6}$$

$$S_{yy}(i\omega) = |G(i\omega)|^2 S_{xx}(i\omega) \tag{6.7}$$

When the input is dominated by white noise, the PSD of the input signal (S_{xx}) can be found by calculating its statistical variance (σ^2) and Eq. 6.7 can be rewritten using the variance:

$$S_{xx}(i\omega) = \sigma^2 \tag{6.8}$$

$$10 \log S_{yy}(i\omega) = 20 \log |G(i\omega)| - 20 \log \sigma \tag{6.9}$$

The transfer function can be conveniently represented by plotting $10 \log S_{yy}(i\omega)$ versus $\log \omega$; such representation is called the Bode plot. For a second-order transfer function:

$$G(i\omega) = \frac{1}{(1 - \omega^2/\omega_n^2) + i2\omega(\xi/\omega_n)} \tag{6.10}$$

where ω_n is the characteristic frequency and ξ is the damping factor with a high-frequency roll-off of -40 dB/decade. The Bode plot will help determine ω at the intersection of low and high frequency asymptotes and ξ will be noted in the trend of the plot around ω_n, as shown in Fig. 6.2. The value of ξ is greater than unity for overdamped systems, which can be identified by a gradual decrease in the PSD as the frequency increases and a noticeable resonance at ω_n. For underdamped systems, ξ is less than unity and the PSD in the Bode plot will show a sharp decrease as the frequency increases.

For a recorded data set, the PSD will be calculated as the average PSD of a series of overlapping segments. A way to compute the discrete Fourier transform for a segment of N_s data points is by using the fast Fourier transform (FFT) algorithm:

$$FFT(n) = \sum_{k=0}^{N_s - 1} y(k) e^{-i2\pi k \frac{n}{N_s}} \tag{6.11}$$

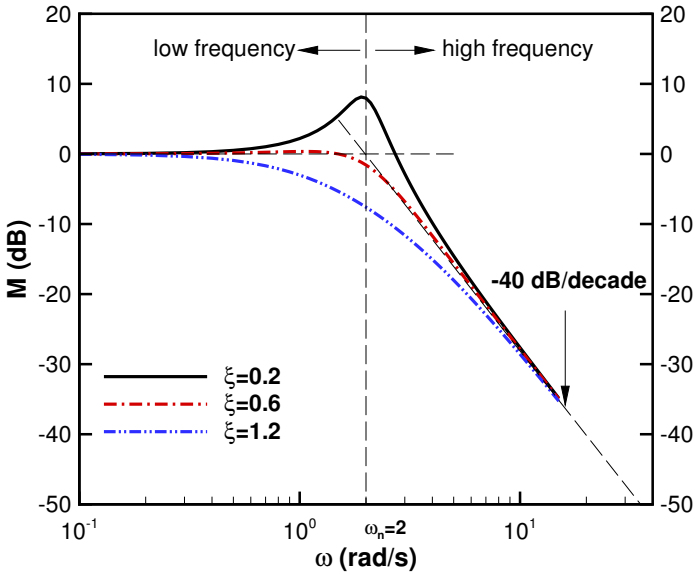

Figure 6.2: Bode plot of an ideal second-order dynamical system with a characteristic frequency $\omega_n = 2$ and damping factors $\xi = 0.2$, 0.6 and 1.2.

for $n = 0, 1, 2, ..., N_s - 1$. FFT is applicable for $N_s = 2^m$, where m is an integer greater than unity. A PSD periodogram can be calculated as follows:

$$PSD(n) = \frac{1}{2T} E\left[|FTT(n)|^2\right] = \frac{1}{2T} E\left[FTT(n) FTT^*(n)\right] \tag{6.12}$$

where $FTT^*(n)$ is the complex conjugate of the $FTT(n)$. The resulting PSD constitutes the frequency spectrum from zero to $N_s/2$. FTT can be expressed in terms of frequency (f) by:

$$f = \frac{n}{N_s} p \tag{6.13}$$

where p is the sampling frequency. Notice that a conversion from ω to f can also be obtained by:

$$f = \frac{\omega}{2\pi} \tag{6.14}$$

Similarly to Eqn. 6.9, the magnitude ($M(n)$) of a Bode plot can be calculated as follows:

$$M(n) = 10 \log PSD(n) \tag{6.15}$$

where $M(n)$ is expressed in decibels (dB).

Pressure Drop as a Second-Order Dynamical System

Pressure fluctuations in gas-solid fluidized beds can be described as a second-order mechanical vibration system or as various second-order systems working in parallel [108]. A force balance on a mechanical system consisting of a mass connected through a spring and a damper to the ground is as follows:

$$m\frac{d^2y(t)}{dt^2} + c\frac{dy(t)}{dt} + ky(t) = u(t) \tag{6.16}$$

where the first term on the left-hand side corresponds to the force due to acceleration of the mass, the second term corresponds to the force related to the damper, and the third term corresponds to the force related to the spring. The term on the right-hand side, u(t), corresponds to a forcing function that may act on the system. This equation can be expressed in terms of the natural frequency (ω_n) and damping factor (ξ):

$$\frac{d^2y(t)}{dt^2} + 2\xi\omega_n\frac{dy(t)}{dt} + \omega_n^2 y(t) = u(t) \tag{6.17}$$

Similarly, a force balance for a single particle of mass, m_i, in a fluidized bed can be written as a function of the vertical height of that particle (h_i) as shown:

$$\frac{d^2h_i(t)}{dt^2} + 2\xi\omega_n\frac{dh_i(t)}{dt} + \omega_n^2 h_i(t) = u(t) \tag{6.18}$$

The change in position of the particles are proportional to the change in void fraction, and the change in void fraction is proportional to the change in pressure drop. Therefore, Eqn. 6.18 can be expressed in terms of the pressure drop (Δp) [109]:

$$\frac{d^2\Delta p(t)}{dt^2} + 2\xi\omega_n\frac{d\Delta p(t)}{dt} + \omega_n^2\Delta p(t) = u(t) \tag{6.19}$$

The damping effects are associated with a friction or resistance to movement, which in a fluidized bed is caused by the drag force. Roy et al. [110] identified three possible sources of oscillation in fluidized beds: a natural frequency of oscillation of the bed, a surface wave that propagates pressure down, and a plenum compression wave that is present when distributor plates have a low resistance.

Hiby [111] and Verloop and Heertjes [112] proposed similar mechanisms where changes in the bed void fraction caused fluctuations in the pressure drop across the bed by lifting and returning the particles to their initial position. They found expressions for the natural frequency of the dynamical system as functions of the void fraction, the bed height, and gravity. Brue [108] modified Hiby's model by deriving the minimum fluidization velocity from the Ergun equation which included gas and particle properties and the minimum fluidization velocity. According to Sun et al. [113], due to the fact that a fluidized bed behaves as a liquid, surface waves is a phenomenon that causes pressure fluctuation in the fluidized bed and a wave frequency was defined as a function of of the gravity and the diameter of the bed.

In summary, pressure drop fluctuations in fluidized beds behave as underdamped second-order dynamical systems and represent the output signal in response to an input signal that can be associated to different phenomena. These phenomena include the local formation, motion, and coalescence of bubbles and propagating global bed oscillation and pressure waves that have their origin in the distributor, the plenum, or the bed surface. The following section describes a fluidized bed geometry for which pressure fluctuations are analyzed using σ, PSD, and Bode plots.

6.2 Problem Description

The rectangular fluidized bed geometry used in this study is based on the work of Zhang et al. [13, 14]. The lower section was modeled in the numerical simulations, as shown in Fig. 6.3. Pressure measurements at locations (1) and (4), as denoted in Fig. 6.3, were taken to record the pressure drop fluctuations for all cases; additionally, pressure measurements at locations (2) and (3) were used to compare pressure drop obtained from pressure gradients reported in the experiments [14]. Fluidizing air supplied through a 48-equally-spaced holed tuyere distributor plate is modeled as uniform flow. A single bed of sand and a binary bed of cotton stalks and sand were used in this study and their properties are shown in Table 6.1. Simulations of a binary mixture considered sand and cotton stalks to be initially mixed. The cylindrical cotton stalks were simulated as spheres using the Sauter mean diameter (Eqn. 2.11).

Table 6.1: Sand, cotton stalks, and cotton stalks-sand mixture particle properties

	Sand	**Cotton stalks**	**Cotton stalks-sand mixture**
$\bar{d_p}$ (cm)	0.045	0.655	0.048
ρ_p (g/cm^3)	2.650	0.385	2.504
$\rho_{b,M}$ (g/cm^3)	1.508	0.015	
ψ (–)	0.9	0.5†	–
m (g)	73,500	735	74,235
e (–)	0.9	0.9	0.9
U_{mf}(m/s)	0.19	–	0.20
ϵ_g^* (–)	0.423	–	0.373

† Sphericity was calculated using Eqn. 2.12

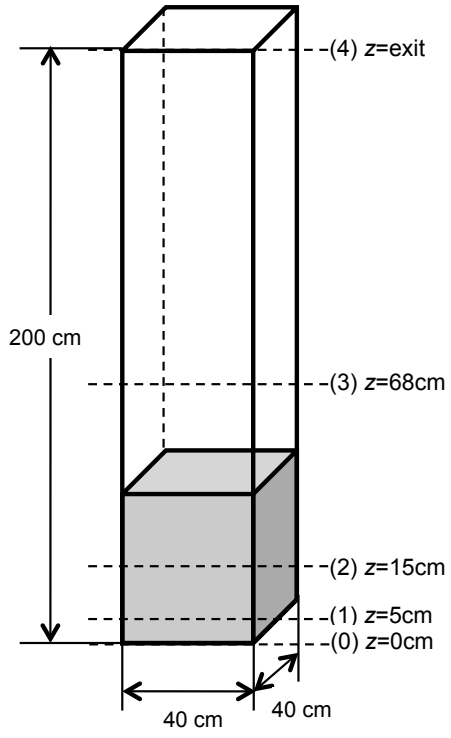

Figure 6.3: Schematic of the 3-D rectangular cylinder representing the bed of the sand-cotton stalks fluidized bed used in experiments by Zhang et al. [13, 14].

For these simulations, a uniform inlet air velocity is specified at the bottom of the domain equal to the superficial gas velocity and atmospheric pressure is specified at the exit. The no-slip condition is used to model the gas-wall interactions and a partial-slip condition for the particle-wall interactions. Table 6.1 summarizes the sand, cotton stalks, and cotton stalks-sand mixture particles properties, as described in Section 2.1.2. Inlet gas velocities ranged from 0.4 to 1.8 m/s; the lower velocity corresponds to $2.0U_{mf}$ and represents a mild bubbling bed and the higher velocity corresponds to $9.0U_{mf}$ and represents a fluidized bed in the turbulent regime. A grid resolution of 40×200 is used for the 2D domain, which was found to produce grid-insensitive results and $40 \times 200 \times 40$ for the 3D domain. Initially, Superbee discretization is used to predict pressure drop and standard deviation.

6.3 Results and Discussion

6.3.1 Pressure Drop

Initially, a bed of sand is used to confirm that the CFD modeling predicts the same pressure drop through the bed using a two-dimensional domain. The pressure drop across the sand fluidized bed versus the inlet gas velocity is shown in Fig. 6.4, comparing the experimental measurements to those predicted using MFIX. Once the bed is fluidized around $U_{mf} = 0.19$ m/s, the measured pressure drop is approximately constant at 4.5 kPa, which also corresponds to the theoretical pressure drop. The predicted pressure drop is approximately 4.3 kPa and is in very close agreement with the experimental and theoretical values and the predicted minimum fluidization velocity is 0.22 m/s.

A bed of cotton stalks-sand[1] mixture is also simulated using a two-dimensional domain. The pressure drop from locations (1–2), (2–3), (1–3), as indicated in Fig. 6.3, is compared with experimental values in Fig. 6.5. Pressure drop through the entire domain (0–4) is also included in this figure. In general, pressure drop predicted values are in agreement with experimental measurements. Two-slope linear trends after minimum fluidization for the experiments indicate partial segregation of sand and cotton for velocities up to approximately 0.4 m/s ($2U_{mf}$).

[1]For the remainder of the discussion, the word "cotton" will refer to "cotton-stalks"

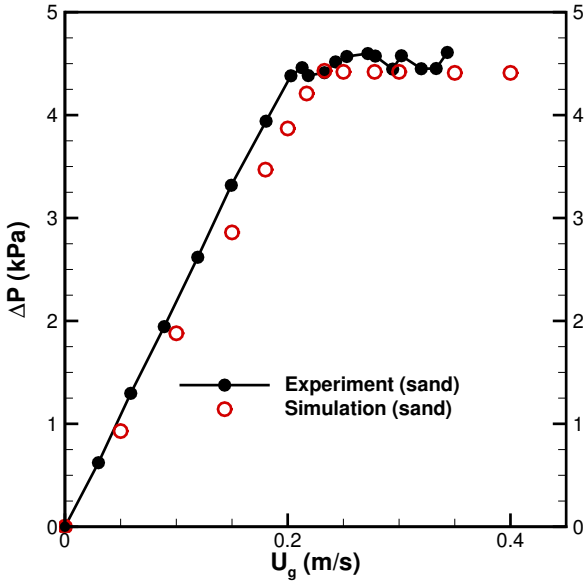

Figure 6.4: Pressure drop versus inlet gas velocity comparing experiments [13] and 2D simulations of a sand fluidized bed.

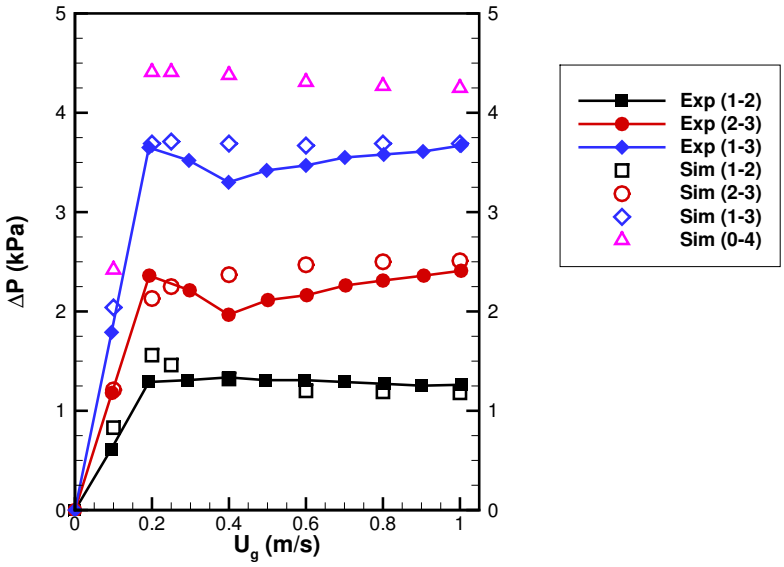

Figure 6.5: Pressure drop versus inlet gas velocity comparing experiments [14] and 2D simulations of a cotton-sand fluidized bed.

The time-average volume fractions of sand and cotton for 0.25 m/s and 0.6 m/s shown in Fig. 6.6 (a) and (b), illustrate the differences of a partially segregated and a homogeneous bed, respectively. Note that only the lower portion of the domain is shown. For inlet velocity of $1.25U_{mf}$, sand is mostly concentrated in the bottom of the bed and cotton on the top near the walls, which explains the higher pressure drop between locations (1–2). For the $3.0U_{mf}$, the material distribution is uniform and is indicative of the pressure drop being constant at this point.

Giving the low mass ratio of cotton to sand (1%), it was of interest to compare simulations of the pressure drop for the binary mixture with the sand-only data.The motivation is to continue with the study of pressure fluctuations with sand-only simulations to decrease the amount of time needed when simulations using a 3D domain will be needed. Figure 6.7 shows pressure drop for a bed of sand and cotton-sand; the average value for both of them are very close, at around 4.2 KPa.

6.3.2 Standard Deviation

The next step is to compare standard deviation of pressure drop, $\sigma_{\Delta P}$, between locations (1–4) for inlet gas velocities ranging from $1.0-9.0U_{mf}$. Standard deviation for sand and cotton-sand fluidized beds are similar and follow the same trend, as shown in Fig. 6.8. A steadily increasing trend in standard deviation shows that for velocities greater than 0.8 m/s ($4U_{mf}$) using a 2D domain is no longer appropriate. Taking into consideration that inlet velocities are high (up to $9U_{mf}$), the use a of turbulence model and a 3D domain is also considered for the fluidized bed simulations.

Having confidence in the similarity of results between a fluidized bed of cotton-sand and sand, the following study will be performed using sand only. Using a 3D domain to model the bed at velocities greater than $4U_{mf}$ shows a noticeable improvement in the prediction of standard deviation of pressure drop; however, the standard deviation when velocities are greater than the peak of $6U_{mf}$ (1.2 m/s) remains constant, as shown in Fig. 6.9 in red triangles. The flow in this region is considered to be turbulent and therefore two turbulence models, κ-ϵ

and Ahmadi, are tested and shown in Fig. 6.9 as squares and diamonds, respectively.

Including turbulence in the modeling underpredicts the standard deviation for the peak at 1.2 m/s and does not decrease for higher velocities as expected. Furthermore, using the Superbee discretization with turbulence models requires constant tuning of the maximum velocity factor and under-relaxation factor for the gas pressure equation. Even with these these adjustments the simulations at higher velocities are unstable and have problems converging beyond 10 s.

The three cases using no turbulence model and with turbulence models are repeated using MUSCL discretization and the results are shown in Fig. 6.10. Simulations using MUSCL discretization and the Ahmadi turbulence model are able to capture the trends reported in the experiments. Standard deviation shows a peak at $6U_{mf}$, which according to numerous experimental works, correlates to the transition from a bubbling to turbulent fluidization regime, known as the slugging regime. The peak is captured with the CFD simulations for the sand-only fluidized bed. Standard deviation of a cotton-sand bed, however, shows a fall in the value. The turbulence model is only necessary for velocities greater than $6U_{mf}$, when the regime transitions to turbulent flow and the standard deviation starts decreasing.

The sand and cotton-sand fluidized beds are shown in Fig. 6.11 with a best curve fit as a second-order polynomial, and both 2D and 3D simulations using MUSCL. In summary, the MUSCL discretization works best for all cases. Furthermore, it has been shown that 2D simulations are valid for $U_g \leq 4U_{mf}$, which is the bubbling fluidization regime. For $U_g > 4U_{mf}$, 3D simulations are necessary and once the flow begins the transition from slugging to turbulent flow ($U_g > 6U_{mf}$), the Ahmadi turbulence model gives the best predictions.

Some additional cases were considered around $9U_{mf}$ to test the model capability to identify the transition to a fast fluidization regime as explained in Section 6.1.1. Both cotton-sand and sand-only fluidized beds were simulated in three dimensions and the values for $\sigma_{\Delta P}$ are shown in Fig. 6.11. Standard deviation of pressure fluctuation beyond 1.8 m/s slightly increases and remains relatively constant showing agreement with the reported general trend presented in Fig. 6.1. The fast fluidization regime is out of the scope of this study, however it is encouraging

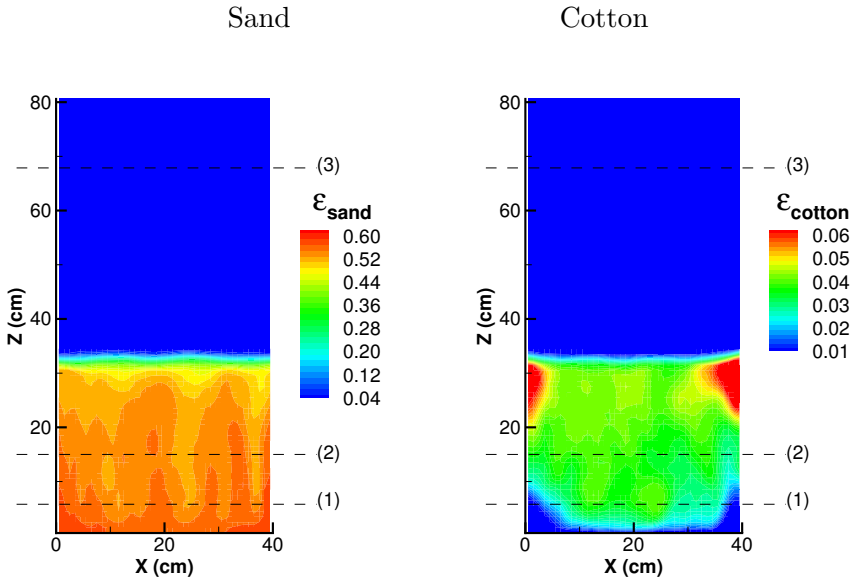

(a) $U_g = 1.25U_{mf}$

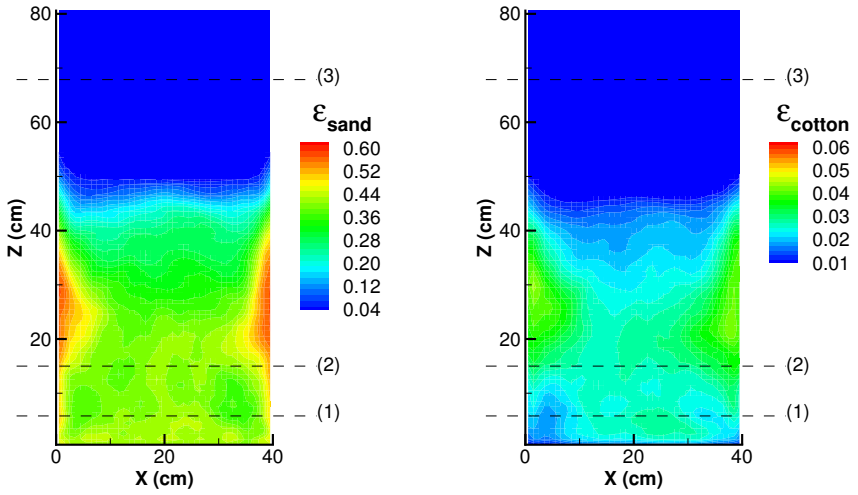

(b) $U_g = 3.0U_{mf}$

Figure 6.6: Time-average volume fraction of sand (left) and cotton (right) as a binary mixture with inlet velocity of (a) U_g=0.25 m/s and (b) U_g=0.6 m/s.

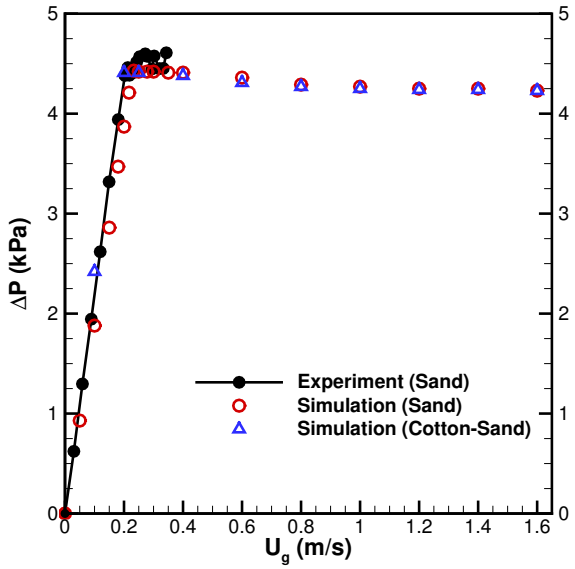

Figure 6.7: Pressure drop versus inlet gas velocity comparing experiments [13] and 2D simulations of sand and cotton-sand fluidized beds.

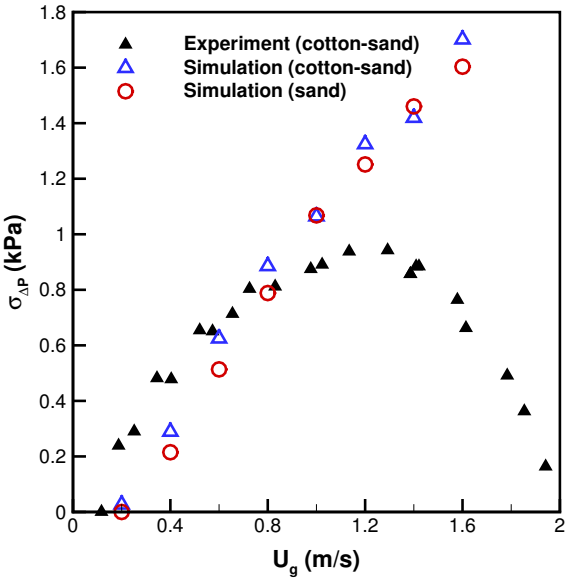

Figure 6.8: Standard deviation of pressure drop comparing experiments [14] and 2D simulations of sand and cotton-sand fluidized bed versus inlet gas velocity

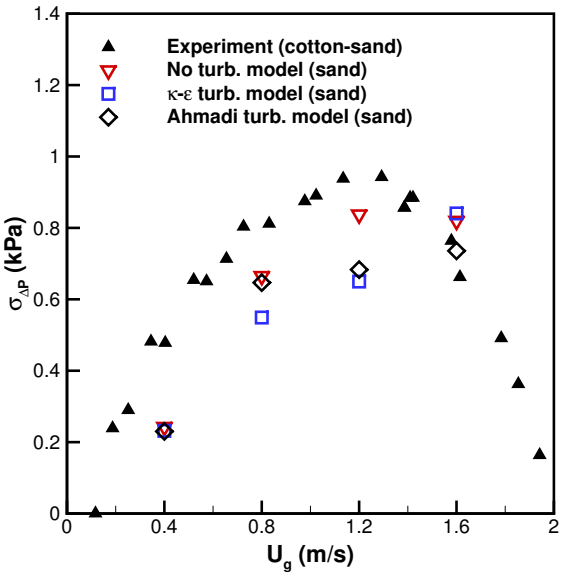

Figure 6.9: Standard deviation of pressure drop comparing 3D simulations of sand fluidized beds using turbulence models and Superbee discretization.

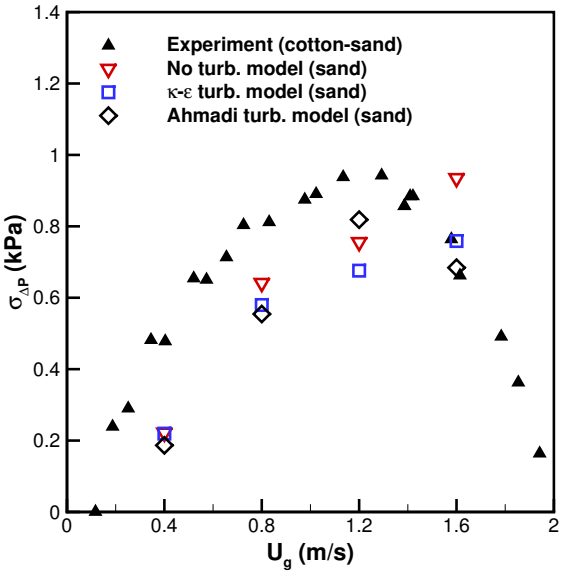

Figure 6.10: Standard deviation of pressure drop comparing 3D simulations of sand fluidized beds using turbulence models and MUSCL discretization.

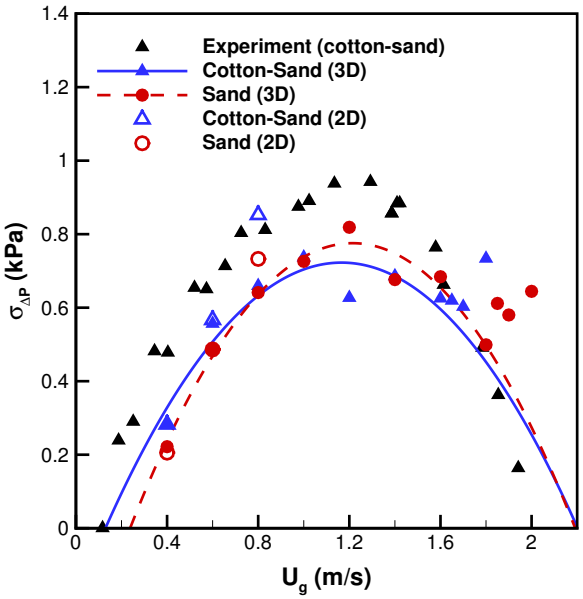

Figure 6.11: Best fit of standard deviation of pressure drop for sand and cotton-sand fluidized beds using MUSCL discretization.

that the numerical model can predict a fast fluidization regime.

It is clear from the comparison shown in Fig. 6.11 that the sand-only fluidized bed can predict standard deviations of cotton-sand bed for a mass ratio of 1%. The 3D simulations of fluidized beds using sand closely resemble predictions of the hydrodynamic behavior of cotton-sand beds, as shown in the time-average contour plots of void fractions shown in Fig. 6.12. The slices correspond to a central vertical plane and only 80 cm is shown because no fluidization occurs beyond that height. Each set of subfigures (a), (b), and (c) corresponds to the bubbling, slugging, and turbulent fluidization regimes represented by $U_g = 0.8$, 1.2, and 1.6 m/s, respectively. Gas-solids distributions and bed heights for sand and cotton-sand are in very close agreement. Figure 6.12 (d) represents the time-average void fraction horizontally-averaged across the rectangular cross section of the domain (x-y plane), and is useful for identifying bed expansion at an approximately constant height. It can be seen that for both sand and cotton-sand, the bed expansion for the bubbling fluidization regime is around 40 cm. The

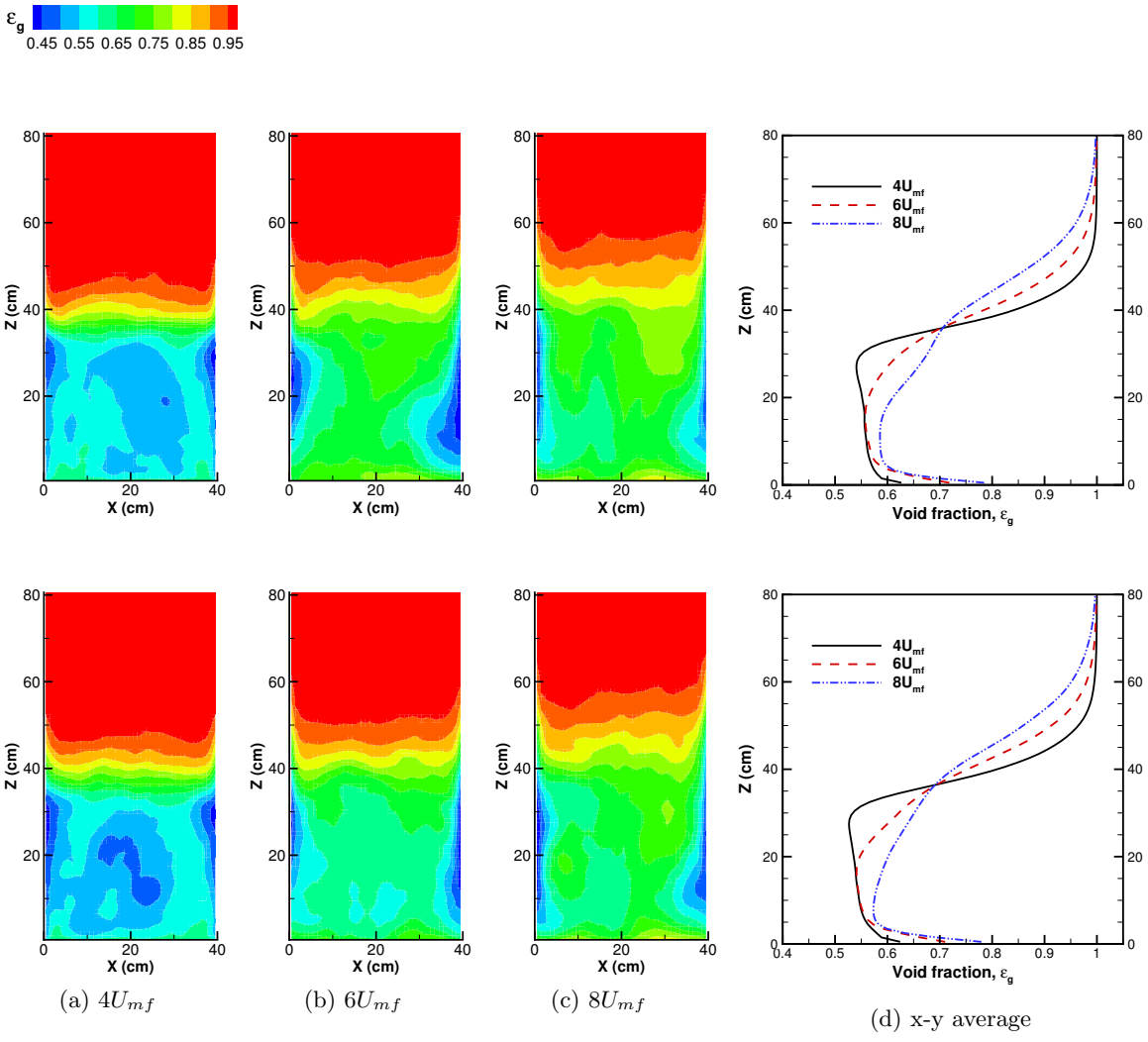

(a) $4U_{mf}$ (b) $6U_{mf}$ (c) $8U_{mf}$ (d) x-y average

Figure 6.12: Time-average void fraction of sand (top) and cotton-sand (bottom) fluidized beds using a 3D domain with inlet velocity of (a) U_g=0.8 m/s, (b) U_g=1.2 m/s, (c) U_g=1.6 m/s, and (d) x-y average void fraction for the three cases.

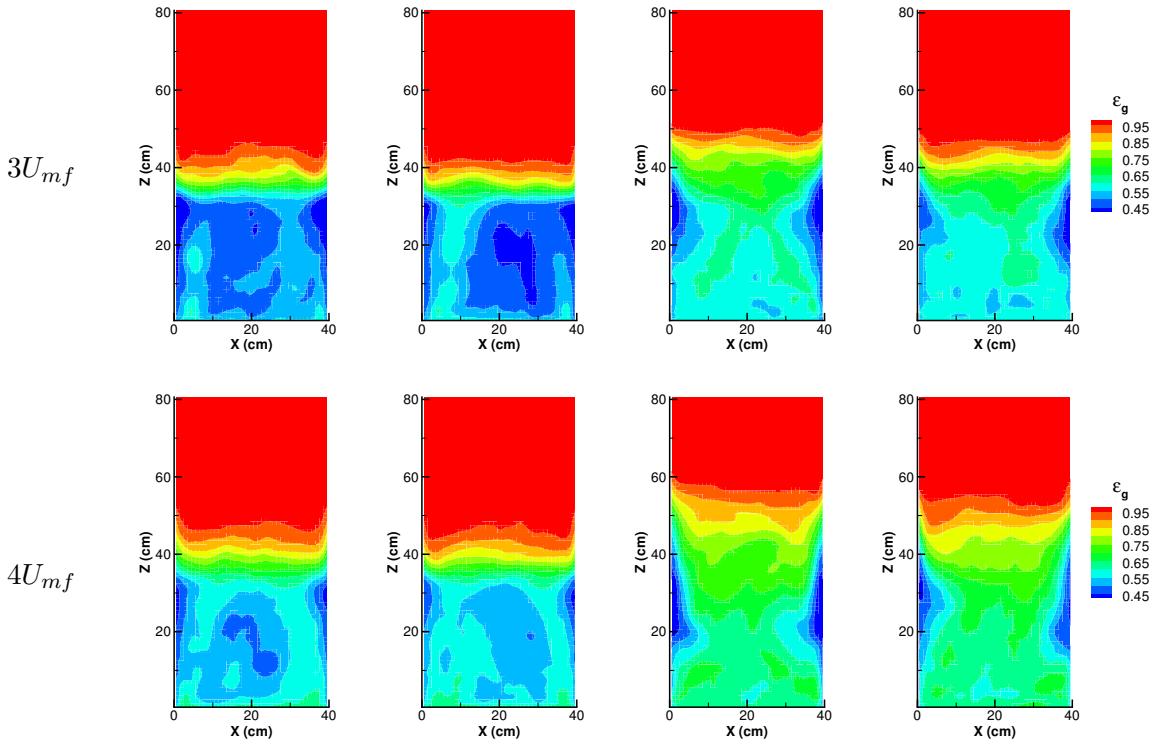

(a) Cotton-Sand (3D) (b) Sand (3D) (c) Cotton-Sand (2D) (d) Sand (2D)

Figure 6.13: Time-average void fraction with inlet velocities of U_g=0.6 m/s (top) and U_g=0.8 m/s (bottom) for fluidized beds (a) Cotton-Sand (3D), (b) Sand (3D), (c) Cotton-Sand (2D), and (d) Sand (2D).

bed surface is not well defined for slugging and turbulent fluidization regimes by showing an inclined trend as the void fraction increases.

Also of interest is the comparison of the void fraction using 2D and 3D domains shown in Fig. 6.13. Although standard deviation using a 2D domain for inlet velocities of $3U_{mf}$ and $4U_{mf}$ are in good agreement with experimental data, void fraction plots show differences between the 2D and 3D domains. It has been reported by Xie et al. [74] and Deza et al. [114] that using a 2D domain with inlet velocities, $2U_{mf}$ and $3U_{mf}$, respectively, overpredicts bed expansion. The over-prediction was due to energy diverting to non-axial momentum terms for increasing inlet velocities [115].

In order to further identify salient features of each of the fluidization regimes, instantaneous void fractions contours at five time intervals with Δt = 0.05 s are shown in Fig. 6.14. The

slices correspond to a central vertical plane and only 80 cm.

The bubbling fluidized bed (top row) shows small bubbles coalescing as they rise. A well defined bed surface can also be visualized, consistent with the time-average void fraction horizontally-averaged in Fig. 6.12 (d). Void fractions for a slugging regime (middle row), show a coalesced large bubble rising to the bed surface. The bed surface is not well defined due to the slugging bubble rising periodically and exploding at the surface. The turbulent fluidization regime (bottom row) shows irregular voids and changing bed surface as gas is released and this fact is also evident in Fig. 6.12 (d).

6.3.3 Power Spectral Density Analysis

PSD analysis has been performed in a sand and cotton-sand fluidized beds for pressure drop fluctuations between locations (1-4) to be consistent with the previous analysis using standard deviation. Before analyzing results using PSD, some parameters such as data sampling frequency, number of overlapping segments for signal averaging, and time range need to be determined for the available data sets. These parameters will be tested according to recommended values. Brue and Brown [15] recommended low frequency sampling rates with long sampling intervals. They noted that a sampling frequency of 20–100 Hz did not show any difference in the high frequency of the PSD. To find an accurate approximation of the PSD, data should be partitioned into a number of overlapping segments that will be transformed into periodograms. The number of segments will depend on the amount of data collected. Brue and Brown [15] recommended collecting at least 1200 seconds of data to capture phenomena occurring at low frequencies.

For this parametric study, a 2D case of the sand fluidized bed at $2U_{mf}$ (0.4 m/s) was simulated for 1205 s and the first 5 s were not considered in the analysis to remove initial transients. Data was recorded at 25, 50, and 100 Hz frequencies. In the comparisons shown in Fig. 6.15, it can be seen that PSD values decrease with decreasing sampling frequency, which can be attributed to the that fact that pressure peaks are not being captured using 25 Hz compared to using 100 Hz when recording pressure information. At low frequencies, $f < 2$, all

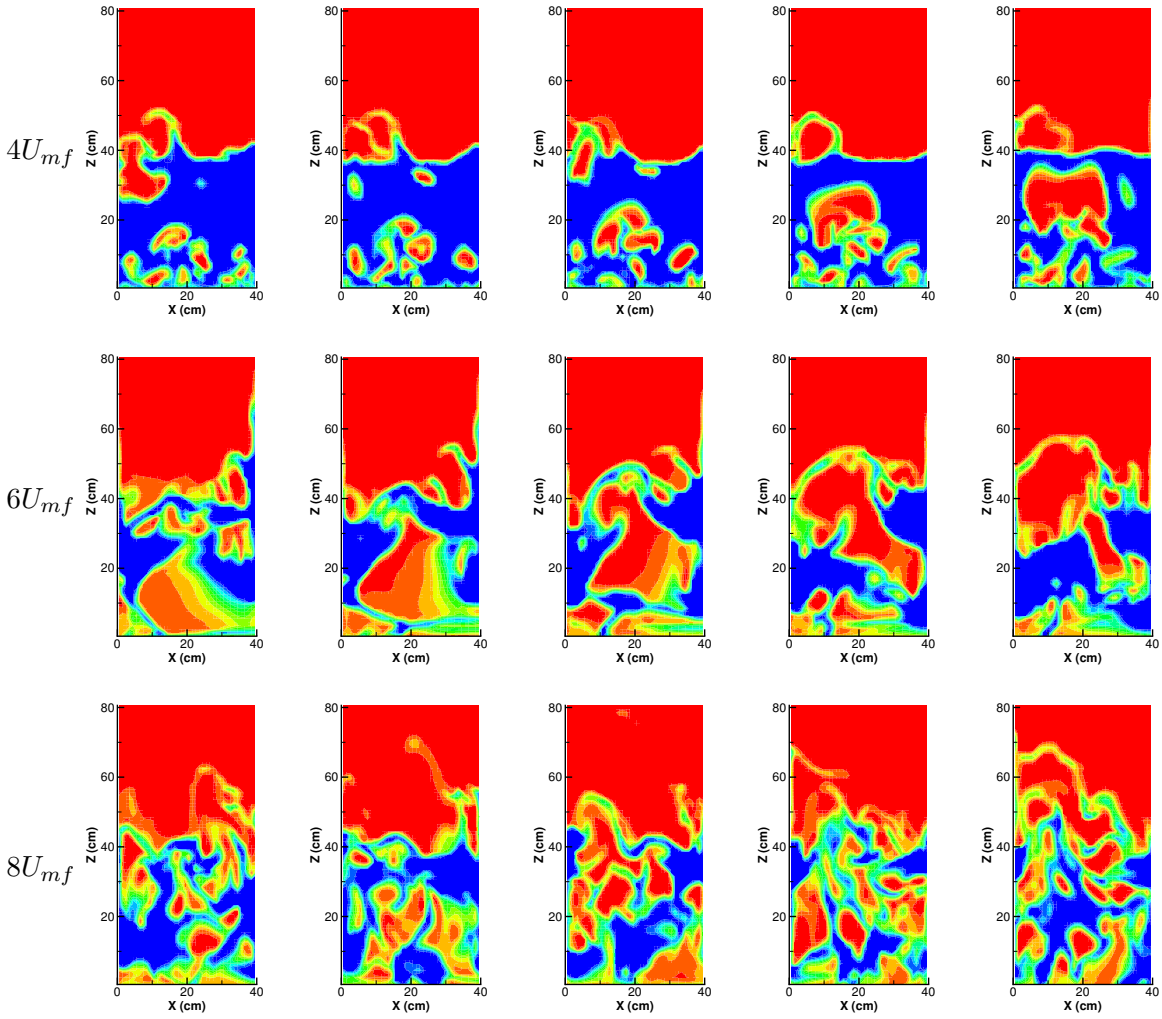

(a) t_1 (b) t_2 (c) t_3 (d) t_4 (e) t_5

Figure 6.14: Instantaneous void fraction of a sand fluidized bed at an inlet velocity $U_g = 0.8$ m/s (top), $U_g = 1.2$ m/s (middle), and $U_g = 1.6$ m/s (bottom) at five different times.

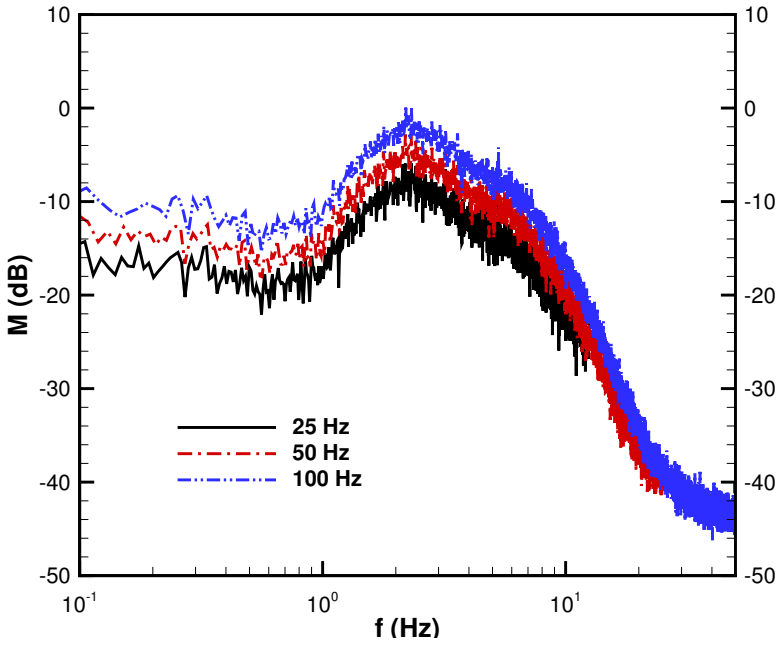

Figure 6.15: Bode plots representing pressure fluctuation of a sand fluidized bed at 0.4 m/s for 1200 seconds using data sampling of 25, 50, and 100 Hz.

the cases exhibit a similar trend, but differ in magnitude. At high frequencies, no important features are being captured besides the characteristic -40dB/decade roll-off of the dynamic system. Taking these facts and amount of time of data collected into consideration, a sampling frequency of 50 Hz will be used for the remaining analyses.

To understand the effect of the number of overlapping segments in the spectrum, four different cases using 10, 15, 20, and 30 segments were chosen to calculate the FFT used in PSD with 1200 s of simulation at 50 Hz of recording data. Their respective Bode plots for pressure drop fluctuation can be seen in Fig. 6.16 (a-d), where it is observed that as the number of overlapping segments are increased, the spectrum is less noisy because more periodograms are being considered to estimate the PSD. However, for higher number of segments, most of the featured peaks cannot be clearly seen. To single out the effect on the amount of time considered for the simulations, with 50 Hz of sampling data and using 15 overlapping segments, four simulation times are considered: 150, 300, 600, and 1200 seconds. Figure 6.17(a-d) presents

Table 6.2: Computational time for simulations, CPU (days)

	2D (40×200)		3D ($40 \times 40 \times 200$)	
	sand	cotton-sand	sand	cotton-sand
Number of processors	2	2	16	16
$U_g = 0.8$ m/s	4	22	102	45†
$U_g = 1.2$ m/s	–	–	92	49†
$U_g = 1.6$ m/s	–	–	101	45†

† *for 20 seconds of simulation*

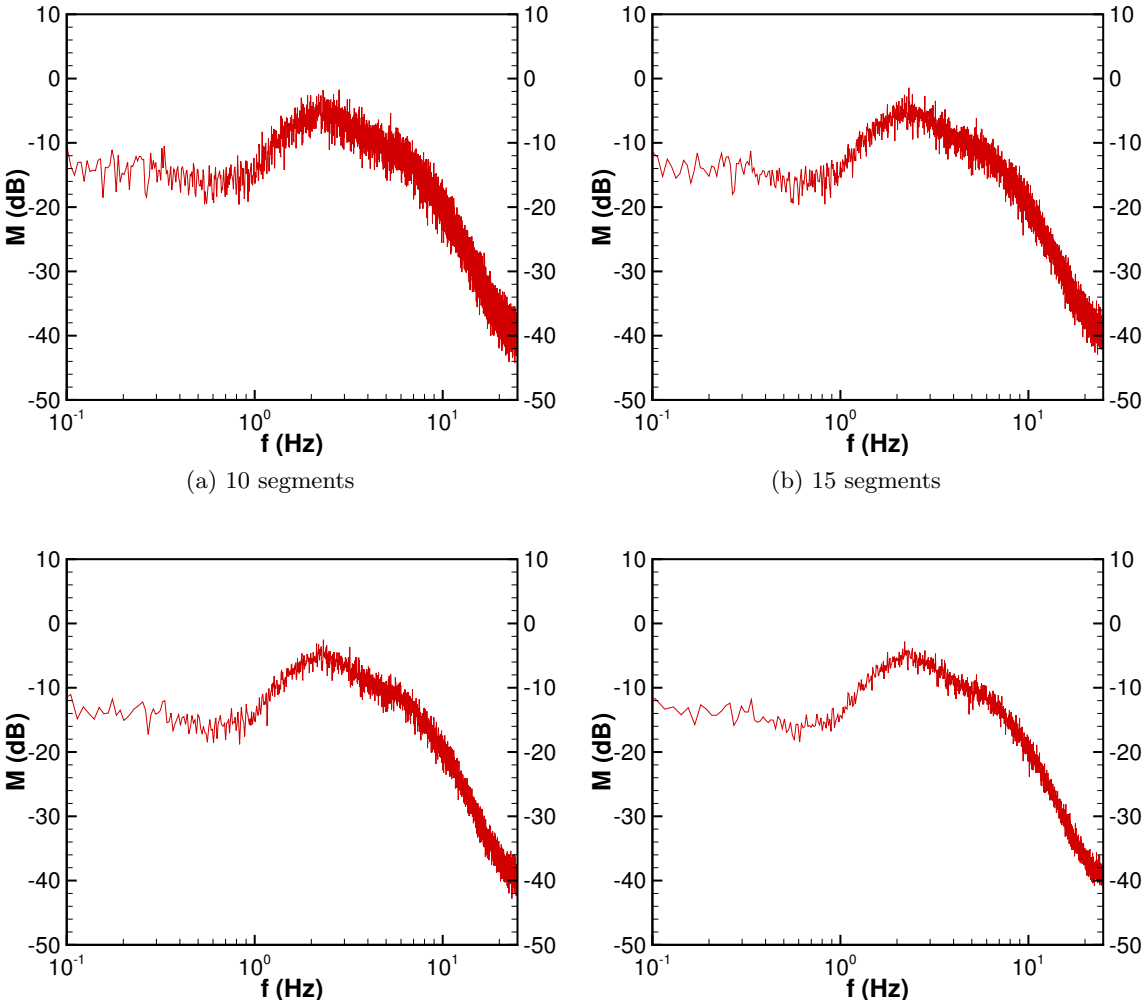

(a) 10 segments

(b) 15 segments

(c) 20 segments

(d) 30 segments

Figure 6.16: Bode plots for pressure drop of a sand fluidized bed at 0.4 m/s for 1200 seconds using (a) 10, (b) 15, (a) 20, and (a) 30 overlaping segments.

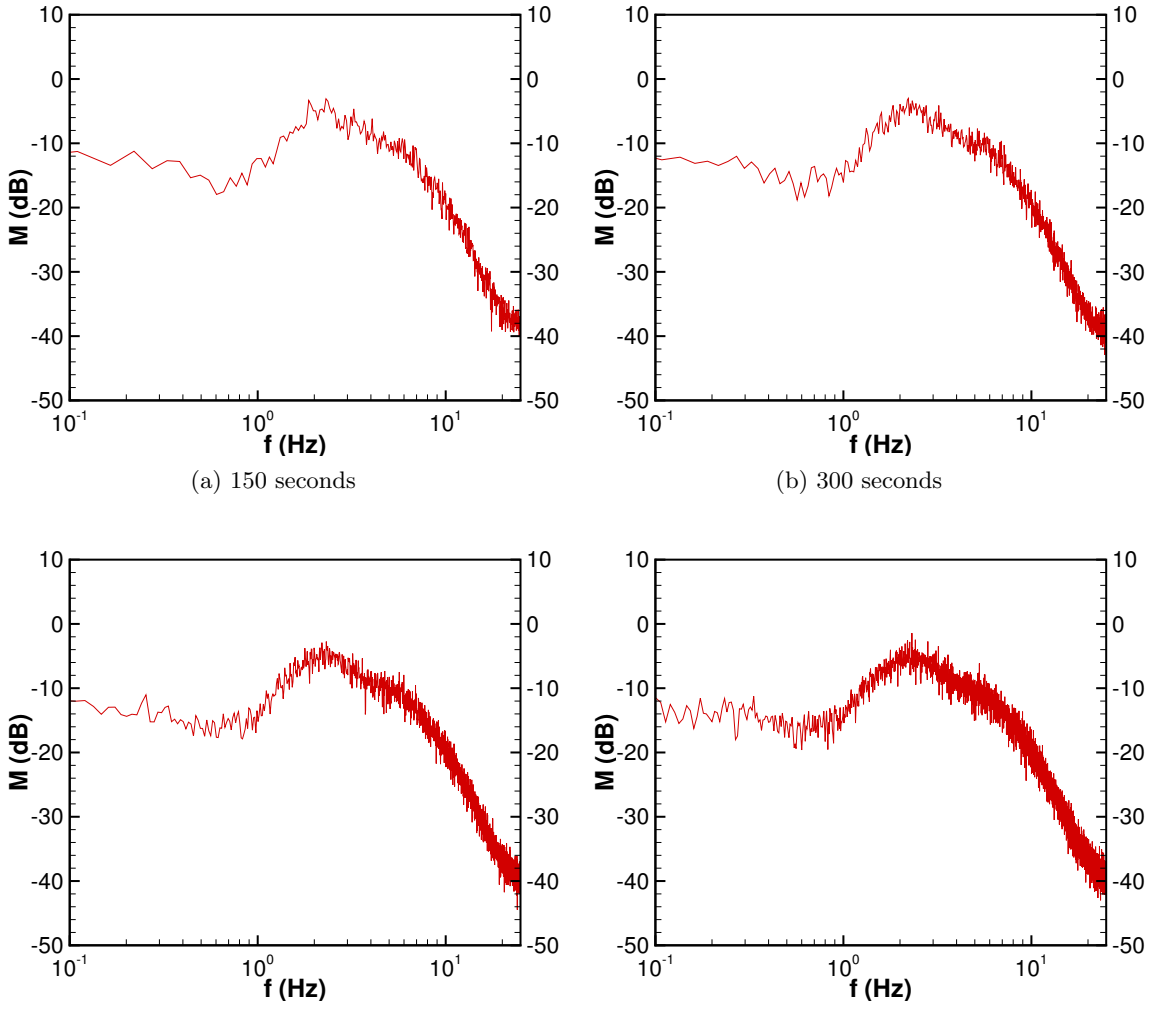

(a) 150 seconds

(b) 300 seconds

(c) 600 seconds

(d) 1200 seconds

Figure 6.17: Bode plots for pressure drop of a sand fluidized bed at 0.4 m/s for (a) 150, (b) 300, (c) 600, and (d) 1200 seconds using 15 overlaping segments.

the Bode plots for these cases and shows how decreasing the amount of time decreases the amount of data per segment and the features of the PSD become less obvious and difficult to identify.

Continuing with the analysis performed for standard deviation in Section 6.3.2, the same three cases are used to study PSD. The cases represent bubbling, slugging, and turbulent fluidization regimes at inlet velocities U_g = 0.8, 1.2, and 1.6 m/s, and correspond to 4, 6, and $8U_{mf}$, respectively. Simulations using the 3D domain and sand as the bed material are analyzed with data collected for 195 seconds. Table 6.2 shows the number of processors and the CPU time in days to simulate 200 seconds of the cases analyzed. The simulations were performed on an Apple G5 with 64 bit, 2.3 GHz IBM (PPC970) dual processors. CPU time for 20 seconds of cotton-sand bed simulations have been included in the table to show how computationally expensive these simulations can be. Bases on previous analysis for overlapping segments and time, as little as 150 s and 10 overlapping segments will capture features present in the PSD and Bode plots. Two more cases at 0.8 m/s are considered to further establish the validity of using a 2D domain and sand instead of the cotton-sand mixtures for low mass ratios up to $4U_{mf}$.

Pressure data will be presented in Figs. 6.18 – 6.22 using three analysis techniques where distinct features will be identified for each fluidization regime. In part (a) of each figure, pressure drop for a 25 s time period is shown to demonstrate how the pressure drop fluctuates with time. Pressure drop for all the cases have been shifted to zero to help quantify the fluctuation around the mean value by:

$$\Delta p^* = \Delta p - \bar{p}$$

For part (b) of Figs. 6.18 - 6.22, the PSD is shown for data collected over 195 s and the Bode plots are shown in part (c). The pressure drop have a minimum and maximum of approximately +/- 1 kPa for the bubbling fluidization regime (Fig. 6.18 (a)), but for other fluidization regimes, (Figs. 6.19 (a), 6.20 (a)) the pressure drop fluctuations are more pronounced.

PSD has commonly been used to find the dominant frequency in the dynamic system; however their Bode plot representation offer an advantage in the identification of additional

frequencies and in determining the order of the dynamic system. As we compare Bode plots for each regime, it is evident that the dynamic system for all three cases is of second order with a roll-off of -40 dB/decade for high frequencies. On the other hand, there are noticeable differences in the peak intensity and distribution among all regimes, which is also evident in the PSD.

PSD and Bode plots for the bubbling regime (Fig. 6.18(b) and (c)) show a series of peaks, which can be described as a broad peak between 2 and 4 Hz, with a maximum at f_B =2.6 Hz, where the subscript B denotes the bubbling fluidization regime. A similar trend for the PSD was obtained from the experiments of Johnson et al. [56] for a fluidized bed in the bubbling regime. Brue [108] showed the same trend for PSD as well as Bode plots in many of his bubbling fluidized bed cases.

The slugging fluidization regime PSD and Bode plots (Fig. 6.19(b) and (c)) show two broad peaks at lower frequencies over a range of 1.5 to 5 Hz, with a peak $f_{S,1} = 2$ Hz and another peak at $f_{S,2} = 3.5$ Hz, where the subscript S denotes the slugging fluidization regime. However, the magnitudes of these peaks are lower than the peak in the bubbling regime (Fig. 6.18). These distinctive broad peaks correspond to previous observations of two peaks at low frequencies, which were identified as characteristics of the slugging regime spectrum by van der Schaaf et al [116].

For fluidized beds in the turbulent fluidization regime, one peak at approximately $f_{T,1} = 2$ Hz and a broader peak at $f_{T,2} = 4.5$ Hz are identified in the PSD and Bode plot (Fig. 6.20(b) and (c)). Brue [108] found that with increasing inlet velocity, the frequencies corresponding to the higher peaks will decrease. For these cases, the peak at lower frequency has a greater magnitude. The existence of two peaks in the spectrum of a turbulent fluidized bed have also been reported by Brue and Brown [15].

It is desirable to know if a 2D domain can be used instead of a 3D domain for PSD analysis in the bubbling fluidization regime ($U_g < 4U_{mf}$). It will also be useful to see how the PSD and Bode plots compare with simulations of a binary mixture of cotton and sand. Both approximations will greatly reduce the computational time-intensive simulations. Comparisons

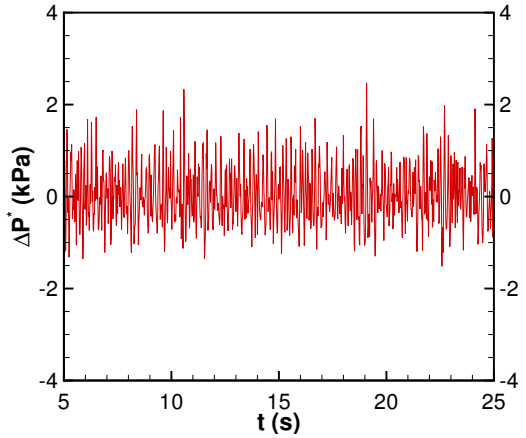

(a) Pressure Drop

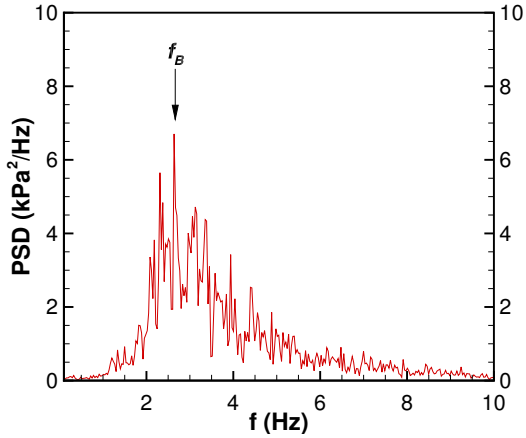

(b) PSD

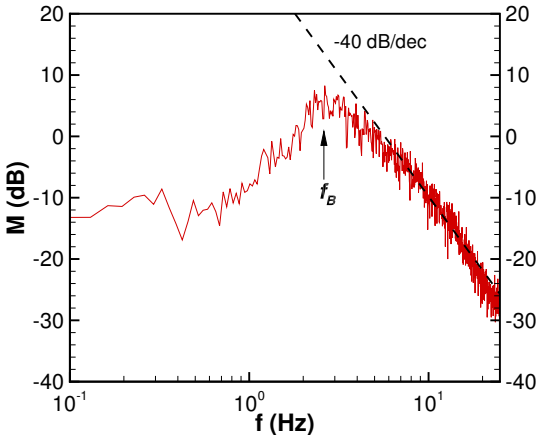

(c) Bode Plot

Figure 6.18: Pressure drop fluctuation (a) with time, (b) as a PSD analysis, and (c) as a Bode plot for a sand fluidized bed with inlet velocity of 0.8 m/s and using a 3D domain.

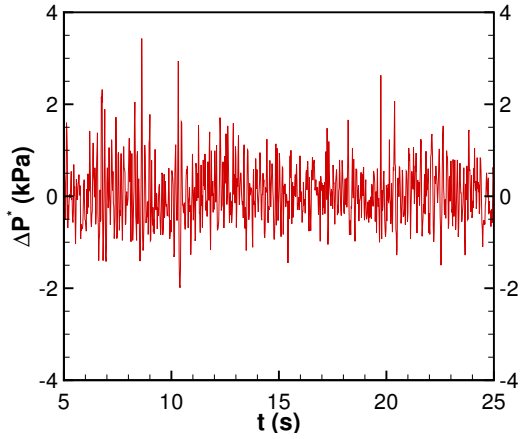

(a) Pressure Drop

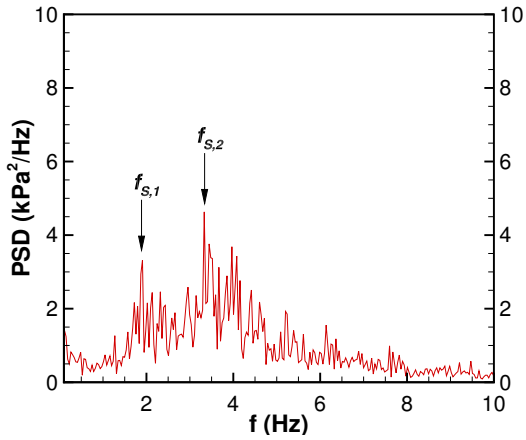

(b) PSD

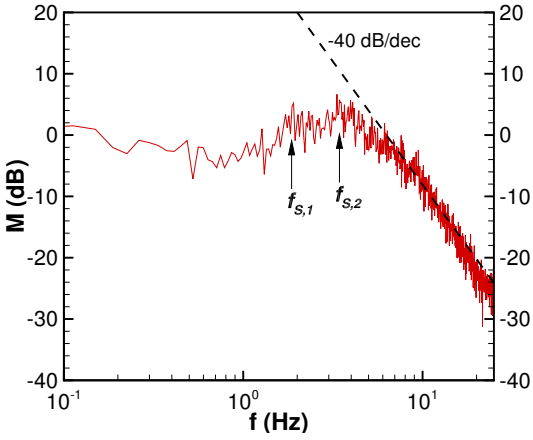

(c) Bode Plot

Figure 6.19: Pressure drop fluctuation (a) with time, (b) as a PSD analysis, and (c) as a Bode plot for a sand fluidized bed with inlet velocity of 1.2 m/s and using a 3D domain.

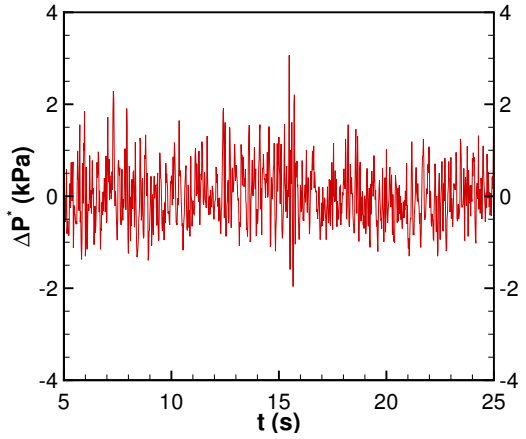

(a) Pressure Drop

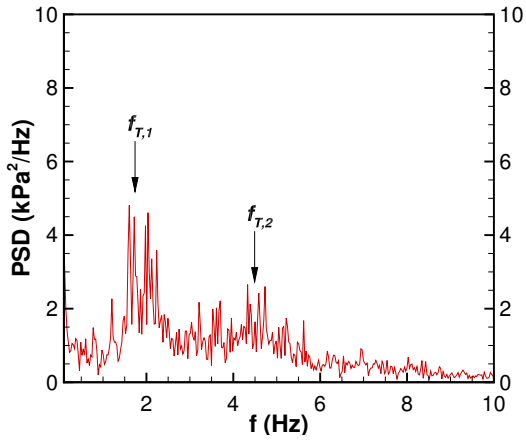

(b) PSD

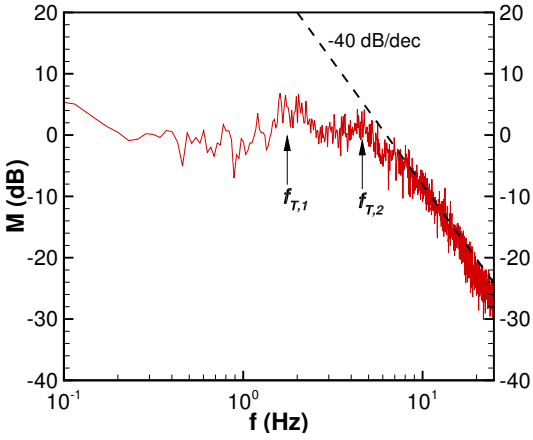

(c) Bode Plot

Figure 6.20: Pressure drop fluctuation (a) with time, (b) as a PSD analysis, and (c) as a Bode plot for a sand fluidized bed with inlet velocity of 1.6 m/s and using a 3D domain.

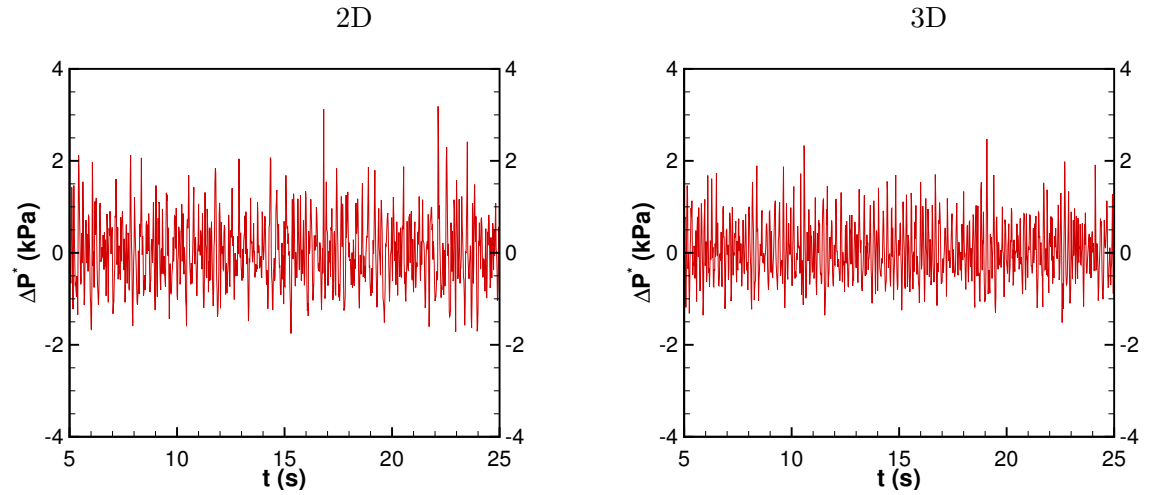

(a) Pressure Drop

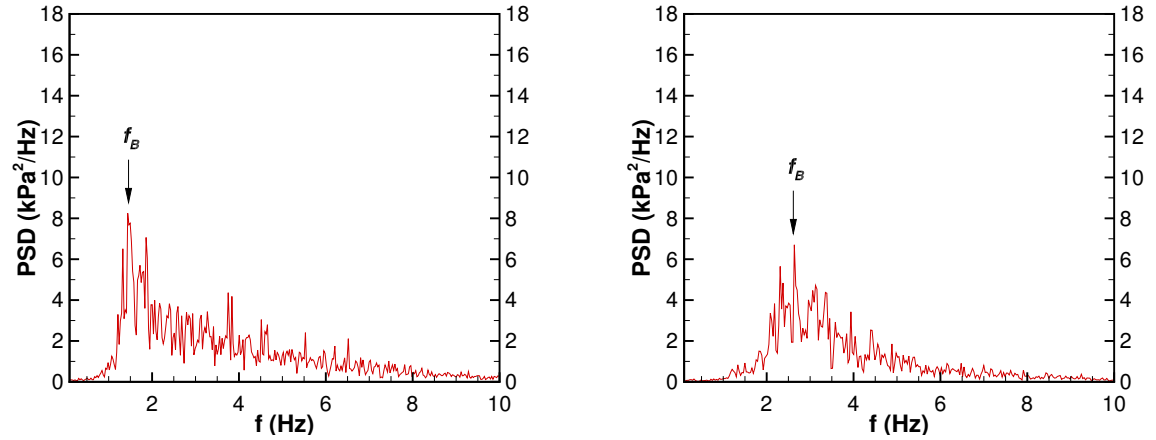

(b) PSD

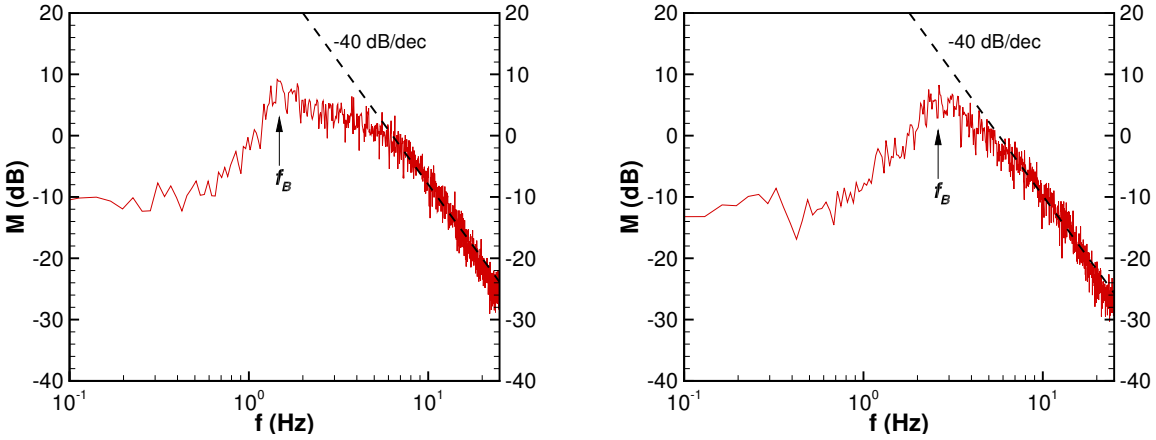

(c) Bode Plot

Figure 6.21: Pressure drop fluctuation (a) with time, (b) as PSD analysis, and (c) as a Bode plot for sand fluidized beds with inlet velocity of 0.8 m/s and using a 2D (left) and a 3D (right) domain.

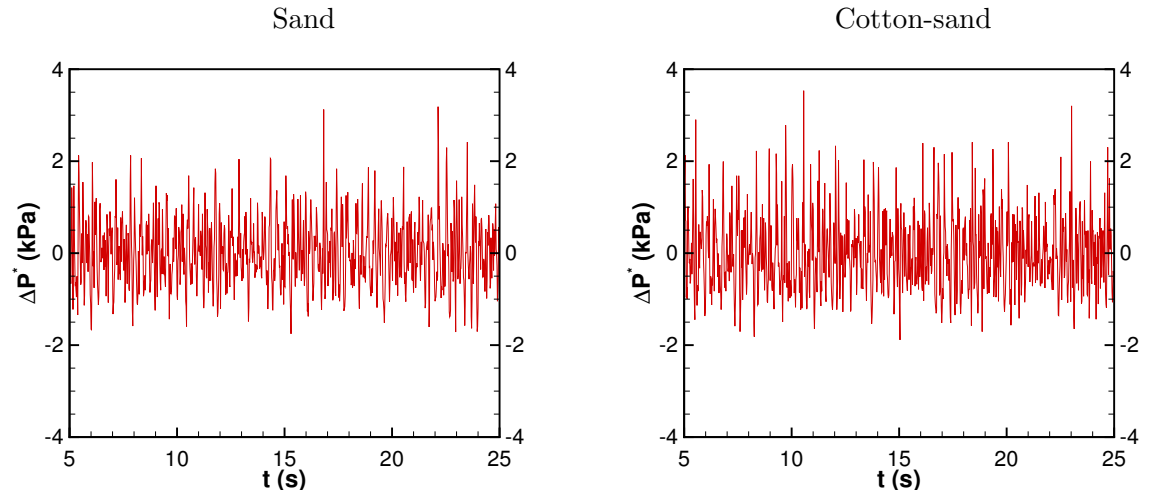

(a) Pressure Drop

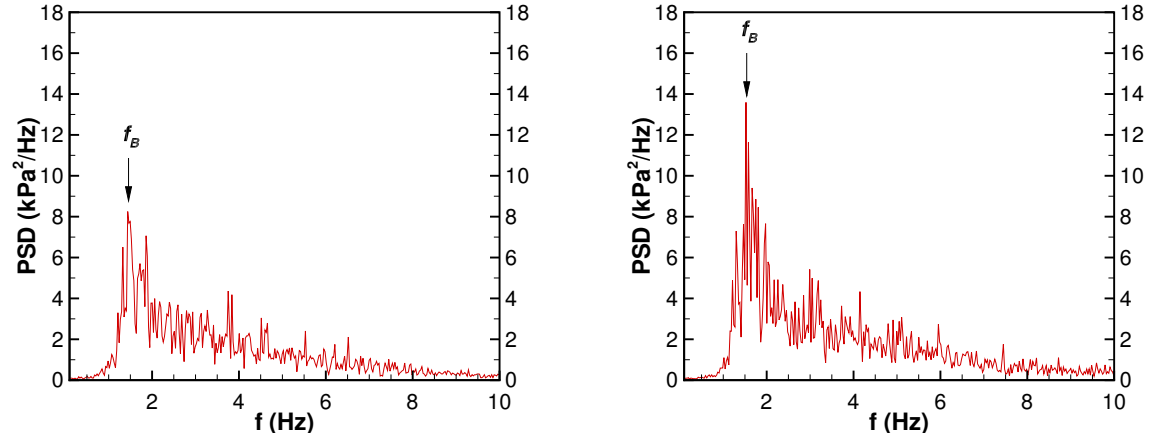

(b) PSD

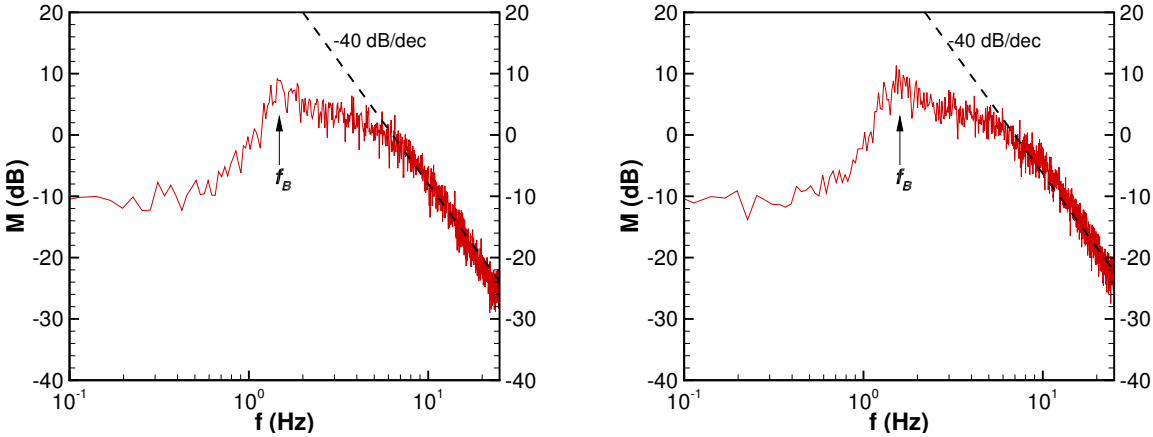

(c) Bode Plot

Figure 6.22: Pressure Drop Fluctuation for sand (left) and cotton-sand (right) fluidized beds with inlet velocity of 0.8 m/s and using a 2D domain (a) with time, (b) as a PSD analysis, and (c) as a Bode Plot.

of bed material will be performed with the 2D domain since the use of a 3D domain and binary mixture will take too long to simulate (see Table 6.2). To determined if these simplifications are appropriate, three cases are compared in Figs. 6.21 and 6.22.

When comparing 2D versus 3D domains, it can be seen that the pressure fluctuations for the 2D simulations are greater and not as uniform as for the 3D simulations (Fig. 6.21(a)), which is consistent with a higher standard deviation of pressure drop for the 2D than for the 3D domain (Fig. 6.11). The PSD for both 2D and 3D simulations contain one peak at low frequencies; however, for the 2D case the peak at $f_B = 1.4$ Hz is shifted to the left compared with the 3D cases ($f_B = 2.6$ Hz) and then gradually decreases as the frequency increases. The PSD of the peaks for the 2D and 3D cases are of similar value, about 8 and 7 kPa^2/Hz, respectively (Fig. 6.21(b)). The gradual decrease of the peak is observed in the Bode plots as a damped system after the peak (Fig. 6.21(c)).

The mentioned features of the simulations of a sand-only fluidized bed at $4U_{mf}$ suggest that using a 2D may underpredict the characteristic peak for a bubbling fluidization regime. However, the 2D domain should be sufficient to simulate a fluidized bed of cotton-sand of $4U_{mf}$ to compare its features to those present in a sand-only fluidized bed. General trends of pressure drop fluctuation, PSD, and Bode plots are very similar as shown in Fig. 6.22. It can be seen that the cotton-sand fluidized bed presents a peak at approximately the same location, $f_B = 1.5$ Hz, but of higher magnitude than for a sand-only fluidized bed. Although PSD and M are attenuated when using the sand-only fluidized bed, the model is still able to predict general spectrum features of the cotton-sand fluidized for low mass ratios.

6.4 Conclusions

A computational model using MFIX has been validated for a cotton-sand fluidized bed operating at inlet velocities ranging from 1.0–9.0U_{mf} with experimental results of Zhang et al. [13, 14]. Fluidization regimes for these cases fall in the bubbling, slugging and turbulent regimes. The hydrodynamic features of fluidized beds in this study have been mainly analyzed by means of pressure fluctuation analysis. Plots of variations of pressure with time, standard

deviation of pressure drop, and power spectrum with frequency have been used to characterize fluidized beds at different inlet velocities for a single bed material and a binary mixture.

Initially pressure drop for sand and cotton-sand beds were tested using a 2D domain model and Superbee discretization. Predicted pressure drop of 4.3 kPa and minimum fluidization velocity of 0.22 m/s for a sand fluidized bed are in very close agreement with those reported in the experiment (4.5 kPa and 0.19 m/s, respectively). Predicted pressure drop and minimum fluidization velocity of a cotton-sand fluidized bed are 4.3 kPa and 0.18 m/s, respectively, and also very close to those reported for sand-only fluidized beds. Results from experiments of cotton-sand bed show pressure drop between three different heights: 5, 15, and 68 cm. Predicted pressure drop between these locations have good agreement with the experimental data, however simulations show some segregation at incipient fluidization velocities.

Standard deviation was overpredicted for inlet velocities greater than $4U_{mf}$ when using a 2D domain, therefore modeling with a 3D domain, as well of the the use of a turbulence model for high velocities was studied. Two turbulence models, κ-ϵ and Ahmadi, and two discretization methods, Superbee and MUSCL, were tested. After comparing all the different models and evaluating solid-gas distributions and bed expansion in their corresponding contour plots, it was determined that the fluidized bed can be appropriately modeled by using MUSCL discretization and the Ahmadi turbulence model for velocities equal to and greater than $6U_{mf}$, which corresponds to the peak of standard deviation of pressure drop. Standard deviation for sand and cotton-sand beds yield very similar results and using a 2D domain for velocities up to $4U_{mf}$ are close to experimental results.

Three cases at 4, 6, and $8U_{mf}$ were chosen to represent bubbling, slugging, and turbulent regimes. Three-dimensional sand fluidized beds at these inlet velocities were used to complete 200 s of simulation. Additionally, 2D cases of sand and cotton-sand for $4U_{mf}$ were simulated to test if using a 2D domain and a bed of only sand could be used to represent the cotton-sand mixture at low mass ratios. Both PSD and Bode plots were compared for all the cases studied. Fluidized beds for all the regimes behave as second-order dynamic systems. Bubbling fluidized beds show one broad peak with a maximum at 2.6 Hz while slugging and turbulent beds show

two distinct peaks. It was observed that the peak at low frequency increases in magnitude as the flow transitions from slugging to turbulent fluidization regimes. CFD simulations of fluidized beds with the purpose of studying pressure fluctuations have demonstrated to be a useful tool to obtain hydrodynamic information that will help determine the fluidization regime. Prediction of slugging and turbulent regimes using CFD have only been studied in spouted fluidized beds by van Wachem et al. [60]. Therefore, the predictions reported in this study represent an important advantage when designing a reactor and evaluating different operation conditions without the need to test them in a pilot plant or a prototype.

CHAPTER 7. Conclusions and Future Work

Biomass is considered a biorenewable alternative energy resource that can potentially reduce the use of natural gas and provide low cost power production or process heating needs. Biomass hydrodynamics in a fluidized bed are extremely important to industries that are using biomass material in gasification processes to yield high quality producer gas. However, biomass particles are typically difficult to fluidize due to their peculiar shape and a second inert material, such as sand, is typically added to the bed. The large differences in size and density between the biomass and inert particles lead to nonuniform distribution of the biomass within the fluidized bed, and particle interactions and mixing become major issues. Problems such as particle agglomeration, defluidization, elutriation, and segregation can arise. The main goal of this research was to use CFD as a tool for modeling and analyzing the hydrodynamic behavior of biomass as a single material or as part of a mixture in fluidized bed. In this work, the open source software Multiphase Flow with Interphase eXchanges (MFIX) was used to simulate fluidized beds.

The first part of this research focused on the characterization of biomass particles in a fluidized bed and validation of a numerical model with experimental results obtained from pressure measurements and CT and X-ray radiograph images. For a 2D fluidized bed of glass beads, the pressure drop, void fraction and mean bed height expansion were in quantitative agreement between the experiments and simulations using Syamlal-O'Brien and Gidaspow drag models. It was encouraging that the Gidaspow model predictions were in close agreement because the model does not require knowing the minimum fluidization as an input, which is an issue when biomass is the bed material because in practice, the minimum fluidization velocity is not typically known.

Ground walnut shells were used to represent biomass because the material fluidizes uniformly and is classified as a Geldart type B particle. Two-dimensional simulations of ground walnut shells were analyzed to determine parameters that can not easily be measured experimentally. Both coefficient of restitution and sphericity were varied to determine the effects on the predictions. The coefficient of restitution study showed no significant differences in the hydrodynamics of the fluidized bed for values between 0.75 and 0.95. However, the particle sphericity study showed that sphericity does affect the behavior of the fluidized bed. It was shown that with decreasing sphericity, the bed more readily fluidized because the effective mean particle diameter decreased. Thus, higher sphericity values either underpredicted the bed expansion or the bed did not fluidize, whereas lower sphericities overpredicted the bed expansion. Although this study is specific to the bed medium, it does demonstrate that biomass can be modeled using the Gidaspow correlations. Furthermore, the parametric study for ground walnut shell indicated that the material can be characterized with a medium sphericity (≈ 0.6) and a relatively large coefficient of restitution (≈ 0.85).

In the second part of this work numerical simulations of a ground walnut shell fluidizing bed with side air injection were compared to CT data for the gas-solid distribution to demonstrate the quantitative agreement for bed fluidization. Two inlet gas velocities are examined; $1.5U_{mf}$ representing a mild bubbling bed and $3U_{mf}$ representing a moderate industrial reactor flowrate. Air injection, expressed in terms of the percentage of minimum fluidization volumetric flowrate, Q_{mf}, was simulated from no injection air to 20%, and one more case of two ports diametrically opposite to each other with $5\%Q_{mf}$ air was also studied. Two- and three-dimensional simulations were performed to determine if both modeling approaches would capture the salient bed features. The predictions for pressure drop through the biomass bed were initially validated with the experiments and were found to be in good agreement. The findings showed that 2D simulations overpredicted the fluidized bed expansion and the results did not demonstrate a uniformly fluidizing bed. The 3D simulations compared well for all cases. This study demonstrates the importance of using a 3D model for a truly 3D flow in order to capture the hydrodynamics of the fluidized bed for a complicated flow and geometry.

The effects of increasing side port air flow on the homogeneity of the bed were investigated next. It was found that increasing the side port injection flowrate up to $20\%Q_{mf}$ for a single port did not significantly affect the behavior of the bed, and the simulations compared well with the experimental measurements of void fraction. However, the simulations showed that adding a second side port injector on the opposite side of the reactor improved the mixing and overall homogeneity of the fluidized material.

It would be of interest to study the effects of adding one additional port, thus having three equally space ports along the circumference of the reactor to further study their effect on the homogeneity of the bed. CFD models can also be used to study the effects of placing injection ports at different bed heights and find an optimal location. Work has been conducted by Papadikis et al. [27,28] with the purpose of studying some aspects of hydrodynamics of biomass particles injected in a sand fluidized bed using a Lagrangian–Eulerian approach. Numerical modeling using an Eulerian-Eulerian approach is proposed for future work with the purpose of predicting the behavior of biomass particles injected in a fluidized bed of inert material. This model could be further implemented with chemical reactions and it would make a valuable design tool.

Finally, CFD modeling of pressure fluctuations was performed on sand and cotton-sand fluidized beds operating at inlet velocities ranging from 1.0–$9.0U_{mf}$ with the objective of predicting characteristic features of bubbling, slugging, and turbulent fluidization regimes. Pressure drop and mimimum fluidization velocity for sand and cotton-sand beds were tested using a 2D domain and Superbee discretization. The predicted values were in very close agreement with those reported in the experiments by Zhang et al. [13, 14]. Pressure drop trends between intermediate positions and time-average volume fraction contour plots show some segregation of cotton and sand at incipient fluidization velocities ($2U_{mf}$).

Standard deviation was overpredicted for inlet velocities greater than $4U_{mf}$ when using a 2D domain, therefore modeling with a 3D domain, as well of the use of a turbulence model for high velocities was studied. It was determined that the fluidized bed can be modeled using MUSCL discretization and the Ahmadi turbulence model used for velocities equal to

and greater than $6U_{mf}$, which corresponds to the peak of the standard deviation of pressure drop. Standard deviation of pressure drop for sand and cotton-sand fluidized beds yield very similar results and using 2D domain for velocities up to $4U_{mf}$ predict standard deviation close to experimental results.

Three-dimensional sand fluidized beds of the cases chosen to represent different fluidization regimes completed 195 seconds of simulation. Fluidized beds for all the regimes behaved as second-order dynamic systems. Bubbling fluidized beds showed one broad peak with a maximum at 2.6 Hz while slugging and turbulent showed two distinct peaks. It was observed that the peak at low frequency increased in magnitude as the flow transitioned from a slugging to a turbulent fluidization regime. CFD simulations of fluidized beds with the purpose of studying pressure fluctuations have demonstrated to be a useful tool to obtain hydrodynamic information that will help determine the fluidization regime. Prediction of slugging and turbulent fluidization regimes using CFD have not been reported to date. The work presented here is the first of its kind and can be an important advantage when designing a reactor and evaluating different operation conditions without the need to test them in a pilot plant or a prototype.

It is intended to use this work as a base to explore how different operating conditions, bed geometry, and bed material will affect the characteristics of the power spectrum. However,3D simulations for binary mixtures using a turbulence model are limited by computational resources. It is recommended to investigate the use of an autoregressive model to generate data to produce PSD and Bode plots from 20 to 60 seconds of simulation time and determine the validity of this model by comparing it with experimental data.

Bibliography

[1] Kunii, D. and Levenspiel, O., 1991, *Fluidization Engineering*, Butterworth-Heinemann, Boston, USA.

[2] Geldart, D., 1973, "Types of gas fluidization," Powder Technology, **7**(5), pp. 285–292.

[3] Cui, H. and Grace, J. R., 2007, "Fluidization of biomass particles: A review of experimental multiphase flow aspects," Chemical Engineering Science, **62**(1–2), pp. 45–55.

[4] Ohman, M., Pommer, L., and Nordin, A., 2005, "Bed agglomeration characteristics and mechanisms during gasification and combustion of biomass fuels," Energy and Fuels, **19**(4), pp. 1742–1748.

[5] Scala, F., Chirone, R., and Salatino, P., 2006, "Combustion and attrition of biomass chars in a fluidized bed," Energy and Fuels, **20**(1), pp. 91–102.

[6] Chirone, R., Miccio, F., and Scala, F., 2006, "Mechanism and prediction of bed agglomeration during fluidized bed combustion of biomass fuel: Effect of the reactor scale," Chemical Engineering Journal, **123**(3), pp. 71–80.

[7] Huilin, L., Yunhua, Z., Ding, J., Gidaspow, D., and Wei, L., 2007, "Investigation of mixing/segregation of mixture particles in gas-solid fluidized beds," Chemical Engineering Science, **62**(1–2), pp. 301–317.

[8] Nijenhuis, J., Korbee, R., Lensselink, J., Kiel, J. H. A., and van Ommen, J. R., 2007, "A method for agglomeration detection and control in full-scale biomass fired fluidized beds," Chemical Engineering Science, **62**(1–2), pp. 644–654.

[9] Bartels, M., Lin, W., Nijenhuis, J., Kapteijn, F., and van Ommen, J. R., 2008, "Agglomeration in fluidized beds at high temperatures: Mechanisms, detection and prevention," Progress in Energy and Combustion Science, **34**(5), pp. 633–666.

[10] Werther, J., Saengera, M., Hartgea, E.-U., Ogadab, T., and Siagib, Z., 2000, "Combustion of agricultural residues," Progress in Energy and Combustion Science, **26**(1), pp. 1–27.

[11] Franka, N. P., Heindel, T. J., and Battaglia, F., 2008, "Visualizing cold-flow fluidized beds with X-rays," *Proceedings of the ASME International Mechanical Engineering Congress and Exposition, IMECE 2007*, vol. **8** PART A, American Society of Mechanical Engineers, ASME Press, New York, NY, pp. 99–105, paper IMECE2007-43073.

[12] Franka, N., Drake, J., and Heindel, T. J., 2008, "Minimum fluidization velocity and gas holdup in fluidized beds with side port air injection," *Proceedings of the 2008 ASME Fluids Engineering Division Summer Conference*, American Society of Mechanical Engineers, paper FEDSM2008-55100.

[13] Zhang, Y., Jin, B., and Zhong, W., 2008, "Fluidization, mixing and segregation of biomass-sand mixture in a fluidized bed," International Journal of Chemical Engineering Reactor, **6**(A88).

[14] Zhang, Y., Jin, B., Zhong, W., Ren, B., and Xiao, R., 2009, "Characterization of fluidization and segregation of biomass particles by combining image processing and pressure fluctuation analysis," International Journal of Chemical Engineering Reactor, **7**(A81).

[15] Brown, R. C. and Brue, E., 2001, "Resolving dynamical features of fluidized beds from pressure fluctuations," Powder Technology, **119**(2–3), pp. 68–80.

[16] Brue, E. and Brown, R. C., 2001, "Use of pressure fluctuations to validate hydrodynamic similitude in fluidized media: Bubbling beds," Powder Technology, **119**(2–3), pp. 117–127.

[17] van Ommen, J. R., Sasic, S., van der Schaaf, J., Gheorghiu, S., Johnsson, F., and Coppens, M. O., 2011, "Time-series analysis of pressure fluctuations in gas-solid fluidized beds – a review," International Journal of Multiphase Flow, **37**, pp. 403–428.

[18] Ergun, S., 1952, "Fluid flow through packed columns," Chem. Eng. Progress, **48**(2), pp. 89–94.

[19] Hoffman, A., Janssen, L. M., and Prins, J., 1993, "Particle segregation in fluidized binary mixtures," Chem. Eng. Sci., **48**(9), pp. 1583–1592.

[20] Wu, S. and Baeyens, J., 1998, "Segregation by size difference in gas fluidized bed," Powder Technology, **98**, pp. 139–150.

[21] Nienow, A. and Naimer, N., 1980, "Continuous mixing of two particulate species of different density in a gas fluidized bed," Transactions of the Institution of Chemical Engineers, **58**, pp. 181–186.

[22] Chien-Song, C., Chen-Chung, K., and May-Yann, C., 1989, "Minimum fluidization velocity of binary mixtures," The Canadian Journal of Chemical Engineering, **67**, pp. 344–347.

[23] Sauter, J., 1928, "Untersuchung der von spritzvergasern gelieferten zerstaubung (study of atomization with spray carburetors)," Forschungsarbeiten auf dem Gebiete des Ingenieurwesens, **312**, p. 30.

[24] Wadell, H., 1935, "Volume, shape and roundness of quartz particles," Journal of Geology, **43**(3), pp. 250–280.

[25] Zhang, K. and Brandani, S., 2005, "CFD simulation in a circulating fluidized-bed biomass gasifier - A modified particle bed model in bubbling fluidized beds," Journal of Fuel Chemistry and Technology, **33**(1), pp. 1–5.

[26] Ravelli, S., Perdichizzi, A., and Barigozzi, G., 2008, "Description, applications and numerical modelling of bubbling fluidized bed combustion in waste–to-energy plants," Progress in Energy and Combustion Science, **34**, pp. 224–253.

[27] Papadikis, K., Bridgwater, A., and Gub, S., 2008, "CFD modelling of the fast pyrolysis of biomass in fluidised bed reactors, part A: Eulerian computation of momentum transport in bubbling fluidised beds," Chemical Engineering Science, **63**, pp. 4218 – 4227.

[28] Papadikis, K., Gub, S., and Bridgwater, A., 2010, "A CFD approach on the effect of particle size on char entrainment in bubbling fluidised bed reactors," Biomass and Bioenergy, **34**, pp. 21–29.

[29] Taghipour, F., Ellis, N., and Wong, C., 2005, "Experimental and computational study of gas-solid fluidized bed hydrodynamics," Chemical Engineering Science, **60**(24), pp. 6857–6867.

[30] Du, W., Bao, X., Xu, J., and Wei, W., 2006, "Computational fluid dynamics (CFD) modeling of spouted bed: Assessment of drag coefficient correlations," Chemical Engineering Science, **61**(5), pp. 1401–1420.

[31] Mahinpey, N., Vejahati, F., and Ellis, N., 2007, "CFD simulation of gas-solid bubbling fluidized bed: An extensive assessment of drag models," Computational Methods in Multiphase Flow IV:WIT Transactions on Engineering Sciences, **56**, pp. 51–60.

[32] Merry, J., 1971, "Penetration of a horizontal gas jet into a fluidised bed," Transactions of the Institution of Chemical Engineers, **49**(4), pp. 189–195.

[33] Zenz, F. A., 1968, "Bubble formation and grid design," IChemE Symposium Series, **30**, pp. 136–139.

[34] Shakhova, N. A., 1968, "Discharge of turbulent jets into a fluidized bed," Journal of Engineering Physics and Thermophysics, **14**(1), pp. 32–36.

[35] Hong, R., Li, H., Li, H., and Wang, Y., 1997, "Studies on the inclined jet penetration length on a gas-solid fluidized bed," Powder Technology, **92**(3), pp. 205–212.

[36] Rajan, F. and Christoff, J. D., 1992, "Effects of horizontal jet penetration on the combustion of coal in a fluidized bed," Journal of Energy, **6**(2), pp. 65–70.

[37] Chyand, C. S., Chang, C. H., and Chang, J. H., 1997, "Gas discharge modes at a single horizontal nozzle in a two-dimensional fluidized bed," Powder Technology, **90**(1), pp. 71–77.

[38] Chen, L. and Weinstein, H., 1993, "Shape and extent of the void formed by a horizontal jet in a fluidized-bed," AIChE Journal, **39**(12), pp. 1901–1909.

[39] Xuereb, C., Laguerie, C., and Baron, T., 1991, "Behavior of horizontal or inclined continuous jets gas-injected into a fluidized bed. Part I: Morphology of the jets," Powder Technology, **67**(1), pp. 43–56.

[40] Tyler, J. and Mees, P., 1999, "Using CFD to model the interaction of a horizontal feed jet on fluidized bed hydrodynamics," *Second International Conference on CFD in the Minerals and Process Industries, CSIRO, Melbourne*, pp. 113–117.

[41] Li, T., Pougatch, K., Salcudean, M., and Grecov, D., 2008, "Numerical simulation of horizontal jet penetration in a three-dimensional fluidized bed," Powder Technology, **184**, pp. 89–99.

[42] Li, T., Pougatch, K., Salcudean, M., and Grecov, D., 2009, "Numerical simulation of single and multiple gas jets in bubbling fluidized beds," Chemical Engineering Science, **64**, pp. 4884–4898.

[43] Yates, J. G. and Simons, J. R., 1994, "Experimental methods in fluidization research," International Journal of Multiphase Flow, **20**, pp. 297–330.

[44] Wilkinson, D., 1995, "Determination of minimum fluidization velocity by pressure fluctuation measurement," The Canadian Journal of Chemical Engineering, **73**, p. 562565.

[45] Puncochar, M. and Drahos, J., 2005, "Origin of pressure fluctuations in fluidized beds." Chemical Engineering Science, **60**, pp. 1193–1197.

[46] Felipe, C. A. S. and Rocha, S. C. S., 2007, "Prediction of minimum fluidization velocity of gas-solid fluidized beds by pressure fluctuation measurements analysis of the standard deviation methodology," Powder Technology, **174**(3), pp. 104–113.

[47] Sobrino, C., Sanchez-Delgado, S., Garcia-Hernando, N., and de Vega, M., 2008, "Standard deviation of absolute and differential pressure fluctuations in fluidized beds of group B particles," Chemical Engineering Research and Design., **86**(11A), p. 12361242.

[48] van Ommen, J. R., de Korte, R. J., and van der Bleek, C. M., 2004, "Rapid detection of defluidization using the standard deviation of pressure fluctuations," Chemical Engineering and Processing, **48**(10), pp. 1329–1335.

[49] Bi, H. T. and Grace, J. R., 1995, "Effects of measurement method on velocities used to demarcate the transition to turbulent fluidization," Chemical Engineering Journal, **57**, pp. 261–271.

[50] Bi, H. T., Grace, J. R., and Lim, K. S., 1995, "Transition from bubbling to turbulent fluidization," Industrial and Engineering Chemistry Research, **34**, pp. 4003–4008.

[51] Bi, H. T., Grace, J. R., and Zhu, J. X., 1995, "Regime transitions affecting gas-solids suspensions and fluidized beds," Transactions of the Institution of Chemical Engineers, **73**, pp. 154–161.

[52] Bi, H. T., Ellis, N., Abba, I. A., and Grace, J. R., 2000, "A state-of-the-art review of gas-solid turbulent fluidization," Chemical Engineering Science, **55**, p. 47894825.

[53] Iwasaki, H. K. N. and Matsuno, H. Y. Y., 1991, "Frequency analysis of pressure fluctuation in fluidized bed plenum," Journal of Chemical Engineering of Japan, **24**(1), pp. 76–8.

[54] Nicastro, M. T. and Glicksman, L. R., 1984, "Experimental verification of scaling relationships for fluidized-bed," Chemical Engineering Science, **39**, pp. 1381–1391.

[55] Parise, M. R., Kurka, P. R. G., and Taranto, O. P., 2009, "The Gaussian spectral pressure distribution applied to a fluidized bed," Chemical Engineering and Processing, **48**(1), pp. 120–125.

[56] Johnsson, F., Zijerveld, R. C., Schouten, J., van den Bleek, C. M., and Leckner, B., 2000, "Characterization of fluidization regimes by time-series analysis of pressure fluctuations," International Journal of Multiphase Flow, **26**(4), pp. 663–715.

[57] Schaaf, J. V. D., Schouten, J. C., Johnsson, F., and Bleek, C. M. V. D., 2002, "Non-intrusive determination of bubble and slug length scales in fluidized beds by decomposition of the power spectral density of pressure time series," International Journal of Multiphase Flow, **28**(5), pp. 865–880.

[58] Guo, Q., Yue, G., and Werther, J., 2002, "Dynamics of pressure fluctuation in a bubbling fluidized bed at high temperature," Industrial and Engineering Chemistry Research, **41**(14), pp. 3482–3488.

[59] Shou, M. C. and Leu, L. P., 2005, "Energy of power spectral density function and wavelet analysis of absolute pressure fluctuation measurements in fluidized beds," Chemical Engineering Research and Design, **83**(5A), pp. 478–491.

[60] van Wachem, B., Schouten, J., Krishna, R., and van den Bleek, C., 1999, "Validation of the Eulerian simulated dynamic behaviour of gas-solid fluidised beds," Chemical Engineering Science, **54**(13–14), pp. 2141–2149.

[61] Benyahia, S., Arastoopour, H., Knowlton, T., and Massah, H., 2000, "Simulation of particles and gas flow behavior in the riser section of a circulating fluidized bed using the kinetic theory approach for the particulate phase," Powder Technology, **112**, pp. 24–33.

[62] Lee, L. D. V., Chandrasekaran, B. K., Hulme, I., and Kantzas, A., 2005, "A non-invasive hydrodynamic study of gas-solid fluidised bed of linear low density polyethylene," The Canadian Journal of Chemical Engineering, **83**, pp. 119–126.

[63] Chandrasekaran, B. K., Lee, L. D. V., Hulme, I., and Kantzas, A., 2005, "A simulation and experimental study of the hydrodynamics of a bubbling fluidized bed of linear low density polyethylene using bubble properties and pressure fluctuations," Macromolecular Materials and Engineering, **290**(6), pp. 592–609.

[64] Johansson, K., van Wachem, B. G. M., and Almstedt, A. E., 2006, "Experimental validation of cfd models for fluidized beds: Influence of particle stress models, gas phase compressibility and air inflow models," Chemical Engineering Science, **61**(5), pp. 1705–1717.

[65] Sasic, S., Johnsson, F., and Leckner, B., 2006, "Inlet boundary conditions for the simulation of fluid dynamics in gas-solid fluidized beds," Chemical Engineering Science, **61**(16), pp. 5183–5195.

[66] Utikar, R. P. and Ranade, V. V., 2007, "Single jet fluidized beds: Experiments and CFD simulations with glass and polypropylene particles," Chemical Engineering Science, **62**(1–2), pp. 167–183.

[67] Mansourpour, Z., Karimi, S., Zarghami, R., Mostoufi, N., and Sotudeh-Gharebagh, R., 2010, "Insights in hydrodynamics of bubbling fluidized beds at elevated pressure by DEMCFD approach," Particulate and Science Technology, **8**(5), pp. 407–414.

[68] Wang, Q., Zhang, K., and Gu, H., 2011, "CFD simulation of pressure fluctuation characteristics in the gas-solid fluidized bed: Comparisons with experiments," Petroleum Science, **8**(2), pp. 211–218.

[69] Acosta-Iborra, A., Sobrino, C., Hernandez-Jimenez, F., and de Vega, M., 2011, "Experimental and computational study on the bubble behavior in a 3-D fluidized bed," Chemical Engineering Science, **66**(15), pp. 3499–3512.

[70] Sun, J., Zhou, Y., Ren, C., Wang, J., and Yang, Y., 2011, "CFD simulation and experiments of dynamic parameters in gas-solid fluidized bed," Chemical Engineering Science, **66**, pp. 4972–4982.

[71] Syamlal, M., Rogers, W., and O'Brien, T., 1993, "MFIX Documentation: Theory Guide," Technical Note DOE/METC-95/1013 and NTIS/DE95000031, National Energy Technology Laboratory, Department of Energy.

[72] Agrawal, K., Loezos, P. N., Syamlal, M., and Sundaresan, S., 2001, "The role of meso-scale structures in rapid gas-solid flows," Journal of Fluid Mechanics, **445**, pp. 151–185.

[73] Lun, C. K., Savage, S. B., Jeffrey, D. J., and Chepurniy, N., 1984, "Kinetic theories for granular flow: Inelastic particles in Couette flow and slightly inelastic particles in a general flowfield," Journal of Fluid Mechanics, **140**, pp. 223–256.

[74] Xie, N., Battaglia, F., and Pannala, S., 2008, "Effects of using two- versus three-dimensional computational modeling of fluidized beds: Part I, hydrodynamics," Powder Technology, **182**(1), pp. 1–13.

[75] Ma, D. and Ahmadi, G., 1988, "A kinetic model for rapid granular flows of nearly elastic particles including interstitial fluid effects," Powder Technology, **56**(3), pp. 191–207.

[76] Jenike, A. W., 1987, "A theory of flow of particulate solids in converging and diverging channels based on a conical yield function," Powder Technology, **50**(3), pp. 229–236.

[77] Schaeffer, D. G., 1987, "Instability in the evolution equations describing incompressible granular flow," Journal of Differential Equations, **66**(1), pp. 19–50.

[78] Dalla Valle, J. M., 1948, *Micromeritics, The technology of fine particles*, Pitman Pub. Corp., New York.

[79] Syamlal, M. and O'Brien, T., 2003, "Fluid dynamic simulation of O_3 decomposition in a bubbling fluidized bed," AIChE Journal, **49**(11), pp. 2793–2801.

[80] Gidaspow, D., 1994, *Multiphase Flow and Fluidization: Continuum and Kinetic Theory Descriptions*, Academy Press, Boston, USA.

[81] Huilin, L. and Gidaspow, D., 2003, "Hydrodynamics of binary fluidization in a riser: CFD simulation using two granular temperatures," Chemical Engineering Science, **58**(16), pp. 3777–3792.

[82] Lathouwers, D. and Bellan, J., 2000, "Modeling and simulation of bubbling fluidized beds containing particle mixtures," *Proceedings of the Combustion Institute*, vol. 28, pp. 2291–2304.

[83] Johnson, P. C. and Jackson, R., 1987, "Frictional-collision constitutive relations for granular materials with application to plane shearing," Journal of Fluid Mechanics, **176**, pp. 67–93.

[84] Harlem, F. H. and Welch, J. E., 1965, "Numerical calculation of time-dependent viscous incompressible flow and flui with free surface," The Physics of Fluids, **8**(12), pp. 2182–2189.

[85] Patankar, S. V., 1980, *Numerical Heat Transfer and Fluid Flow*, Hemisphere, Inc., Washington, USA.

[86] Chorin, A., 1967, "A numerical method for solving incompressible viscous flow problems," Journal of Computational Physics, **2**, pp. 12–26.

[87] Syamlal, M., 1994, "MFIX Documentation: User's Manual," Technical Note DOE/METC-95/1013, National Energy Technology Laboratory, Department of Energy.

[88] Tannehill, J. C., Anderson, D. A., and Pletcher, R. H., 1997, *Computational Fluid Mechanics and Heat Transfer*, Taylor & Francis, Inc., second edition.

[89] Leonard, B. P., 1991, "The ULTIMATE conservative difference scheme applied to unsteady one-dimensional advection," Computer Methods in Applied Mechanics and Engineering, **88**(1), pp. 17–74.

[90] Syamlal, M., 1998, "MFIX Documentation: Numerical Technique," Technical Note DOE/MC31346-5824 and NTIS/DE98002029, National Energy Technology Laboratory, Department of Energy.

[91] Heindel, T. J., Hubers, J. L., Jensen, T. C., Gray, J. N., and Striegel, A. C., 2005, "Using X-rays for multiphase flow visualization," *Proceedings of ASME Fluids Engineering Division Summer Conference, 2005 Forum*, vol. **2**, New York, NY, pp. 415–423, paper FEDSM2005-77359.

[92] Heindel, T. J., Gray, J. N., and Jensen, T. C., 2008, "An X-ray system for visualizing fluid flows," Flow Measurement and Instrumentation, **9**(2), pp. 67–78.

[93] Abdullah, M. Z., Husain, Z., and Yin Pong, S. L., 2003, "Analysis of cold flow fluidization test results for various biomass fuels," Biomass and Bioenergy, **24**(6), pp. 487–494.

[94] Davidson, J. and Harrison, D., eds., 1971, *Fluidization*, chap. 2, Incipient Fluidization and Particulate Systems, American Press, London and New York, pp. 27–29, author: J. F. Richardson.

[95] Syamlal, M., 1998, "High Order Discretization Methods for the Numerical Simulation of Fluidized Beds," Technical Note DOE/FETC/C-98/7305 and CONF-971113, Department of Energy.

[96] Cao, J., Cheng, Z., Fang, Y., Jing, H., Huang, J., and Wang, Y., 2008, "Simulation and experimental studies on fluidization properties in a pressurized jetting fluidized bed," Powder Technology, **183**(1), pp. 127–132.

[97] Ahuja, G. N. and Patwardhan, A. W., 2008, "CFD and experimental studies of solids hold-up distribution and circulation patterns in gas-solid fluidized beds," Chemical Engineering Journal, **143**(1–3), pp. 147–160.

[98] Patel, A. K., Waje, S. S., Thorat, B. N., and Mujumdar, A. S., 2008, "Tomographic diagnosis of gas maldistribution in gas-solid fluidized beds," Powder Technology, **185**(3), pp. 239–250.

[99] Deza, M., Battaglia, F., and Heindel, T. J., 2007, "Computational modeling of biomass in a fluidized bed gasifier," *Proceedings of the 2007 ASME International Mechanical Engineering Congress and Exposition, IMECE 2007*, vol. **8** PART A, New York, NY, pp. 107–114, paper IMECE2007-43097.

[100] Deza, M., Battaglia, F., and Heindel, T. J., 2008, "A validation study for the hydrodynamics of biomass in a fluidized bed," *Proceedings of the 2008 ASME Fluids Engineering Division Summer Conference*, paper FEDSM2008-55158.

[101] Deza, M., Battaglia, F., and Heindel, T. J., 2008, "Approximating a three-dimensional fluidized bed with two-dimensional simulations," *Proceedings of the 2008 ASME International Mechanical Engineering Congress and Exposition*, paper IMECE2008-66378.

[102] Min, J., Drake, J. B., Heindel, T. J., and Fox, R. O., 2010, "Experimental validation of CFD simulations of a lab-scale fluidized-bed reactor with and without side-gas injection," AIChE Journal, **56**(6), pp. 1434–1446.

[103] Deza, M., Franka, N. P., Heindel, T. J., and Battaglia, F., 2009, "CFD modeling and X-ray imaging of biomass in a fluidized bed," Journal of Fluids Engineering-Transactions of the ASME, **131**(11), pp. 111303– 1–11.

[104] Reardon, J., 2007, "Better biomass gasification for the ethanol industry," Personal Communication: A Presentation by Frontline BioEnergy to T.J. Heindel.

[105] Franka, N. and Heindel, T., 2009, "Local time-averaged gas holdup in a fluidized bed with side air injection using X-ray computed tomography," Powder Technology, **193**(1), pp. 69–78.

[106] Komo, J. J., 1987, *Random Signal Analysis in Engineering Systems*, Academic Press, Orlando, USA.

[107] Jenkins, G. M. and Watts, D. G., 1968, *Spectral Analysis and Its Applications*, Holden-Day, San Francisco, USA.

[108] Brue, E. J., 1996, *Pressure Fluctuations as a Diagnostic Tool for Fluidized Beds*, PhD Thesis, Iowa State University, Ames, IA.

[109] Brown, R., Brue, E., Schroeder, J. R., and Cruz, R. D. L., 1998, "Pressure Fluctuations as a Diagnostic Tool for Fluidized Beds," Technical Report DE-FG22-94PC94210–15, Federal Energy Technology Center, Department of Energy.

[110] Roy, R., Davidson, J. F., and Tuponogov, V. G., 1990, "Velocity of sound in fluidised beds," Chemical Engineering Science, **45**(11), pp. 3233–3245.

[111] Hiby, J. W., 1967, "Periodic phenomena connected with gas-solid fluidization," *Proceedings of the International Symposium on Fluidization*, p. 99.

[112] Verloop, J. and Heertjes, P. M., 1974, "Periodic pressure fluctuations in fluidized beds," Chemical Engineering Science, **29**(4), pp. 1035–1042.

[113] Sun, J., Chen, M. M., and Chao, B. T., 1994, "Modeling of solids global fluctuations in bubbling fluidized beds by standing surface waves," International Journal of Multiphase Flow, **20**(2), pp. 315–338.

[114] Deza, M., Heindel, T. J., and Battaglia, F., 2011, "Effects of mixing using side port air injection on a biomass fluidized bed," Journal of Fluids Engineering-Transactions of the ASME, **133**(11), pp. 111302–1–9.

[115] Xie, N., Battaglia, F., and Pannala, S., 2008, "Effects of using two- versus three-dimensional computational modeling of fluidized beds: Part II, budget analysis," Powder Technology, **182**(1), pp. 14–24.

[116] van der Schaaf, J., van Ommen, J. R., Takens, F., Schouten, J. C., and van den Bleek, C., 2004, "Similarity between chaos analysis and frequency analysis of pressure fluctuations in fluidized beds," Chem. Eng. Sci., **59**, pp. 1829–1840.